Novel Approaches for Improving Efficiency and Stability of Next Generation Perovskite Solar Cells

by

Aditya Sumanth Yerramilli

A Dissertation Presented in Partial Fulfillment
of the Requirements for the Degree
Doctor of Philosophy

Approved September 2020 by the
Graduate Supervisory Committee:

Terry Alford, Chair
David Theodore
Yuanqing Chen

ARIZONA STATE UNIVERSITY

December 2020

ABSTRACT

Perovskite solar cells are the next generation organic-inorganic hybrid technology and have achieved remarkable efficiencies comparable to Si-based conventional solar cells. Since their inception in 2009 with an efficiency of 3.9%, they have improved tremendously over the past decade and recently demonstrated 25.2% efficiency for single-junction devices. There are a few hurdles, however, that prevent this technology from realizing their full potential, such as stability and toxicity of the perovskites. Apart from solution processing in the fabrication of perovskites, precursor composition plays a major role in determining the quality of the thin film and its general properties. This work studies novel approaches for improving the efficiency and stability of the perovskite solar cells with minimized toxicity. The effect of excess Pb on photo-degradation in $MAPbI_3$ perovskites in an inverted device architecture was studied with a focus on improving stability and efficiency. Precursor concentration with 5% excess Pb was found to be optimal for better efficiency and stability against photo-degradation. Further improvements in efficiency were made possible through the addition of Zirconium Acetylacetonate as a secondary electron buffer layer. A concentration of 1.5mg/ml was found to be optimal for demonstrating better efficiency and stability. Partial substitution of Pb with non-toxic Sr was also studied for improving the stability of inverted devices. Using acetate-derived precursors, 10% Sr was introduced into perovskites for improvements to the stability of the device.

In another study, triple-cation perovskites with FAMACs cations were studied with doping different amounts of Phenyl Ethyl Ammonium (PEA) to induce a quasi 2D-3D structure for improved moisture stability. Doping the perovskite with 1.67% PEA was

found to be best for improved morphology with fewer pinholes, which further resulted in better V_{OC} and stability. A passivation effect for triple-cation perovskites was further proposed with the addition of a Guanidinium Iodide layer on the perovskite. Concentrations of 1mg/ml and 2mg/ml were demonstrated to be best for reducing defects and trap states and increasing the overall stability of the device.

DEDICATION

To my parents, Shri Venkat Rao Yerramilli, Smt. Vijayasri Yerramilli

and sister, Samyuktha for their love and support

ACKNOWLEDGMENTS

I take this opportunity to acknowledge the support and assistance of many individuals without whom this dissertation would not have been possible.

I had the privilege of having Dr. Terry Alford as my advisor, and I thank him for his invaluable guidance and support throughout my doctoral studies. I would like to thank my committee member and advisor, Dr. Yuanqing Chen, for his valuable inputs and guidance in my research. I would also like to express my gratitude to my committee member, Dr. David Theodore, for taking the time and effort to evaluate my thesis work and provide constructive feedback.

I thank Dr. Emmanuel Soignard, Mr. David Wright, Mr. Tim Karcher, and Ms. Diana Convey, Dr. Y.K. Lee for training me on the various materials characterization and deposition tools that I regularly used in my research. I would like to acknowledge their periodical assistance in my projects, without which the dissertation would not have been possible.

I would like to thank Dr. Aritra Dhar, Dr. Sayantan Das, and Dr. Zhao Zhao for their guidance on my initial research projects. I also thank Dr. Aprillya Lanz for her encouragement during my Ph.D. I would also like to acknowledge the friendship and assistance of Banashree Gogoi and for support from my family, Dr. Pavan Turaga and Dr. Ramya Turaga, during my Ph.D. I also thank Subbarao, Diana, Taylor, Smitha, Suneet, and all my friends for their support throughout my academic studies at ASU.

TABLE OF CONTENTS

CHAPTER Page

LIST OF TABLES

LIST OF FIGURES

CHAPTER 1

INTRODUCTION

1.1 Background

Today's primary energy sources, Oil and Coal, are tending towards an eventual decline, which would force us to replace them with renewable energy sources [1]. Global production of oil is forecasted to drop in the next few decades, according to several estimates [2]. This drop in the production would eventually result in a rise in oil prices, which would necessitate the utilization of various renewable energy sources such as Solar, Hydroelectric, Tidal, and Wind energy systems [3]. Fossil Fuels are also known to cause other issues such as a rise in greenhouse gases, which can have significant environmental impacts and do not promote sustainable living [4]. The CO_2 emissions resulting from excessively burning these fossil fuels, and increased human activity, increase the global temperature by a 0.6 – 0.7 ^{0}C every year [5–7].

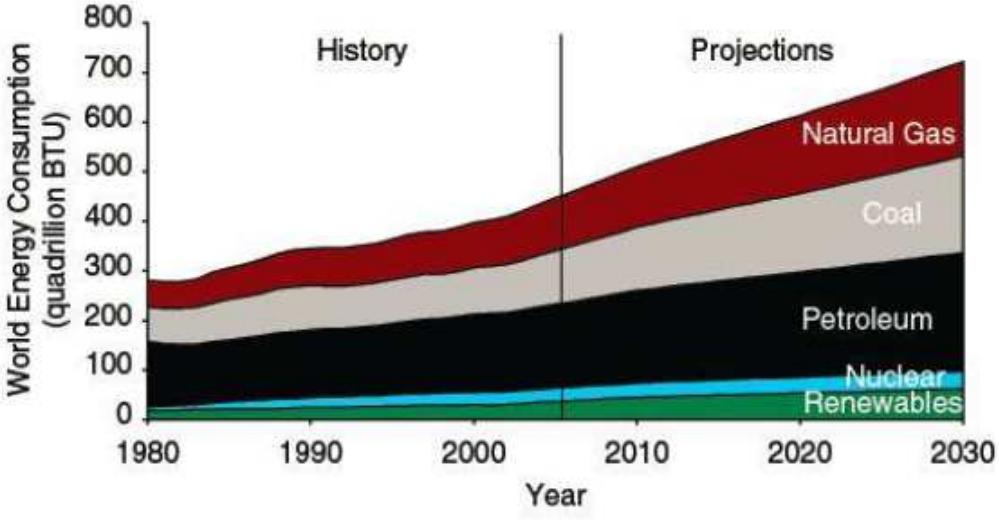

Fig. 1.1 Estimation of World's energy consumption by 2030 [4]

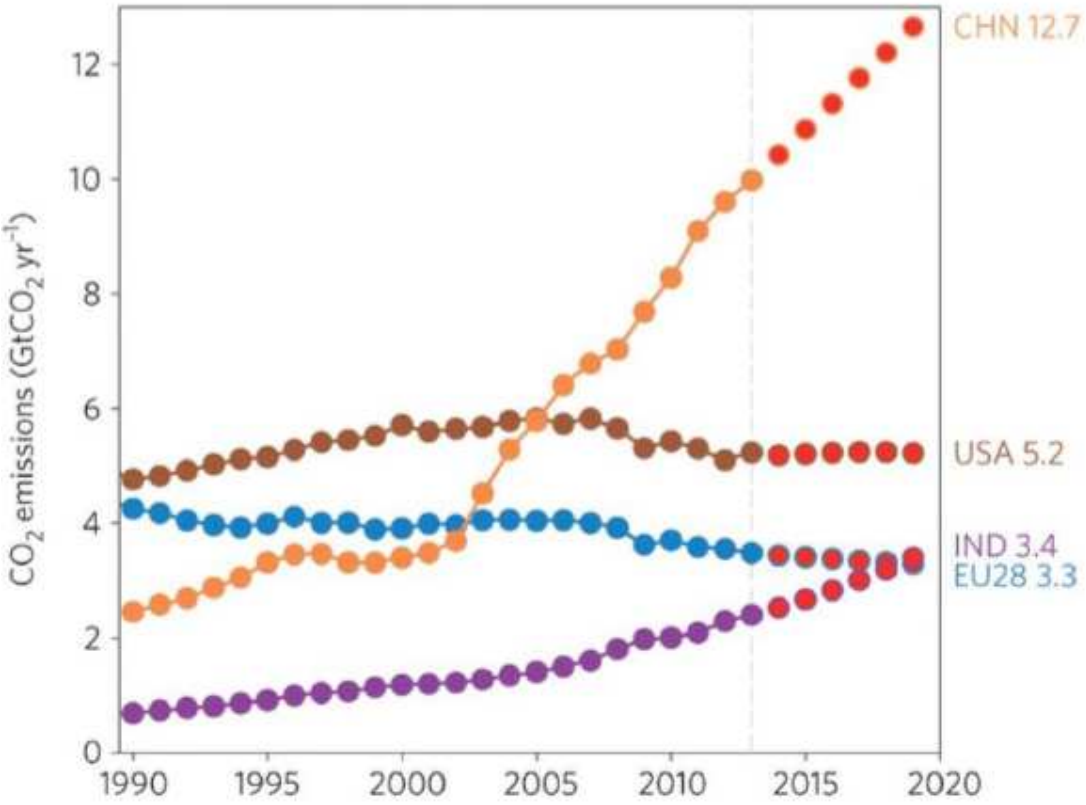

Fig. 1.2 Carbon dioxide emissions from the top four emitters of the world (China, USA, EU28, and India) [8]

Renewable energy sources are regarded as the best possible solution to these issues. From bringing down CO_2 emissions to promoting sustainable living conditions, these sources are not only capable of generating the energy necessary to power the whole world but also are eco-friendly. Only three renewable energy sources: biomass, geothermal, and solar can be used for power generation, given the amount of heat that energy that can be extracted. Given that geothermal sources are contained by fewer locations, and biomass is not present everywhere, solar energy has the highest potential to become the primary energy source. The amount of solar energy irradiant on the earth is approximately 342 Wm^{-2}, 30% of which is either reflected back or scattered elsewhere [9]. The remaining 70%

(239 Wm^{-2}) is available for harvest [9]. Across the earth, annual effective solar irradiance varies from 60 to 250 Wm^{-2} [10]. Fig. 1.3 shows the annual average intensity of solar radiation over the surface of the earth. The "black dot" areas are estimated to provide more than the world's total primary energy demand, given a conversion efficiency of 8%[11]. Amongst all the places across the globe, Africa is theoretically estimated to receive 470-660 petawatt hours (PWh)[12]. Other areas, such as the south-western US, central and south America, Middle East, India, Pakistan, etc., are estimated to generate 125-gigawatt hours (GWh)[13]. This information shows the scope to exploit Solar energy as a resource for the primary energy needs of the world.

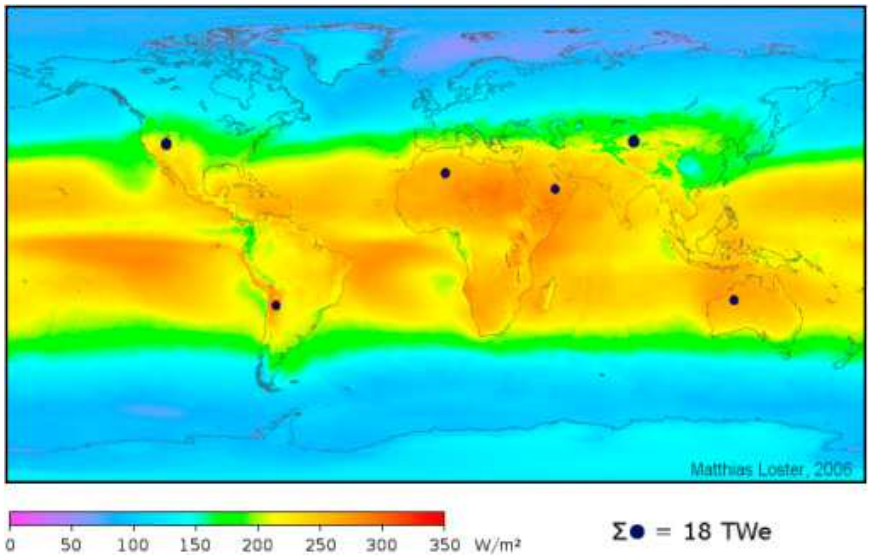

Fig. 1.3 Annual average solar irradiance distribution over the surface of the earth [11]

Solar energy can be classified into two types: active and passive energy technologies. Passive energy technology can be further classified into Direct, Indirect, and Isolated solar gain, and these techniques are outside the scope of this report. Active solar energy can be grouped into two categories – Photovoltaic and Solar Thermal technology.

Solar thermal technology involves practices where solar energy is converted into thermal energy for various commercial and domestic applications and is these topics are also outside the scope of this work. Photovoltaic technology involves the use of semiconductors to convert sunlight into electrical energy, and this area has seen several efforts from Researchers and Scientists across in development.

1.2 Current Solar Technologies

Several innovations have spurred the growth of the now commercially available inorganic solar cells. These comprise mono-crystalline Silicon (Si), III-V compounds and alloys,..3 Cadmium Telluride (CdTe), copper indium gallium diselenide (CIGS) [14]. Mono-crystalline Si solar cells are reported to have the highest of 25.6% efficiency to date[15]. The current market is dominated by Si-based solar cells with a 90% market share, and the technology has already matured with current efforts being focused only on cost reduction of modules. Since the crystalline Si requires defect-free processing and high thickness to be efficient, it requires costly equipment and conditions for large scale manufacturing [16,17]. Alternative inorganic materials such as CdTe and $CuInGaSe_2$ have fewer requirements to demonstrate 21% efficiency [15,18], but the costs involved in the processing are still high. Multi-junction solar cells making up of multiple absorbers demonstrated 46% efficiency [15] and are mostly used for non-commercial based applications given their high production cost. However, a major challenge for the PV community with these solar cells is the high production cost. The high costs pushed researchers to pursue the so-called ‘third-generation’ solar cells to overcome the limitations of the previous ones with the appeal of simpler processing routes and cheaper fabrication procedures required. Organic solar cells (OSCs) that are made up of polymers and organic

molecules have received a lot of interest given their simpler processing and operation at lower temperatures (25-200 ^{0}C). [19–22]. The simple solution processing methods adopted in the synthesis of these devices allow the tailoring of the composition and hence the performance [23,24]. Hybrid organic-inorganic solar cells such as Perovskite Solar Cells (PSCs) have emerged as a prime candidate for photovoltaic applications and fall under the class of emerging photovoltaics. Single-junction PSCs have surpassed all emerging photovoltaics in terms of efficiency delivered, which is very profound, given that they were explored as solar cell absorber materials only in 2009 (see Fig. 1.4). However, there is still a lot of room for improving the efficiency and stability through precursor concentration control and addition of buffer layers to facilitate better charge transport and extraction.

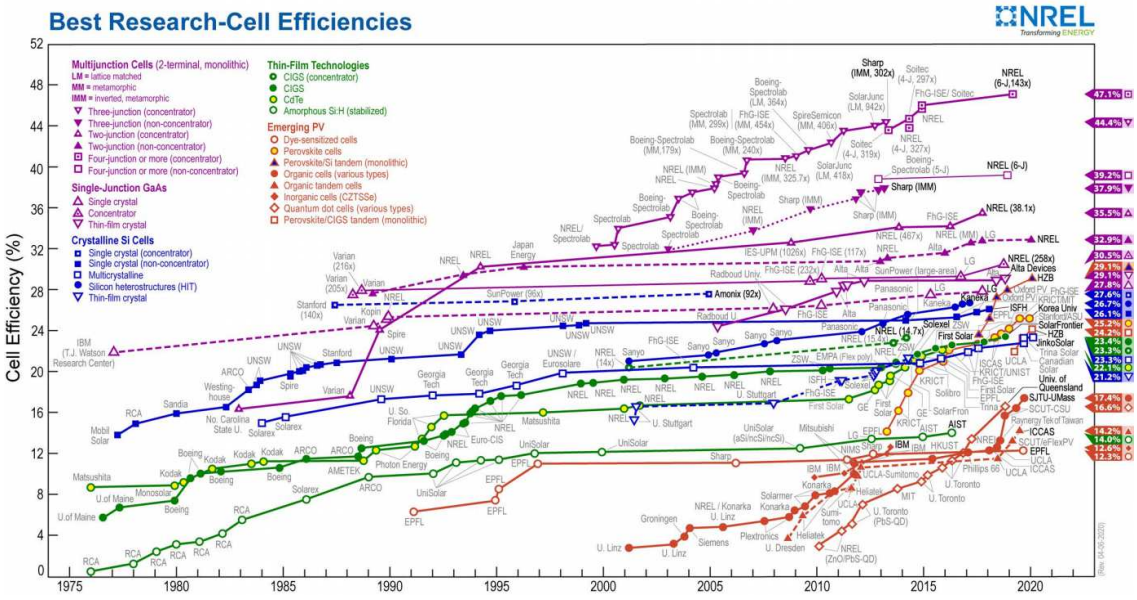

Fig. 1.4 Best solar cell efficiencies (National Renewable Energy Laboratory (NREL)) [18]

1.3 Outline of the Thesis

The focus of this dissertation is to realize methods to improve the efficiency and stability of PSCs. In that regard, approaches related to composition tuning of the perovskite and additional layers for passivation and charge transport were developed, for optimizing the efficiency and stability of the device, with a focus also on minimizing the toxicity of the perovskite. Chapter 2 presents an overview of perovskites and discusses the common materials and architectures of PSCs and processing methodologies used in the research community. Chapter 3 discusses the impact of excess Pb on the photo-degradation of PSCs. Chapter 4 discusses the influence of adding Zirconium Acetylacetonate as a secondary buffer layer for improved efficiency through better charge extraction. Chapter 5 discusses the partial substitution of Pb with non-toxic Sr up to 30%, with improved stability. Chapter 6 presents a discussion on the effect of introducing Phenyl Ethyl Ammonium into Triple-cation perovskite for improved V_{OC} and stability. Chapter 7 discusses the addition of Guanidinium Iodide as a passivation layer on Triple-cation perovskite for improved efficiency and stability.

CHAPTER 2

PEROVSKITE SOLAR CELLS: AN OVERVIEW

Organic-inorganic halide PSCs have received a lot of attention from the solar research community, which could be attributed to the dramatic rise in efficiency from 3.8% to over 25% [18]. With PSCs suggested as potential alternatives to silicon photovoltaics and with researchers working on dye-sensitized solar cells (DSSCs) being able to relate to PSCs due to some similarities in materials and principles, a lot of progress was made possible with an eye for commercialization. The use of cheaper methods to fabricated PSCs made them more attractive with large-scale roll-to-roll manufacturing demonstrated in several reports [25–27].

The origin of perovskites can be traced to the initial discovery of calcium titanate as a mineral and was subsequently named after Lev Perovski. All compounds occurring in the same crystal structure were referred to as Perovskites. A more detailed discussion on the structure and properties of perovskites is presented in the following sections.

2.1 Materials and Principles of Working

2.1.1 Crystal structure and phases

The perovskite structure can be defined as ABX_3, where A and B refer to two cations of different sizes, and X is the anion that bonds to both. Among several compounds and elements that can be part of the structure, $CH_3NH_3PbX_3$ is most commonly reported for solar cell applications. Methylammonium (MA) here is the A cation surrounded by PbX_6 octahedra, as shown in Fig. 2.1. X is the usually a halide element such as iodide or chloride or bromide, or a combination of these. The structure formation is estimated using Goldschmidt's tolerance factor 't,' as per the equation:

$$t = (rA+rX) / 2^{1/2} [rM + rX] \qquad (2.1)$$

where rA, rM, and rX are effective ionic radii for A, M, and X ions, respectively [28]. Tailoring of the composition is possible with different combinations of anions and cations as long as they satisfy the criterion.

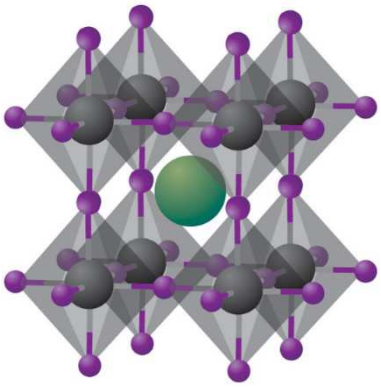

Fig. 2.1 Crystal structure of perovskite: MA^+ represented by green; Pb^{2+} represented by grey and I^- represented by purple [29]

The perovskite structure is determined by the size of the organic cation. In the above case, MA was used to describe a common 3D structure. However, if a larger organic cation is introduced, a structure with alternating layers of organic and inorganic compounds, held together by van der Waals forces, is formed. The 3D perovskite structure is known to form four sold phases, of which three are perovskite-based (α, β, γ) and one non-perovskite (δ) phase. At high temperatures (>327K), the α phase is observed in a cubic structure, and lower than 327K and phase transition is observed from α to β. MA cation is known to be disordered in both these phases. An orthorhombic structure is realized at lower temperatures than 162K, where the γ phase is observed with highly ordered MA cations. Rotation of MA cations is known to be rapid at higher temperatures and little or no rotation at low temperatures. The fourth δ phase is understood as being formed in solvent environments and is currently under investigation [30].

There are several advantageous properties for a perovskite absorber such as (i) strong optical absorption; (ii) high electron and hole mobilities and long diffusion lengths (orders of μm); (iii) superior defect tolerance; (iv) low surface recombination rates; (v) grain boundaries that limit recombination [31–33]. With a tunable bandgap of 1.55 eV, a wide range of wavelengths can be captured for generating charges from the perovskite absorber [34]. This property helps incorporate other elements into the perovskite resulting in a change in the bandgap and corresponding absorption properties. Fig. 2.2 shows the energy level diagram for different combinations of perovskite materials.

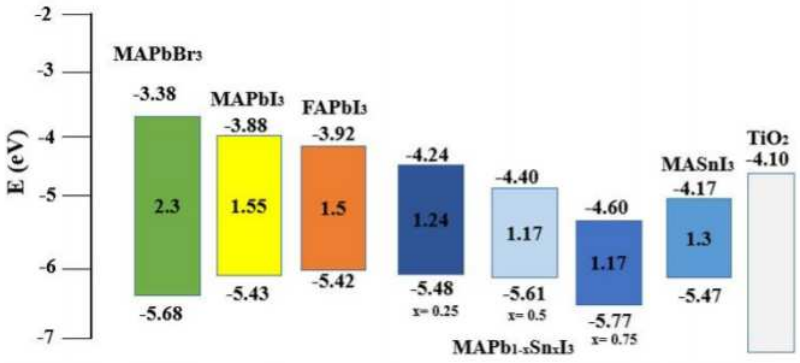

Fig. 2.2. Schematic illustration of the energy level diagram with different perovskite compound combinations [34]

2.1.2 Operating principles of PSCs

Organic materials are known for high absorption coefficients for thin layers (100nm – 200nm), which make them suitable candidates for these devices [35,36]. In PSCs, however, exciton generation is not reported, but rather charges are created and separated efficiently based on energy level differences between the various layers in the device [35]. The diffusion of generated charge carriers is very important in understanding the working

of PSCs. The average diffusion length of charges is estimated using the diffusion coefficient (D) and recombination lifetime τ, according to the equation:

$$L_D = \sqrt{D\tau} \qquad (2.2)$$

Balanced charge transport is an advantageous property of PSCs, as demonstrated by Xing [37]. Photoluminescence spectroscopy and transient absorption measurements were used to estimate the diffusion lengths as $L_D^e \sim 1069$nm and $L_D^h \sim 1213$nm for electron and hole, respectively. For higher efficiency without recombination, the diffusion lengths need to be larger than the typical thickness of the absorption layer [38].

Regarding the functioning of the device, the perovskite absorbs photons and creates electron-hole pairs. The electrons and holes are separated at the interface of the perovskite and the charge transport layers and travel to the back contacts into the external circuit. The process occurs in a few picoseconds and can be detailed in three different steps:

(a) Charge generation

Perovskites are known to have low exciton binding energies (~2 meV), which implies the process of generation charges is not through excitons [39], which is unlike conventional organic solar cells. The efficient generation of carriers is highly possible in perovskite, given that it is non-excitonic in nature. When the light of a bandgap higher than the Fermi energy is incident on the perovskite, the energy absorbed results in the dissociation of electrons and holes, which move into the empty molecular orbitals.

(b) Charge transport and recombination

As mentioned previously, the electron and hole effective masses are very close, and the spin-orbit coupling is very strong, due to the presence of heavy elements such as Pb

[40,41]. While transport of generated charge carriers is accomplished by having charge selective layers, recombination is to be avoided at all costs. Efficient charge extraction requires well-defined interfaces and the appropriate thickness of the corresponding layers to support the diffusion. In a realistic situation, several causes can prevent this, and some of the important ones are (i) annihilation of charges through photoluminescence, (ii) non-radiative recombination, and (iii) recombination at the interface, usually resulting in heat release.

(c) Charge extraction

The choice of the charge transport materials is based on the Fermi level alignment with respect to the perovskite, as shown in Fig. 2.3 to facilitate the efficient extraction process. Further on, the common materials used and configurations will be discussed in the later section of this chapter. The built-in electric field in the perovskite and the interface is responsible for the charge movement, and band-bending is observed after equilibrium is reached.

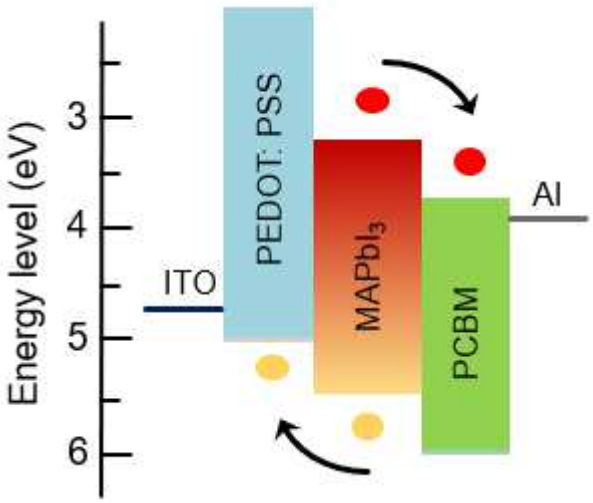

Fig. 2.3. Band level alignment of PSCs

2.2 Common Device Architectures

Several configurations, such as mesoporous-conducting scaffold; mesoporous-insulating oxide; planar; HTM-free, and inverted, are commonly used in the research on PSCs [33]. The highest efficiencies reported were of planar (21% PCE) [42] and planar (20.7% PCE) [43]. Planar and inverted configurations and corresponding materials will be discussed further.

2.2.1 Planar PSC

A planar configuration, as shown in Fig. 2.4, consists of a hole blocking layer on top of a transparent conductive oxide such as Indium doped Tin Oxide (ITO). The perovskite is deposited on top of the blocking layer, and a hole transport material (HTM) is deposited on top of the perovskite, and a back contact such as Ag or Au is thermally evaporated on top of the HTM. TiO_2, generally known for its mesoporous properties, can be employed as hole blocking material by making it compact and reducing thickness [44]. Other materials such as ZnO were later explored for utilizing their high electron mobility properties [27]. Further improvements in efficiency were achieved by using SnO2 [43]. SpiroOMeTAD is usually the choice of hole transport material given its superior charge transport properties and favorable fermi levels [27,33,43]. Hysteresis is an effect where the forward and reverse scans generate different I-V curves. The origin of this is pointed to the capacitive effect of the perovskite arising due to ion movement [45]. Guo et al. used P3HT based HTM to minimize the hysteresis and reported 12.4% PCE [46].

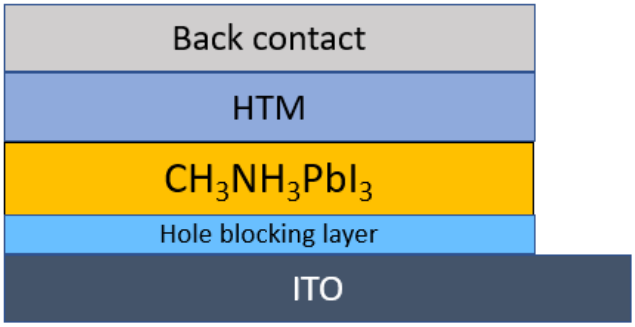

Fig. 2.4. The planar architecture of PSCs

2.2.2 Inverted PSC

As the name suggests, in an inverted configuration, the hole transport layer (HTL) is first deposited on top of the ITO/glass. This is followed by the perovskite and then the electron transport layer (ETL). The structure is as shown in Fig. 2.5. Poly (3,4-ethylene dioxythiophene) polystyrene sulfonate (PEDOT: PSS) is commonly reported as the HTL, with one of the first devices reported by Jeng et al. [47]. C_{60} derivatives such as [6,6]-phenyl C_{61}-butyric acid methyl ester (PCBM) were soon developed with efficiency increasing to 16% [48]. PEDOT: PSS is known to be hygroscopic in nature, which compromises the long-stability of the device, and hence Nickel Oxide was used to replace it as the HTM [49]. Further development in overcoming the instability of the polymer-based layers led to the use of NiO and crystalline SnO_2 as the HTL and ETL in an inverted configuration with an efficiency of 18.8% with the stability of almost 90% PCE being maintained over 30 days [50].

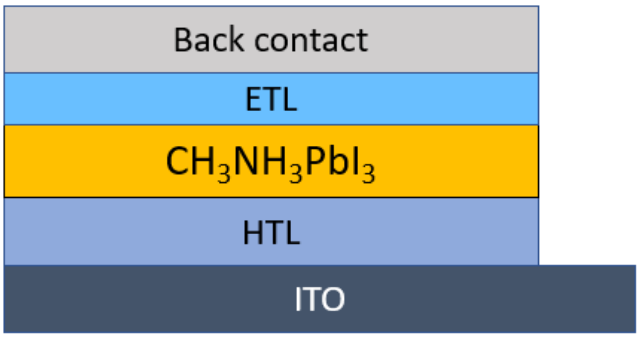

Fig. 2.5. The inverted architecture of PSCs

2.3 Research Thrusts and Challenges

Perovskite solar cells (PSCs) are a relatively new class of photovoltaic technology, which has seen a remarkable high in power conversion efficiency (PCE), mainly possible due to the ease of optimization of the individual layers. The versatility of processing techniques and low costs also made this technology to be developed faster. A lot of research activity was dedicated to improving the efficiency and stability of the device for potential alternatives to existing Si-based solar cells. While a high efficiency of 23.3% has been achieved for a small area device of 0.09 cm^2[18,51], and the precursors are earth abundant-materials [52] (Fig. 2.6), poor stability of the device hamper PSCs to realize their full potential [53]. The perovskite thin-film growth mechanism is governed by several factors, such as the solvent and the antisolvent properties, annealing processes, and precursor concentration. A variety of solvents such as Dimethyl Formamide (DMF), dimethyl sulfoxide (DMSO), N, N dimethylacetamide (DMA), γ-butyrolactone (GBL) are commonly employed in the dissolving of perovskite precursors [54]. Since DMF and DMSO are widely used in dissolving the perovskite precursors, the discussion in this work is limited only to these solvents.

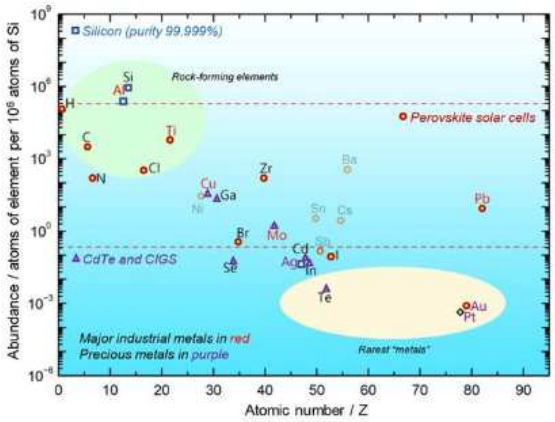

Fig. 2.6. Atom fraction of elements used in different types of solar cells, Si solar cells (blue squares); PSCs (Red circles); CdTe, and CIGS (purple triangles). Major industrial metals and precious metals are classified according to Goldschmidt rules [52,55]

2.3.1 Toxicity In Perovskites

The toxicity of the solvents and materials used in the perovskites are cause for concern. Solvent-free deposition and solution-based approaches that use chemicals with minimal toxicity [56,57] still need further research. Besides the solvents, the lead (Pb) in the perovskite is one of the primary sources of toxicity. The development of lead-free solar cells would always be desirable for commercial applications. Ideally, some of the critical properties such as narrow bandgaps, high optical absorption coefficients, high mobilities, low exciton-binding energies, long charge-carrier lifetimes, and good stabilities are key towards the development of lead-free perovskites [58]. Few materials can meet the above criteria while offering the structural integrity to the perovskite – Sn/Ge based halides, Bi/Sb based halides, as shown in Fig. 2.7. [59,60].

Of the various materials, one of the best performances for a lead-free perovskite was first demonstrated by the Kanatzidis group [61], and this was followed by several improvements with a more recent report demonstrating 9.6% [62]. Both of the works were based on Sn-based perovskites, and these materials, although had low V_{OC}'s (~0.5V), gave high current densities due to the lower bandgap (1.10 – 1.20 eV) [60]. The main disadvantage with Sn-based perovskites is the unwanted oxidation of Sn^{2+} to Sn^{4+}which leads to more p-type properties resulting in too high dark carrier concentration and large carrier recombination [58].

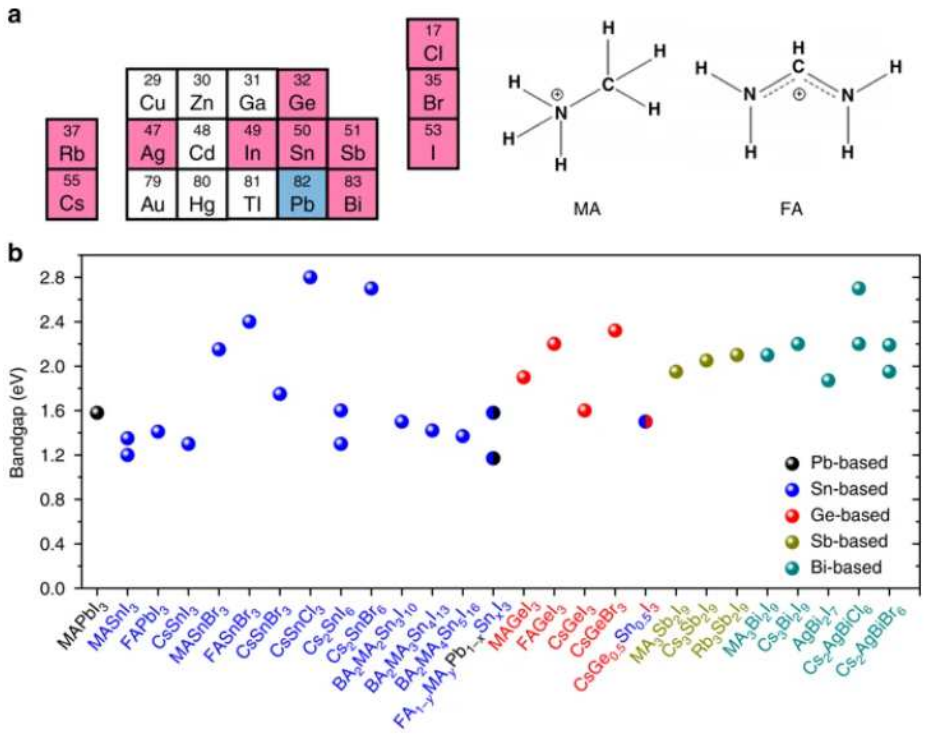

Fig. 2.7. a) Potential A-site cations (organic MA and FA or inorganic Cs and Rb), metals, and halides (I, Br, Cl) for perovskite structure b) Bandgaps of various materials

Ge based perovskites are relatively less explored, given that they possess much wider bandgaps such as 1.9eV and 2.2eV for $MAGeI_3$ and $FAGeI_3$, respectively [58].

Alloys of Sn and Ge with Cs as the A-site cation possess a narrower bandgap of 1.5eV and demonstrated a PCE of 7.11% [63]. Other elements outside Sn and Ge are underexplored as a means of replacing Pb. Sr is one of the elements where its inclusion in small percentages proved to improve the optoelectronic properties by means of passivation in the inorganic $CsPbI_2Br$ perovskites[64]. A remarkable 10.8% PCE was obtained with Sr^{2+} acting a passivating agent on the surface of the perovskite. Higher fill factors were also reported due to the addition of 5% Sr [65], but the amount of Sr introduced was limited to very little (<10%).

2.3.2 Processability and Stability of Perovskites

The photovoltaic industry requires upcoming technologies to be very robust and demonstrate long-term stability. To be able to compete with Si-based solar cells, PSCs should match or get better than the conventional degradation rate of 0.5% per year – ensured over 25 years [66]. However, the volatile nature of the organic cations tends to accelerate the degradation under moisture and heat conditions, especially when the temperature is around 85 ^{0}C [67]. Since the stability of the perovskites is largely owed to the structural integrity and configuration, sizes of the A and X ions in the ABX_3 configuration play a significant role in the stability [68]. One of the reports that reported better moisture stability is due to partial replacement of the large I ion with the smaller Br ion and the formula being $MAPb(I_{1-x}Br_x)_3$, thereby transforming the tetragonal structure to cubic [69]. Some of the other efforts were dedicated to improving stability by employing metal-oxide charge transport layers [70] and performance by incorporating smaller cations into the perovskite matrix [71]. In that regard, the 'mixed cation' and 'mixed halide' perovskite compositions – $FA_{0.83}Cs_{0.17}Pb(I_{0.6}Br_{0.4})_3$ were studied extensively, and the Cs

insertion was deemed to improve the stability through the transition from black to yellow phase [72,73]. Devices based on the above composition maintained 80% of "post-burn-in" efficiency after 650 hours while the same efficiency was maintained after 3400 hours in sealed conditions [74]. Alternative methods of improving stability would be to use inorganic charge transport layers, which last longer and slow the degradation of the devices [75,76].

The majority of the research on perovskites was conducted on planar architectures, although inverted architectures were known for lower processing temperature and simpler fabrication routes [77,78]. As mentioned earlier, triple-cation perovskites proved to demonstrate better performance and stability; however, investigation of this composition of perovskites in inverted architectures is limited and hence a necessary thrust for progress towards commercialization. The stability of solar cells is a pre-requisite for proper working and performance due to the possibility of exposure to various conditions. The materials used should therefore be able to retain the stability in a given atmosphere over extended durations. There is still a long way to go before PSCs can reach full-scale commercialization on large scale panels with an area greater than $12cm^2$ [79]. Various methods such as screen-printing, slot-die coating, spray-coating, and soft-cover coating methods have been developed towards preparing PSC modules on the scale of tens of sq. centimeters [80]. Alternative processing methodologies are required to achieve large scale deployment of perovskites in the industry.

CHAPTER 3

IMPACT OF EXCESS LEAD ON THE STABILITY AND PHOTO-INDUCED DEGRADATION OF LEAD HALIDE PEROVSKITE SOLAR CELLS

3.1 Introduction

Organic-Inorganic lead halide perovskite solar cells (PSC) have emerged as one of the most promising thin-film photovoltaic technologies. This emergence is attributed to the cost-effectiveness of their manufacturing methods and low-temperature synthesis processes [22,81,82], and their high power conversion efficiencies (PCE) [21,75,83–86]. However, instability in device performance due to photo-degradation is a major concern for the advancement of perovskite solar cells [87–89]. Several reports show that prolonged illumination to sunlight leads to device degradation [90,91]. Such degradation is attributed to several factors. Ito *et al.* have reported that perovskite film degradation could be a key reason [92]. Device degradation has also been attributed to a combination of light and thermal influences [93]. Interfacial degradation between the transport layer and the corresponding electrode has also been reported [94]. In this investigation, the formation of trap states due to ion migration is also a reason for the degradation in device performance [95–97]. Hence, the analysis of these defects [98] is important, and so is the elucidation of their impact on the stability of PSCs.

Lead iodide residue is commonly formed during solar-radiation induced degradation of PSCs, together with trap states in different environments [93,99]. A group of investigators has demonstrated improved device stability by using crosslinking additives, compositional engineering, and the addition of other precursor materials [100–102]. Additives such as Benzoquinone are added to suppress the occurrence of trap states,

and thereby, to improve device stability [103]. However, solar-radiation induced degradation needs to be further explored since solar cells typically operate under constant illumination.

In this work, glass/ITO/PEDOT: PSS/$MAPbI_3$/PCBM/Ag devices were fabricated with an inverted architecture, using lead acetate as source material. Characterization of the devices shows that adding excess lead into the precursor solutions (that were used for the perovskite active layer) results in higher stability (for exposure to prolonged illumination) compared to samples fabricated with no excess Pb in their precursor solutions. This increased stability against prolonged exposure is attributed to the formation of PbI_3 in the perovskite layers.

3.2 Experimental Procedure

The experimental procedure in this study was similar to that reported for our previous work [104]. Methylammonium iodide was purchased from Dyesol, and lead acetate trihydrate ($Pb(OAc)_2 \cdot 3H_2O$) was purchased from Alfa Aesar. Both materials were used as received. An initial perovskite precursor solution was prepared by dissolving 3.0 mmol MAI and 1.0 mmol $Pb(OAc)_2 \cdot 3H_2O$ in 1 mL of anhydrous DMF solution. Three different perovskite solutions were then prepared with differing excess Pb concentrations: 0 mol%, 5 mol%, and 10 mol%.

Indium-doped tin-oxide (ITO) coated glass substrates were cleaned in the following sequence: detergent solution, deionized water, acetone, and isopropyl alcohol, followed by UV-ozone treatment for 10 min for each process step. The substrate was 2.5cm×2.5cm in size, and the active device area (defined by the overlapping of ITO and Al electrodes) was 0.2 cm^2. Poly(3,4-ethylene dioxythiophene): poly(styrene sulfonate) (PEDOT: PSS,

Clevious PVP Al4083 filtered through a 0.45 μm filter) was spin-coated onto the ITO substrates at 4000 rpm, followed by a thermal anneal at 130 ^{o}C, for 15 min in a glovebox. $Pb(OAc)_2$:MAI solutions were then spin-coated onto the PEDOT layers for 60s at 4000 rpm. A thermal anneal was then performed at either 80 ^{o}C for 15 min or 90 ^{o}C for 5 min to form the perovskite films. Phenyl-C_{61}-butyric acid methyl ester (PCBM, Aldrich) was dissolved in chlorobenzene, to result in a concentration of 20 mg/mL, and was then spin-coated on top of the perovskite layer at 1000 rpm for 30 sec. The devices were then completed, with thermal evaporation of an 80 nm thick Al electrode.

The as-prepared samples were characterized using scanning electron microscopy (SEM-XL30 Environmental FEG (FEI)). X-ray diffraction (XRD) measurements were performed with an X-ray Diffractometer using an anode tension of 40 kV and a filament current of 45 mA to produce Cu $K\alpha$ radiation. A step-size of 0.01 degrees was used during the analysis. UV-Vis absorption spectra were recorded using a Cary 5000 UV/VIS spectrometer. The lifetimes of charge carriers were determined from Photoluminescence (PL) characteristics, using a Picosecond Time-Correlated Single Photon Counting (TCSPC) Spectrofluorometer. The PL decay time for each perovskite film was monitored at 775 nm with a femtosecond Ti:S laser (Spectra Physics) with a frequency doubler and a pulse selector. The excitation wavelength was fixed at 425 nm.

Current density-voltage (J-V) characteristics of the solar cells were measured using simulated AM 1.5 global solar irradiation (100 mW/cm^2) from a xenon-lamp solar simulator (Spectra Physics, Oriel Instruments, USA). For illumination aging, the samples were placed under the solar simulator for prolonged time intervals before recording the J-V characteristics. In order to minimize the influence of moisture, the devices were placed

into sealed environments and transferred to characterization tools.

3.3 Results and Discussion

The degradation of the current density of the devices as a function of time under constant illumination is shown in Fig. 3.1. As reported in our previous work, 5% excess Pb content resulted in the highest PCE, with a value of 12.9 %, initially [104]. Following the 5% device, 10% and 0% excess Pb devices with PCE values of 8.8 % and 7.2 %, respectively. Under simulated solar illumination, the device's PCE followed a similar trend of degradation over time, as shown in Fig. 3.2. The degradation trend of the PCE shows that the 5% Pb structure retained the highest efficiency after 1 hour of constant illumination when compared to the other samples. Various solar cell device parameters before and after degradation are tabulated in Table 3.1. While the J_{SC} degraded significantly, the V_{OC} and FF remained similar for all of the devices after illumination aging. The degradation trends of V_{oc} and FF of devices (measured every 10 minutes for 1 hour) are plotted in Fig. 3.3a and 3.3b, respectively.

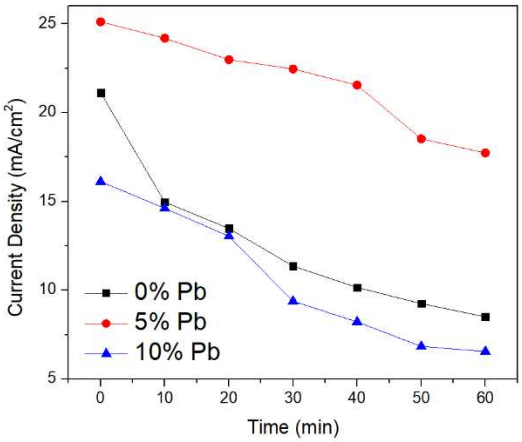

Figure 3.1. J_{SC} degradation with time

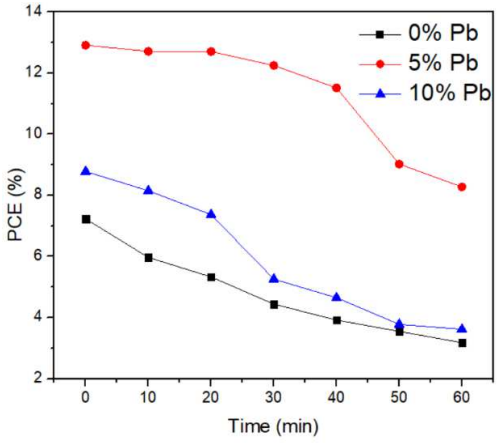

Figure 3.2 PCE degradation with time

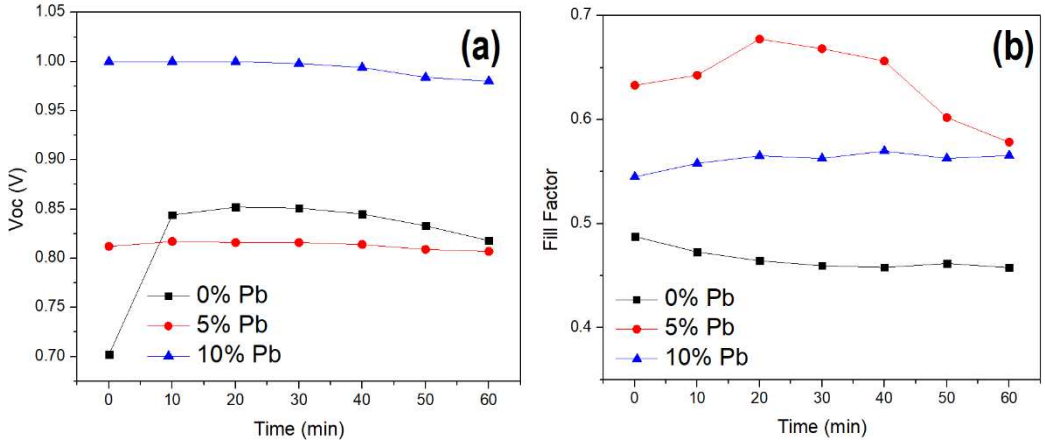

Fig. 3.3 Photo-degradation of photo-voltaic properties of PVS device with illumination time (T), (a) V_{OC} - T curve, (b) FF - T curve

Table 3.1. Solar cell device parameters for different devices

Sample details	PCE (%)	J_{SC} (mA/cm^2)	V_{OC} (V)	FF
0% initial	7.23	-21.12	0.84	0.48
0% degraded	3.18	-8.50	0.81	0.45
5% initial	12.91	-25.11	0.81	0.63
5% degraded	8.27	-17.73	0.80	0.57
10% initial	8.78	-16.11	1.00	0.56
10% degraded	3.62	-6.54	0.95	0.54

To further investigate the behavior of the devices, absorbance spectra were measured before and after illumination, and are shown in Fig. 3.4. The absorbance does not show any significant reduction with time, for all of the samples. However, a distinct hump is observed around 500 nm [99] for both 5% and 10% excess Pb samples. This can be attributed to an increased presence of PbI_2 in these samples when compared to the 0% excess sample [99,105]. The higher PbI_2 is a direct result of higher Pb precursor concentrations. The reaction for the formation of $MAPbI_3$ and its decomposition can be summarized as follows [99,104]:

$$Pb(CH_3COO)_2+3CH_3NH_3I \rightarrow CH_3NH_3PbI_3+2CH_3NH_3CH_3COO\uparrow \quad (3.1)$$

$$CH_3NH_3PbI_3 \rightarrow PbI_2+CH_3NH_2+HI \quad (3.2)$$

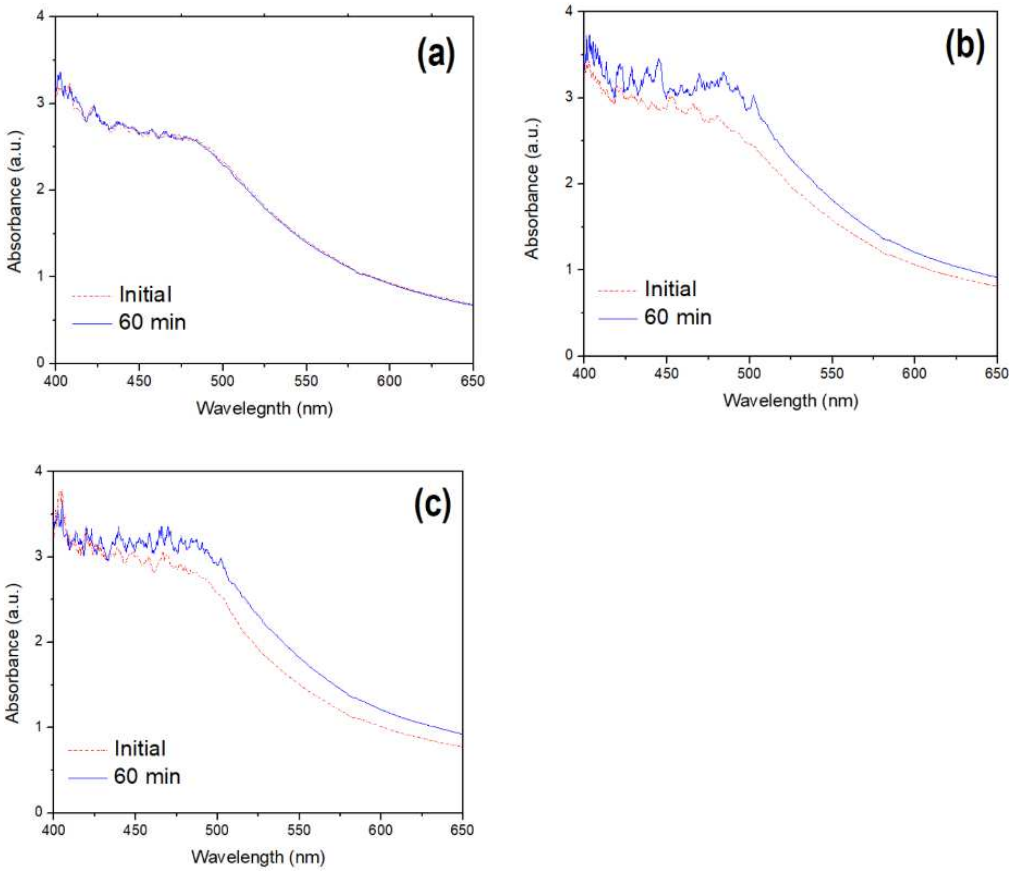

Fig. 3.4 UV-Vis spectra of PVS layer derived from solutions with a) 0% excess Pb, (b) 5% excess Pb, and (c) 10% excess Pb

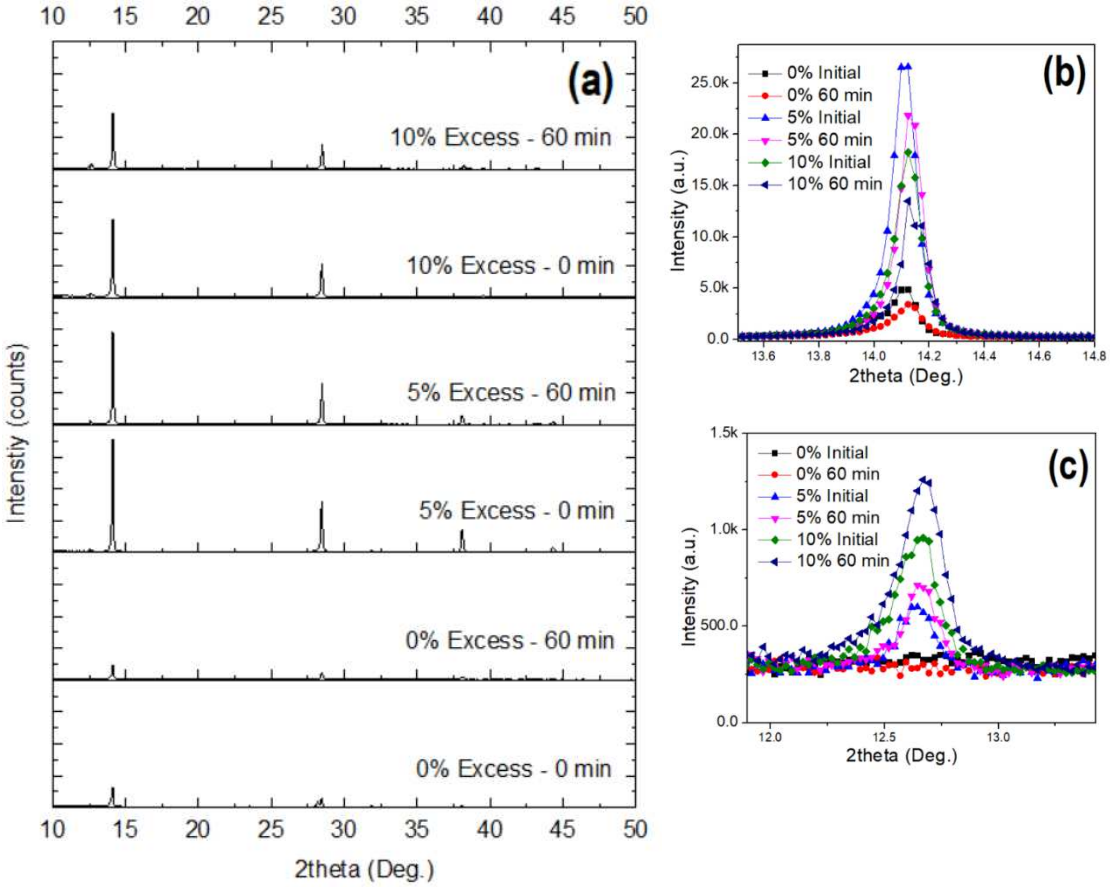

Fig. 3.5 a) XRD spectra of all samples before and after degradation, b) $MAPbI_3$ peak, and c) PbI_2 peak enlarged

The formation of PbI_2 is further evident from the XRD data shown in Fig. 3.5. The initial patterns showed that the $MAPbI_3$ peak is highest for the 5% excess Pb sample when compared to the 0% and 10% excess Pb samples. Photo-degraded samples show a decrease in the crystallinity of the (110) peak. This indicates structural degradation occurring due to the decomposition of $MAPbI_3$ and the formation of PbI_2. Zoomed graphs (Figs. 3.5b and 3.5c) show a decrease in the peak intensity from the $MAPbI_3$, with a simultaneous increase in PbI_2 at 12.67^0 in all of the samples. Since the 0% excess sample does not have any excess Pb, the intensity of the newly formed PbI_2 is barely visible when compared to the higher

intensities from the 5% and 10% excess Pb samples. For correlation with these XRD results, SEM images were taken of the samples before and after degradation. However, no significant changes were visible in any of the images, as shown in Fig. 3.6.

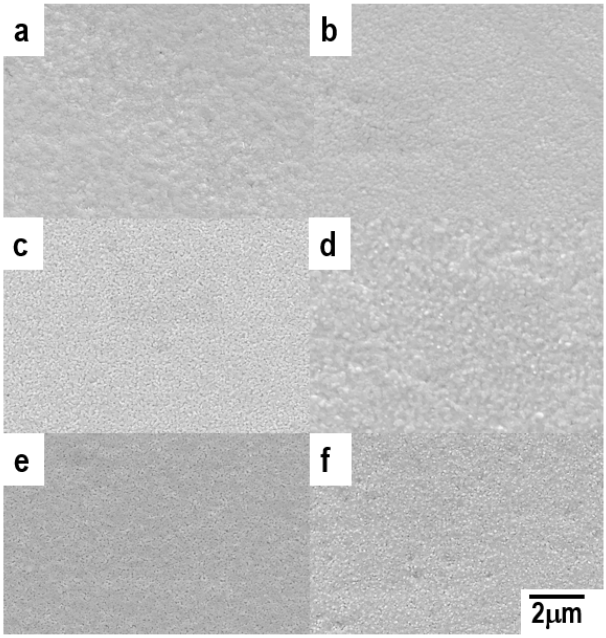

Fig. 3.6. Surface morphologies of PVS films before and after photo-illumination a), c) and e) for pristine samples derived from solutions with 0%, 5%, and 10% excessive Pb, respectively and b), d), and f) for photo-degraded samples derived from solutions with 0%, 5% and 10% excessive Pb, respectively

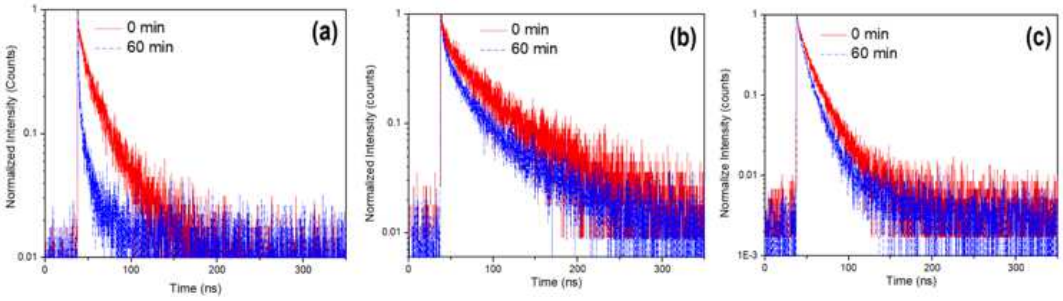

Fig. 3.7 TRPL spectra of pristine and photo-degraded PVS layer. a) 0% excess Pb, b) 5% excess Pb, and c) 10% excess Pb

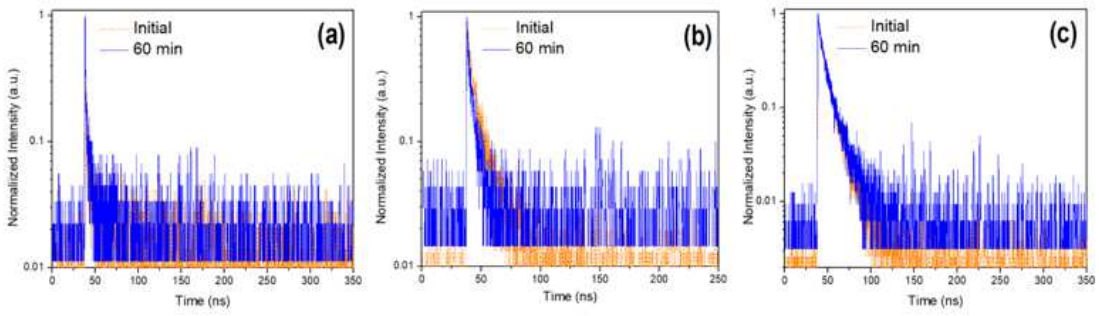

Fig. 3.8 TRPL spectra of pristine and photo-degraded PVS layer with PCBM. The PVS layers are derived from solutions with a) 0% excess Pb, b) 5% excess Pb, and c) 10% excess Pb

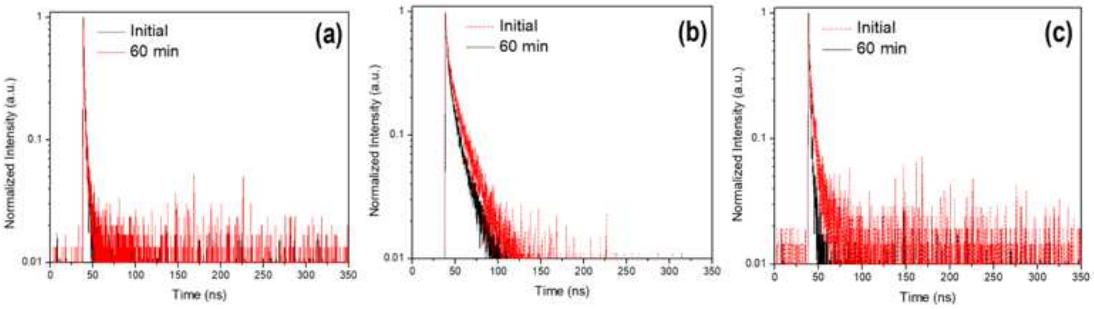

Fig. 3.9 TRPL spectra of pristine and photo-degraded PVS layer with PEDOT. The PVS layers are derived from solutions with a) 0% excess Pb, b) 5% excess Pb and, c) 10% excess Pb

Table 3.2. TRPL fitting parameters of PVS active layer

Sample details	A1	A2	τ_1 (ns)	τ_2 (ns)	τ_{PL} (ns)	χ^2
0% initial	49.34	36.99	8.48	30.41	17.87	0.87
0% degraded	134.29	16.22	1.61	18.00	3.37	1.40
5% initial	18.77	26.19	11.22	57.80	38.35	0.99
5% degraded	95.48	44.96	9.53	55.99	24.40	1.36
10% initial	171.04	94.57	8.82	23.79	14.15	1.15
10% degraded	410.62	91.80	7.50	22.82	10.29	1.49

Table 3.3. TRPL fitting parameters of PVS/PCBM

Sample details	A1	A2	τ_1 (ns)	τ_2 (ns)	τ_{PL} (ns)	χ^2
0% Initial	58.63	4.45	0.77	11.41	1.52	0.85
0% degraded	30.05	5.77	0.98	5.40	0.71	83.89
5% Initial	209.22	91.20	8.74	22.90	13.03	1.15
5% degraded	96.73	47.17	5.96	18.26	9.99	0.87
10% Initial	261.04	97.82	5.86	14.97	8.34	1.06
10% degraded	65.99	56.01	4.99	13.78	9.02	1.78

Table 3.4. TRPL fitting parameters of PVS/PEDOT

Sample details	A1	A2	τ_1	τ_2	τ_{PL}	χ^2
0% Initial	233.10	12.89	1.57	7.28	1.86	1.17
0% degraded	122.82	16.47	1.29	6.58	1.91	0.97
5% Initial	160.72	71.84	4.47	21.49	9.72	1.00
5% degraded	460.63	116.69	3.95	20.53	7.30	1.32
10% Initial	75.09	14.38	2.35	9.28	3.85	0.93
10% degraded	348.74	107.61	2.35	9.28	3.98	0.97

To further understand the effects of PbI_2 formation, Time-Correlated Photoluminescence (TCPL) spectra were obtained from the PVS layers and the PVS-combined PCBM layers. The spectra are shown in Fig. 3.7, which presents the PL spectra of the perovskite active layer before and after degradation. The PVS and PVS/PCBM layers were deposited on glass, and the excitation laser irradiation was incident from the glass-side (or rear side) with the detector on the front-side of the sample. The photoluminescence decay kinetics were fitted using a biexponential decay function $I(t) = A_1e^{-(t/\tau_1)} + A_2e^{-(t/\tau_2)}$. To easily compare the total lifetimes of all of the perovskite films, the values of τ_{PL} were determined by using the relationship $\tau_{PL} = \alpha_1\tau_1 + \alpha_2\tau_2$; where $\alpha_1 = A_1/(A_1+A_2)$ and $\alpha_2 = A_2/(A_1+A_2)$. The fitting parameters (τ_1, α_1, τ_2, α_2) and the corresponding errors (χ^2) of the photoluminescence decay are listed in Tables 3.2 and 3.3 for the PVS and PVS/PCBM

devices, respectively. The results show that the 0% excess samples experience a significant decrease in τ_2 (characteristic recombination lifetime) values from 30 ns to 18 ns. However, the 5% and 10% excess Pb samples did not show a significant reduction in lifetimes (from 57.8ns to 55.99ns and 23.79ns to 22.82ns, respectively) when comparing their initial and final values. The PL spectra of the PVS active layer with the PCBM layer are shown in Fig. 3.8 for all the samples. A similar effect in decay for excess Pb is observed in all of the samples. Inspection of the 0% excess Pb sample shows a degradation of τ_2 from 11.41ns to 5.4ns. In contrast, 5% and 10% excess samples show a lesser reduction from 15.3 ns to 14ns and 15.0 to 13.8 ns, respectively.

The formation of the PbI_2 phase can have two distinct effects: *i*) grain boundaries in the perovskite layer are regions of defects that can be modified by the PbI_2, and *ii*) PbI_2 can form at the interface between the active layer and the charge transport layer. Electrons or holes are quenched at grain boundaries, and this blocks the efficient separation of the charge carriers. PbI_2 can have a passivating effect at the grain boundaries, as shown in Fig. 3.10. This will then reduce carrier recombination at such boundaries [106,107]. The result is the retaining of initial lifetime values even after degradation, as seen in the TCPL results. These findings suggest that the nucleation and growth of PbI_2 at grain boundaries can help retain carrier lifetimes for specific exposure times.

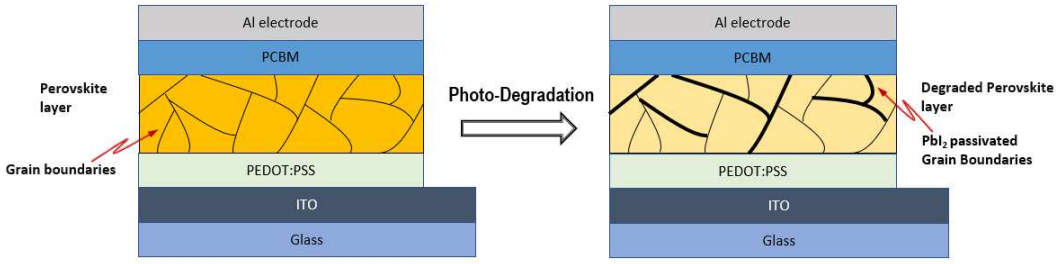

Fig 3.10. Schematic of the passivation effect of PbI_2 on grain boundaries

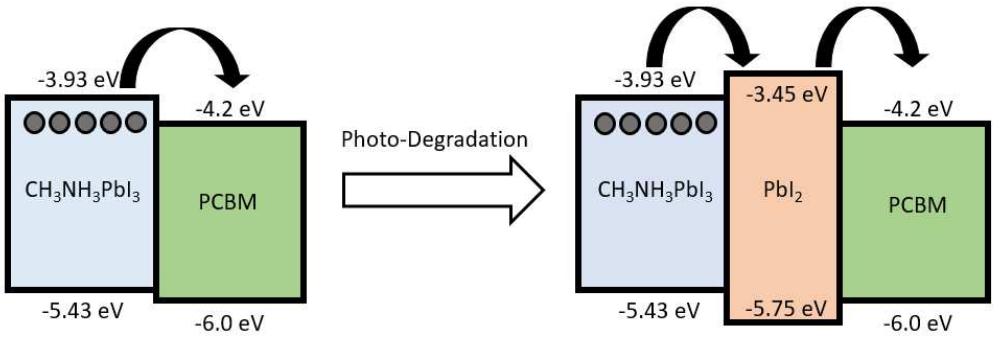

Fig. 3.11. Modified band structure due to the effect of PbI_2 formation at the interface with PCBM

PbI_2 can also form at the interface between the active layer (AL) and the charge transport layer (CTL). In an inverted planar structure, PCBM is deposited on top of the active layer. If PbI_2 is present at the AL-CTL interface, it can alter the band structure at the interface, as shown in Fig. 3.11. The conduction band minimum (CBM) and valence band maximum (VBM) of $MAPbI_3$ occur at -3.93eV and -5.43eV, respectively [108]. For PbI_2, the CBM and VBM are at -3.45eV and -5.75eV, respectively, according to Chen *et al*. [107]. Hence, when PbI_2 forms at the AL-CTL interface during prolonged illumination, this creates a barrier that acts against the extraction of electrons (at the interface between the active layer and the PCBM). This alters the band structure, and as a result, the PCE continues to be stable for longer durations, as shown in our earlier results (Figs. 3.1 and 3.2). However, a higher concentration of PbI_2 has a negative influence, since the extraction efficiency is affected, resulting in faster degradation of the device as in the case of the 10% excess samples. The results from TCPL analysis show that the PbI_2 has more influence at the interface between the active layer and PCBM rather than with PEDOT. This is because a significant reduction in carrier lifetimes was not observed in the PVS/PEDOT samples, before and after illumination, for all sample concentrations were shown in Fig. 3.9. This is

due to the fact that PbI_2 is formed mostly at the PVS/PCBM interface, and at grain boundaries [106,107].

These results show that 5% excess Pb is the optimum concentration in the precursors, and the resulting formation of PbI_2 is sufficient to make the device stable after prolonged illumination when compared to samples with 0% or no excess Pb precursor. Samples with 10% excess Pb content result in much higher concentrations of PbI_2, which, combined with poor film quality, has detrimental effects on the PCE.

3.4 Conclusion

This work compares the stability of PCE for three groups of samples with varying excess Pb content in the precursor solution. Devices using films with 5% excess Pb are the most stable of all, with more than 50% of the initial PCE being retained after prolonged illumination for 1-hour. PbI_2 was found to be a product of light-induced degradation, as confirmed by absorbance spectra and XRD analysis. However, substantial degradation of the $MAPbI_3$ complex is also observed. The formation of PbI_2 contributes to the stability of the device under simulated solar illumination due to the passivation of grain boundaries in the active layer and modification of the band structure at the interface between the active layer and the charge transport layer. This work shows that utilizing excess Pb in perovskite solar cells can improve stability under illumination.

CHAPTER 4

IMPROVED PERFORMANCE OF INVERTED PEROVSKITE SOLAR CELLS DUE TO THE INCORPORATION OF ZIRCONIUM ACETYLACETONATE BUFFER LAYER

4.1 Introduction

Organic-Inorganic lead halide perovskite solar cells have emerged as the most promising thin-film photovoltaic technology. Solution-processed solar cells using organic-inorganic hybrid perovskite compounds have garnered quite an interest recently [34,109,110]. High power conversion efficiencies have been reported to show promising potential for competing with existing technologies [72,75]. Apart from improving the quality of the active layer, higher performances achieved due to modifications to the interfaces between the photoactive layer and the electrode were equally important [111,112]. Amongst the modifications introduced, inorganic materials such as ZnO, TiO_x, MoO_x, NiO, WO_x, and ZAC have shown promise for replacing conventional layers on a long term basis in both in regular and inverted architectures [113–119]. In the case of the inverted devices, these layers served as a cathode buffer layer for PTB7 (polymer) and perovskite-based solar cells. With the quality of the perovskite film optimized heavily, the power conversion efficiency (PCE) can be pushed further only by concentrated efforts in realizing quality interfacial layers [120]. However, the processing methodologies and materials presented thus far still lack robustness to their approach and systemic consideration of potential reproducibility.

Zirconium acetylacetonate (ZAC) is a relatively new cathode buffer layer that has been used. The initial work of Tan *et al.* demonstrates the use of this layer in a regular device structure [118], followed by Hancox *et al.,* who reported the use of ZAC in inverted solar cells [121]. Fan *et al*. reported higher performances with the use of PTB7 based inverted architecture solar cells [119]. While employing ZAC as a secondary buffer layer allows for charge extraction with record efficiencies [122]. Zhang *et al.* reported improved fill factor values due to the incorporation of a ZAC layer [123]. These developments, combined with an abundance of availability and easy processability without the need for additional annealing steps [124], make ZAC one of the promising materials for large-scale applications. Despite the above work, certain questions remain regarding the compatibility of the secondary cathode buffer layer with the active layer itself and the other cathode layer, Phenyl-C_{61}-butyric acid methyl ester (commonly known as PCBM), in inverted device structures and the effect of thickness on charge transfer kinetics and functionality of the device.

In this work, ZAC solutions of different concentrations were prepared in iso-propyl alcohol (IPA), which is less polar than other commonly used alcohol solutions, and optimized parameters for maximum efficiency while using a more robust approach in the processing of the secondary cathode layer. Our perovskite solar cell (PSC) devices used an inverted configuration and dual cathode buffer layers of ITO/PEDOT: PSS/Perovskite/PCBM/ZAC/Al. The perovskite used in our study was methylammonium lead iodide and prepared from lead acetate precursors and dimethylformamide. IPA was found to be the best solvent to dissolve zirconium precursor, and it gave consistent and reproducible results when compared to ethanol and methanol. ZAC concentration was

optimized to 1.5mg/ml in IPA to give an average PCE of 14.3% with the highest PCE of 15.2%, compared to 12% PCE of a control device without the ZAC layer. Our results demonstrated the potential for using ZAC in IPA for more consistent applications in future PSC devices.

4.2 Experimental Procedure

The PSC active layer is prepared according to our previously optimized procedure using excess Pb in the precursor, which is briefly described here [125]. Poly (3,4-ethylene dioxythiophene): poly (styrene sulfonate) (PEDOT: PSS), purchased from Ossila, was spin-coated onto ITO substrates at 4000 rpm for 60 s followed by thermal annealing at 130 °C for 15 min. Methylammonium iodide (MAI) was purchased from Dyesol, and lead acetate trihydrate ($PbAc_2$. $3H_2O$) was purchased from Alfa Aesar, and both were used as received. 2.7 mmol MAI and 0.9 mmol $PbAc_2.3H_2O$ were dissolved into 1mL anhydrous dimethylformamide (DMF) solution resulting in a solution concentration of 0.9 M. For preparing Pb excessive solution, ($MAI/PbAc_2$ = 3:1.05) were used. This solution was then spin-coated onto the PEDOT layer at 4000 rpm for 60 s followed by an anneal at 80 °C for 12 min. PCBM dissolved into chlorobenzene (20 mg/ml) was spin-coated on the top at 1000 rpm for 30 s. Zirconium acetylacetonate purchased from Aldrich was dissolved into different alcohols to prepare solutions of concentration 1mg/ml. ZAC was spin-coated onto the PCBM at 3000 rpm for 30 s. For device fabrication, a 70 nm thick Al electrode was thermally evaporated, which resulted in a device area of 0.2 cm^2.

The as-prepared devices were characterized for current-density measurements under simulated AM 1.5 solar irradiation (100 mW/cm^2), which is a xenon-lamp based solar simulator (Spectra Physics, Oriel Instruments, USA). The steady-state

photoluminescence (PL) spectra of the samples were tested using Reinshaw InVia spectroscopy system with an x100 objective lens and a laser source of wavelength 488 nm. The charge carrier lifetimes were measured by Picosecond Time-Correlated Single Photon Counting Spectrofluorometer (TCSPC). The PL decay time was observed at 775 nm after excitation from a Ti:S laser (Spectra Physics) at 425 nm. The PL decay kinetics were fitted to a bi-exponential decay function. Surface morphology was measured using scanning electron microscopy (SEM-XL30 Environmental FEG (FEI) and atomic force microscopy (Bruker Multimode 8). X-ray diffraction analysis was done with a Rigaku diffractometer. The tension was 40 kV on the Cu anode, and the filament current was 20 mA.

4.3 Results and Discussion

The perovskite active layer used in this research and the architecture are the same for all devices and prepared according to our previously reported work [125,126] (see Fig. 4.1a). The XRD and SEM images of the perovskite on ITO shown in Fig. 4.1b and 4.1c. XRD results reveal the dominant peak of $MAPbI_3$ at 14.26°. The SEM reveals the smooth formation of the layer with few pinholes or pores.

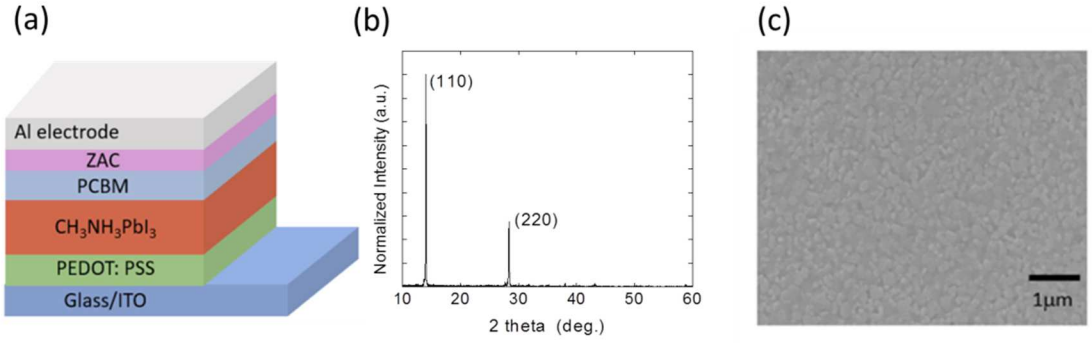

Fig. 4.1 a) Schematic of the device structure with the ZAC layer, b) XRD patterns, and c) SEM image of the perovskite layer of perovskite used in all samples.

4.3.1 Solvent Optimization

To investigate the effect of different alcohol-based solvents, devices with the ZAC layer using solutions of either ethanol, methanol, and IPA at 1mg/ml were prepared. Our observations indicated that solvent played a critical role in the formation of a good layer of ZAC.

Ethanol and methanol are the most commonly used solvents that are alcohol-based, while chloroform is another proposed solvent to dissolve the precursors [13-18]. Although the above-mentioned solvents were very good at dissolving the precursor, according to our experimental observation, prove to be corrosive to PCBM and perovskite layers unless extreme care is adopted in the synthesis procedure. This explains why ZAC layers, when dissolved in ethanol or methanol, require very careful control of the spin coating process; otherwise, it will result in dissolving the underlying PCBM/perovskite layers [127]. IPA, on the other hand, is not as polar as ethanol or methanol and is considerably robust in its processing use for coating an additional layer without any damage to underlying layers. IPA, which has a significantly lower vapor pressure and is slightly less polar, is less corrosive and more reproducible when used as the solvent for ZAC dissolution. Our results reflect these observations where ZAC dissolved in IPA gives the highest performance when compared to the other alcohols. Figure 4.2a shows the current-density characteristics of the devices prepared using ethanol and methanol. Other device parameters, open-circuit voltage (V_{OC}), current density (J_{SC}), fill factor (FF), and efficiency (PCE) for all samples are summarized in Table 4.1. Devices prepared using IPA gave a PCE of 14.03%, while those fabricated with ethanol and methanol gave 7.62% and 11.66%, respectively.

A closer look at the solar cell device parameters reveals that the V_{OC} as being significantly lower for ethanol and methanol-based devices; while, IPA based devices show a high V_{OC}. Open-circuit voltage has a direct implication on device performance, and its dependence on the morphology and structure of the active layer cannot be stressed enough. Any inhomogeneities in the PCBM layer can result in direct contact of the ZAC layer with the active layer. Given that ethanol and methanol-based solvents can be detrimental to the perovskite layer, the poor physical properties result in poor V_{OC} and, subsequently, poor overall performance. IPA, on the other hand, is not as corrosive to the active layer, and so better performance is possible as the inherent structure is left undisturbed.

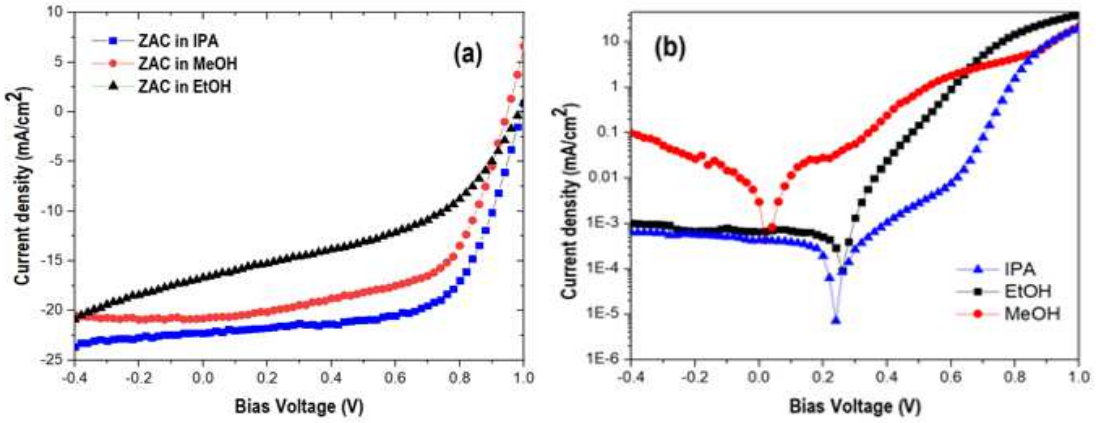

Fig. 4.2 a) Current density characteristics, and b) Dark current characteristics of ZAC in different solvents

Table 4.1. Solar cell device parameters of samples prepared in different solvents

Device details	V_{OC} (V)	J_{SC} (mA/cm^2)	FF	PCE (%)
ZAC in ethanol	0.95	-16.07	0.46	7.62
ZAC in methanol	0.94	-20.82	0.59	11.66
ZAC in IPA (PZ1)	0.99	-22.27	0.63	14.03

Figure 4.2b displays the dark current characteristics for the various solvents, and it was observed that the IPA based devices show less leakage comparatively. Both ethanol and methanol-based devices showed large leakage (about two orders of magnitude than IPA) in the given bias voltage. This is primarily due to the presence of pores and defects in the active layer (which are possibly induced due to the spin-coating of the highly polar solvents. A certain amount of bias voltage is required for the onset of dark current as of the case for IPA devices. This is due to the excellent layer formation, which results in very good suppression of charge recombination inside the device. This suppression of injection of charges effect is similar to the previous works by Hou *et al.* and Thakur *et al.,* who shared that Ta-WO_x doped perovskites and size-dependent TiO_2 nanorods in perovskites result in a shifting of the bias voltage and the onset of dark current. [127,128].

To further confirm our hypothesis that ethanol and methanol result in rough surfaces, AFM analysis of the samples prepared in different solvents was done (see Fig. 4.3). RMS values of 18 nm, 20 nm for ethanol, and methanol samples, respectively, revealed rougher surfaces when compared to the relatively smoother IPA sample with an RMS of 15 nm.

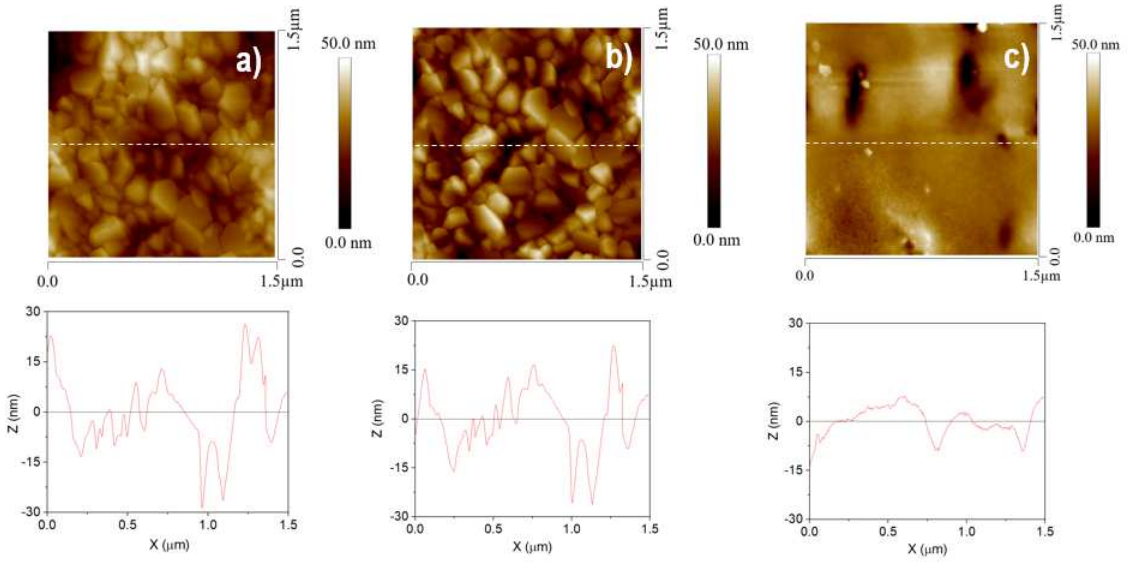

Fig. 4.3 a) ZAC in ethanol, b) ZAC in methanol, and c) ZAC in IPA

4.3.2 Concentration optimization:

The efficiency was further optimized by investigating the effect of different concentrations of ZAC in IPA. Devices with ZAC 1mg/ml, 1.5 mg/ml, and 2mg/ml and designated them as PZ1, PZ2, and PZ3, respectively, were prepared. For comparison, a control device without any ZAC, designated as P1, was also prepared. PZ2 or 1.5 mg/ml showed the best PCE of 15.2 %. Other devices, PZ1 and PZ3, showed 14.3 % and 11.2 % PCE over the control device, which showed 12.1 % PCE. The current density characteristics (Fig. 4.4a) and other density parameters (Table 4.2) were measured.

To explain the performance, the dark current characteristics of the devices were investigated. The dark current characteristics as a function of bias voltage were measured and tabulated (see Fig. 4.4b and Table 4.2). Inspection of the data reveals that leakage current was minimized, and the onset of dark current shifted to higher bias voltages as the concentration of the ZAC in the solution increases. A high concentration typically resulted in a thicker layer. In this case, 2 mg/ml was obviously the thickest layer of ZAC, and

1mg/ml was the thinnest layer. Both PZ2 and PZ3 devices suppressed charges very well and did not allow leakage due to the lesser presence of pores or defects in the layer when compared to PZ1 and the only PCBM (P1) layers. Furthermore, within IPA based devices with different ZAC concentrations, a thicker layer created a higher injection barrier, which prevented the leakage until a threshold of about 0.23 V was reached. This also emphasizes that a high shunt resistance was achieved in the device, which was also responsible for the high FF and, consequently, the PCE.

Figure 4.5 demonstrates that statistically, the concentration of 1.5 mg/ml gave a higher efficiency compared to other concentrations. This further confirms the initial hypothesis that 1.5 mg/ml is the optimized concentration. Fig. 4.6. displays results from a stability test that was conducted with the devices being stored in a nitrogen-filled glovebox, and the efficiencies of the solar cells were mapped over a duration of 30 days. Findings show no significant improvement due to the addition of the ZAC layers, and no significant differences were observed in the degradation profiles of all devices when compared to the control device with no ZAC.

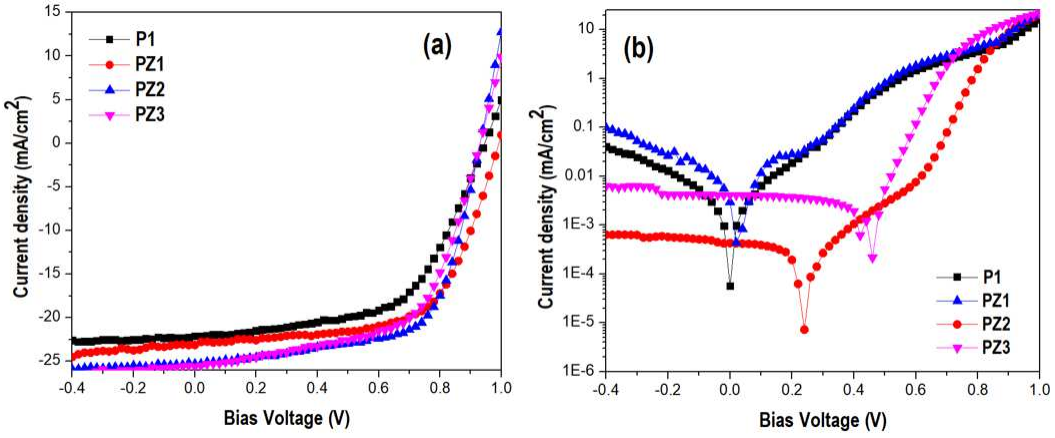

Fig. 4.4 a) Current density characteristics, and b) Dark current characteristics of devices with different ZAC concentrations

Table 4.2. Solar cell device parameters of ZAC samples prepared in different concentrations

Device details	V_{OC} (V)	J_{SC} (mA/cm^2)	FF	PCE (%)
P1 (0mg/ml)	0.94	-22.09	0.58	12.13
ZAC in IPA	0.93	-23.13	0.62	14.26
PZ2 (1.5mg/ml)	0.99	-24.50	0.64	15.21
PZ3 (2mg/ml)	1.00	-19.04	0.59	11.17

The high concentration also has a positive effect on smoothening the active layer surface and creating excellent surface morphology, as demonstrated in the AFM data in Fig 4.7. RMS values of 5nm and 2nm for 1.5mg/ml and 2mg/ml concentrations of ZAC, respectively, were obtained. A smooth film without defects is always beneficial for efficient charge extraction, and a concentration of 1.5 mg/ml in IPA gives a reasonably small number of aggregates, which might also reduce the number of defects present, and this translates to better performance [119]. However, using the 2mg/ml concentration, which results in a smoother film and much thicker, is detrimental to device performance, as explained in the electrical transport characteristics in later sections.

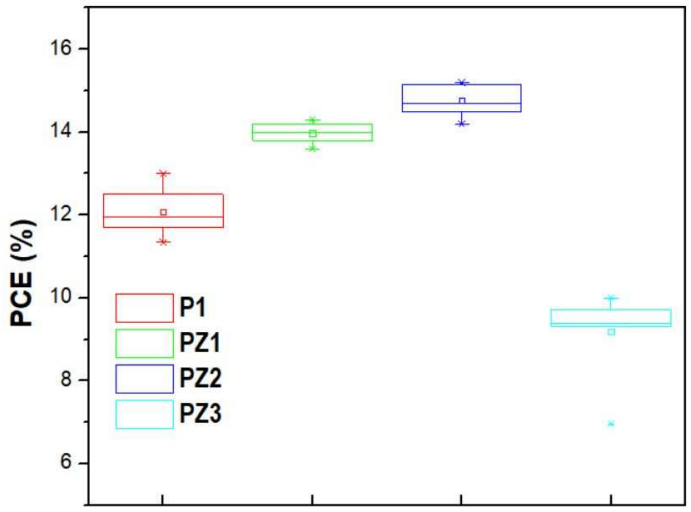

Fig. 4.5 Box plot of device efficiency for different concentrations of ZAC

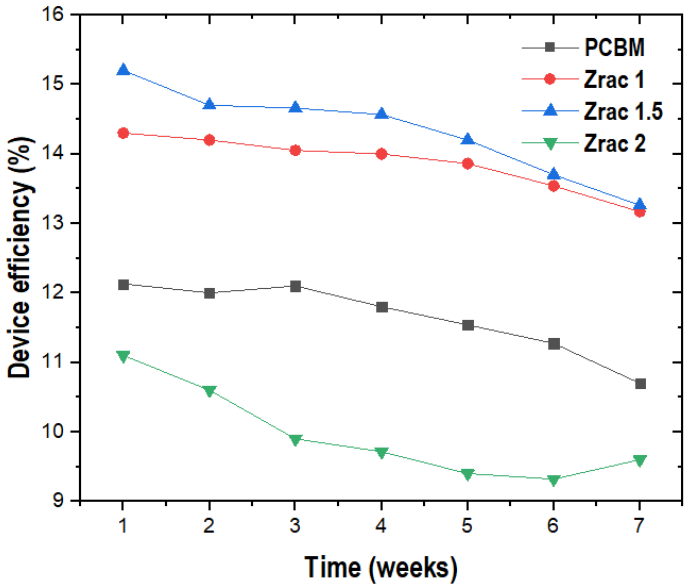

Fig. 4.6. Device performance trend of PVS prepared with different concentrations of ZAC

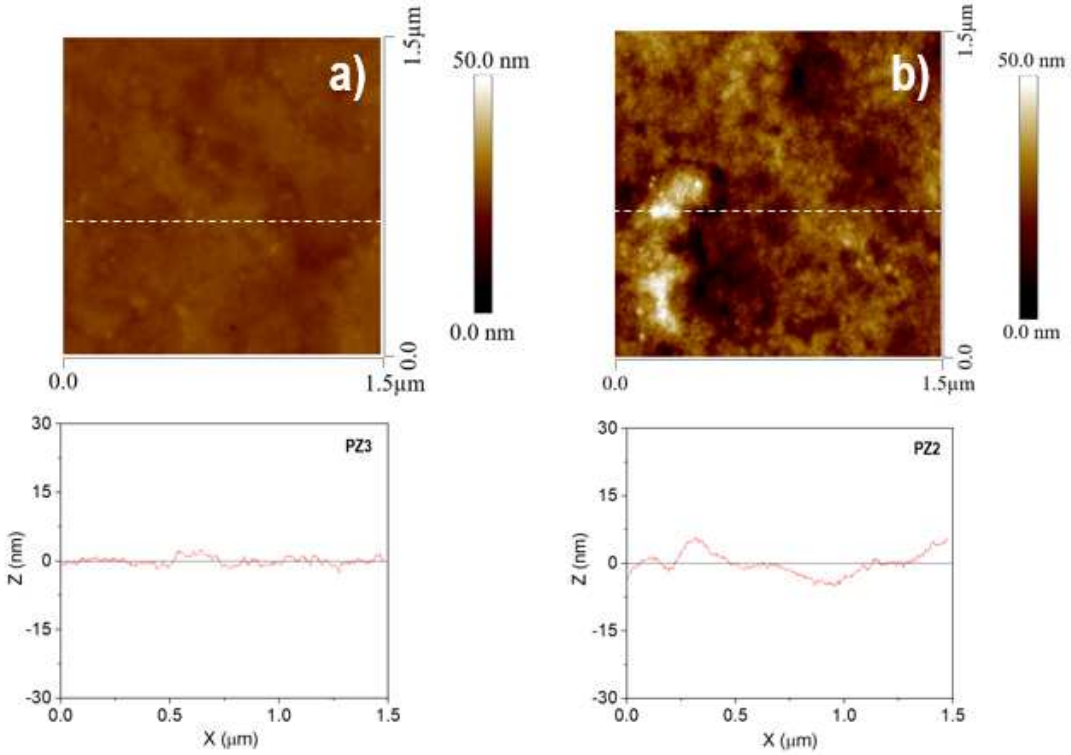

Fig. 4.7 a) ZAC in 1.5mg/ml in IPA and b) 2mg/ml in IPA

4.3.3 Optical Properties:

UV-Vis spectroscopy was used to determine the absorbance and transmittance properties of the film. ZAC layers thicknesses were measured to be around 2 nm for 1mg/ml ZAC and 3nm for 1.5mg/ml and 2mg/ml samples. Since the perovskite active layer and PCBM charge transport layer were prepared using the same recipe for all samples, the same thickness was expected for these layers. The absorbance of PVS film coated with PCBM was compared with added ZAC layers made from different concentrations, as shown in Fig. 4.8a. The absorption spectra are normalized with respect to the highest peak point in the visible region. Any observed scattering background has been subtracted from the plots. No significant difference was observed between the normalized absorption values, as also reported in previous works [123]. Transmittance spectra of PVS with ZAC

was reduced a little (about 68%) compared to having only PEDOT (about 70%) in Fig. 4.8b. This is likely due to the slightly higher thickness and is not significantly different for a control device without ZAC. Band-gap calculations from the UV absorbance plot revealed that for arbitrary thicknesses, the bandgap of PZ2 (1.5mg/ml ZAC) was about 3.50 eV and that of PZ3 (2mg/ml) was 3.62 eV. This increase in bandgap explained the slightly inferior absorption values and influence on performance. The band-gap calculated for PZ2 agreed with existing literature [123]. Plots related to band-gap calculations for PZ1 and PZ2 are presented in Figs. 4.9a and 4.9b, respectively.

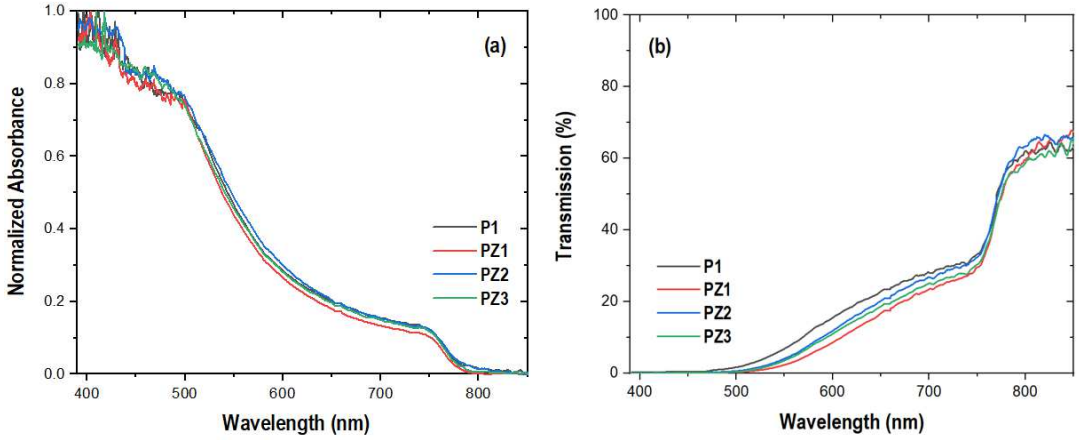

Fig. 4.8 a) Absorbance and b) Transmittance spectra of PVS with different ZAC layers

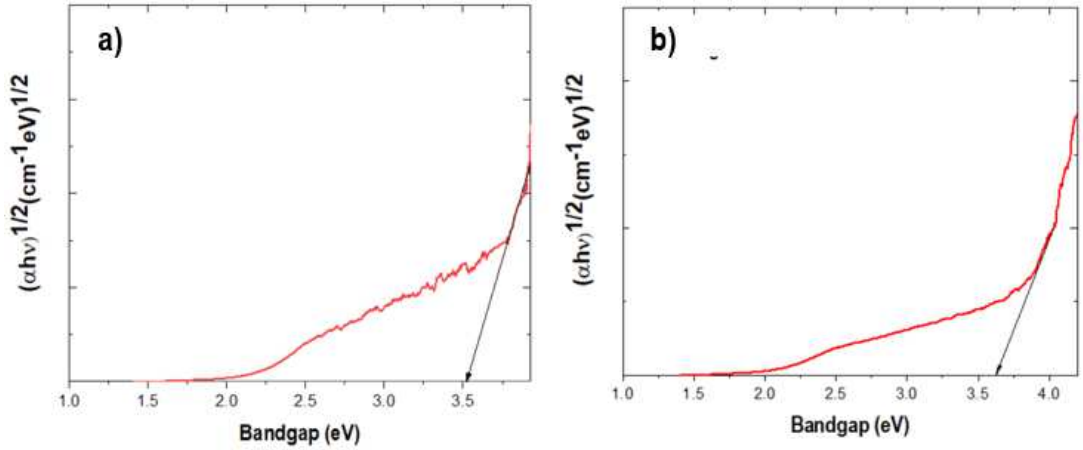

Fig. 4.9 Band-gap plots of a) ZAC 1.5mg/ml, and b) ZAC 2mg/ml samples

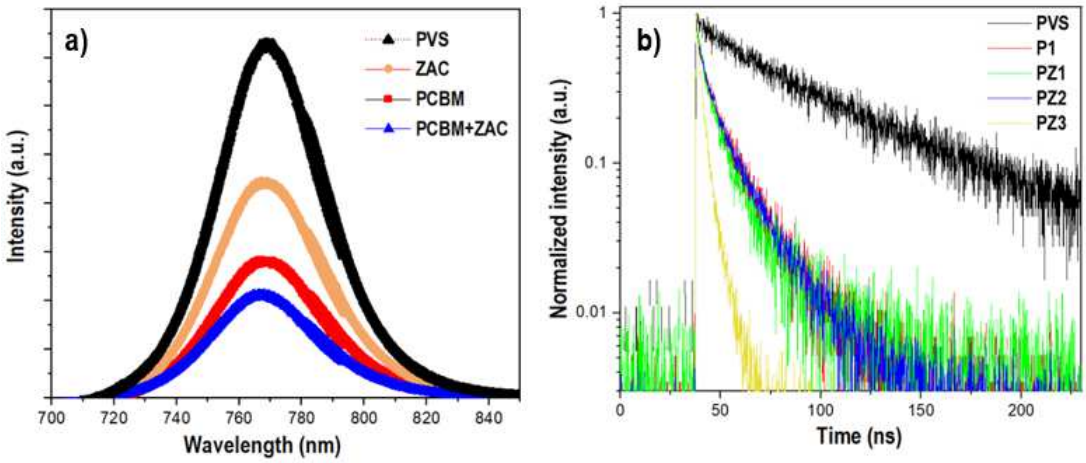

Fig. 4.10 a) Steady State Photoluminescence and b) Time-resolved Photoluminescence spectra of PVS with different ZAC layers

Table 4.3 TRPL fitting parameters of PVS with PCBM prepared in different ZAC concentrations

Sample	A1	A2	τ_1 (ns)	τ_2 (ns)	τ_{pl} (ns)	χ^2
PVS	11.06	36.99	33.53	174.55	142.09	1.02
P1	20.23	5.50	3.44	42.48	11.78	0.85
PZ1	146.97	84.93	4.88	20.45	9.68	0.80
PZ2	50.12	25.31	4.13	18.00	7.65	0.92
PZ3	294.70	3.27	3.12	14.65	3.31	1.00

Figure 4.10a displays steady-state photoluminescence (STPL) measurements from the active layer in the presence of PCBM and ZAC layers. The peak represented by PVS is used as a reference to compare the quenching efficiency. The peak labeled PCBM+ZAC shows the lowest intensity due to the combination of PCBM and ZAC layers resulting in more effective quenching of the generated charge carriers when compared to the peaks

with only PCBM and only ZAC. The concentration of the ZAC layer used in the STPL measurement is 1.5 mg/ml, which is the optimized concentration for high efficiency.

Figure 4.10b shows the charge transport kinetics of the perovskite active layer as the reference spectra labeled PVS, and also in the presence of PCBM and different concentrations of ZAC layers measured using the time-resolved photoluminescence (TRPL). The photoluminescence decay kinetics data arise from a fit to a bi-exponential decay function $I(t) = A_1e^{-(t/\tau_1)} + A_2e^{-(t/\tau_2)}$. The fast decay component, τ_1, is representative of trap-assisted recombination at grain boundaries, and the slow component, τ_2, is representative of radiative-recombination mechanisms inside the bulk [129]. Table 4.3 displays the estimated charge carrier parameters. Inspection shows that the PZ3 (2mg/ml) sample has a very low total lifetime (τ_{pl}=3.31ns); while the PZ2 (1.5mg/ml) sample has a slightly higher lifetime of 7.65 ns. While PZ1 also has a reduced lifetime of 9.68ns, further inspections show that this value is still low when compared to the decay from the PEDOT only sample, represented by the P1 peak (11.78ns). The decreasing lifetime was attributed to increasing concentration phenomena due to the insulating nature of ZAC [122], which comes into effect as the thickness of the layer was increased. This insulating property of the ZAC layer was the reason why the charges were trapped much faster than their low concentration counterparts. In addition, the ZAC layer obtained from a higher concentration solution is smoother and more compact, which means the PCBM/ZAC layer is effectively contacted with the PVS layer and facilitates the quenching of the carriers. However, if the ZAC film thickness is too high, the carrier transport from the ZAC to the electrode is blocked, resulting in the poor performance of the high ZAC concentration film (11.17% PCE) when compared to the lower concentration ones (15.26% PCE).

4.4 Conclusion

In summary, an inverted PSC was demonstrated with the addition of a secondary cathode buffer layer of ZAC dissolved in IPA. IPA as the solvent for ZAC was beneficial when compared to the commonly used ethanol and methanol, due to its lower polarity and robust synthesis procedure. Further optimization of the concentration of the layer to 1.5mg/ml was shown for a PCE of 15.2%, which is higher by 25% when compared to the control device with only PCBM (12.13%). Dark current measurements and charge-transport kinetics revealed the reasons why a high concentration film created injection barriers and became insulating in nature, and this resulted in poor device performance. The effect of surface morphology on the device performance was also investigated, and it was found that the ZAC layer fills in the pinholes in the PCBM/perovskite interface resulting in a smooth surface.

CHAPTER 5

EFFECT OF SUBSTITUTING PB WITH SR IN HIGHER-ORDER USING ACETATE-DERIVED PRECURSORS IN INVERTED PEROVSKITE SOLAR CELL DEVICES

5.1 Introduction

Perovskite solar cells have come a long way since their inception in 2009, with efficiencies improving from 3.8 % to more than 25 % recently [18]. Excellent properties such as long carrier diffusion lengths and high absorption coefficients [130–132] are some of the attributes which make the perovskites perform very well and progress towards commercialization [133]. Breakthrough performances and stability levels have been achieved by substitution of methylammonium (MA) ions with formamidinium (FA) and Cesium, Iodide, and Bromide, making the hybrid structure more inorganic [51,134,135]. However, the lead (Pb) that is present in the system is questionable, given its toxic influence and corresponding environmental concern. Alternatives to Pb in the perovskite composition are critical for furthering the development of perovskites.

In the pursuit of a stable perovskite, theoretical calculations have yielded elements from group 14 to meet the condition of having the ionic radius ratio close to 1 [61,136,137]. Extensive research has spurred the exploration of Sn and Bi as potential replacements, given their suitable valence states [61,138–140]. Fast crystallization and oxidative instability were commonly reported in Sn-based perovskites [141]. Although the bandgap was made ideal (~1.3 eV) for absorption in Bi-based perovskites, the structure suffered from stability issues [142]. Ge was the other material that was used in tandem with inorganic materials to increase the stability and evaluate performance. Ge substitution demonstrated success in improving the stability at high temperatures and photo-current

density; however, corresponding open-circuit voltages very low as a consequence of Ge^{4+} formation [143,144]. Several studies based on the modified electronic and optical properties due to the substitution of Pb with other monovalent ions such as Sr, Cd, and Ca were also done [145]. Sr has a similar ionic radius compared to Pb (132pm vs. 133pm), and similar bonding patterns with halogens were indicated for both. Perez *et al.* demonstrated improved charge carrier lifetime and fill factor from the incorporation of 2 % Sr^{2+} [65]. Yao *et al.* showed high thermal stability and higher voltage resulting in a high device efficiency of 16.3 % with the inclusion of almost 5% Sr^{2+} in the perovskite [146]. Low-temperature processing was demonstrated by Lau *et al.*, with a surface enriched Sr having a passivating effect, resulting in increased lifetimes and higher open-circuit voltage of Cs based perovskite [64]. Despite these studies, the amount of Sr^{2+} incorporated was not more than 5 % of the total composition, and also, the synthesis processes involved iodide-based precursors for Pb and Sr.

$MAPbI_3$ perovskite is known to suffer from poor stability due to the hydrophilic nature of the methylamine (MA) group, where the degradation leads to the formation of PbI_2 [147]. Several studies focused on the effects of excess unreacted PbI_2 on the long term stability of devices [148,149]. New studies emerged with 2D perovskites introduced into 3D perovskites to form mixed compounds with improved stability and moisture tolerance [150–152]. While the 2D-3D mixed perovskites focused on tuning the MA cation, recent studies reported good stability of all tin-based [153] and mixed Pb-Sn [154] devices. A lot of potential exists for demonstrating improved stability with partial or full replacement of Pb with other less toxic materials such as Sn and Sr.

In this work, the first use of acetate-based precursors to achieve a 30 % replacement of Pb with Sr was demonstrated. The effects of alloying the perovskite with Sr using the acetate derived precursor on the structural, morphological, and optoelectronic properties have been investigated. An 11.23% PCE for the perovskite with 10 % alloyed Sr and 2.15 % PCE for 30 % alloyed Sr samples was demonstrated. Improved stability of 10 % alloyed Sr was observed, with only a loss of about 25% PCE, compared to more than 50 % loss of PCE for control perovskite device. The structural, morphological, and optoelectronic properties of the perovskite composition $CH_3NH_3Sr_xPb_{1-x}I_3$ with x was varied from 0-0.3, are further explored.

5.2 Experimental Procedure

The experimental procedure is similar to our previous work using lead acetate precursors [104,148]. Methylammonium iodide (MAI) was purchased from Dyesol, and both lead acetate trihydrate ($Pb(OAc)_2.3H_2O$) and Strontium acetate ($(CH_3CO_2)_2Sr$ from Sigma Aldrich. Poly (3,4-ethylene dioxythiophene): polystyrene sulfonate (PEDOT: PSS), which was used as the hole transport layer (HTL), was purchased from Xi'an Polymer Light Tech Corp. Phenyl-C_{61}-butyric acid methyl ester (PCBM) was purchased from Sigma Aldrich and used as the electron transport layer (ETL). All materials were used as received. For the perovskite solution, MAI and $Pb(OAC)_2.3H_2O$ were mixed in the ratio 1:3.05 (5% excess Pb precursor) in anhydrous dimethylformamide (DMF) to a concentration of 1M. Different solutions of Sr were prepared by tuning the amount of Sr: Pb ratios from 10 to 30 wt%. To be noted is that Sr alloyed samples were also added in 5% excess, similar to the Pb excess, as outlined in our previous works. PEDOT: PSS solution was prepared by filtering the original solution using a 0.45μm Polyvinylidene difluoride (PVDF) filter

before using. PCBM was prepared by dissolving the powder in anhydrous chlorobenzene to a concentration of 20mg/ml with overnight stirring.

Devices were prepared on patterned Indium doped tin oxide (ITO) coated glass substrates. All devices were fabricated in a planar inverted architecture. Firstly, ITO substrates were cleaned using an ultrasonicator in deionized water, acetone, and isopropyl alcohol. They were then subjected to UV-Ozone treatment for 10 min to remove organic contaminants. The substrates were then transferred to a Nitrogen filled glovebox for device preparation. PEDOT: PSS was initially filtered using a 0.45μm filter and then spin-coated onto the ITO glass at 4000 rpm for 30s followed by thermal annealing at 130 ^{o}C for 15 min. After cooling down, the perovskite solution was coated at 4000 rpm for 180s and annealed at 80 ^{o}C for 12 min. For the electron transport layer, PCBM was spin-coated at 1000 rpm for 30s without any further post-annealing. 80nm of Al was deposited via thermal evaporation to complete the device, and an area of 0.2cm^2 was defined for each device as per the shadow mask dimensions.

For characterization, the perovskite samples were separately prepared on ITO/glass substrates. Scanning electron microscopy (SEM-XL30 Environmental FEG (FEI)) was used to study morphology. A beam voltage of 10kV with used to analyze all samples. Panalytical X-ray Diffractometer was used to conduct X-ray diffraction (XRD) measurements. For XRD, an anode tension of 40 kV and a filament current of 45 mA was used to produce Cu Kα radiation. UV-Vis Absorption spectra were recorded using a Cary 5000 UV/VIS spectrometer. The lifetimes of minority charge carriers were determined using a Picosecond Time-Correlated Single Photon Counting (TCSPC) Spectrofluorometer. The samples were excited at a wavelength of 425nm for both steady-

state and time-resolved PL measurements. The emission wavelength was monitored at 775 nm. Current-voltage (J-V) measurements for all devices were conducted under AM 1.5G (100mW/cm^2) simulated radiation from a Xenon lamp, which was purchased from Spectra Physics, Oriel Instruments, USA.

5.3 Results and Discussion

Figure 5.1 shows the XRD spectra of different samples prepared with the composition $CH_3NH_3Sr_xPb_{1-x}I_3$ with x varied from 0 to 0.3, with 0 being the control sample. The spectra show high-intensity peaks at 14.0° and 28.3°, which represent the (110) and (220) plane of the perovskite. No new peaks were observed due to the incorporation of Sr, which suggests that the general crystal structure is not altered. However, there is a significant decrease in intensity due to reduced crystallinity with higher-order substitutions of Sr, as shown by the FWHM values as a function of concentration in Fig. 5.2. This loss of crystallinity has been reported previously in Sr doped $FASnI_3$ [155] and $CsPbI_2Br$ [64] perovskite compositions. An increase in FWHM values demonstrates the reduction in grain sizes as well. Fig. 5.3, which shows the SEM images agree with the XRD results.

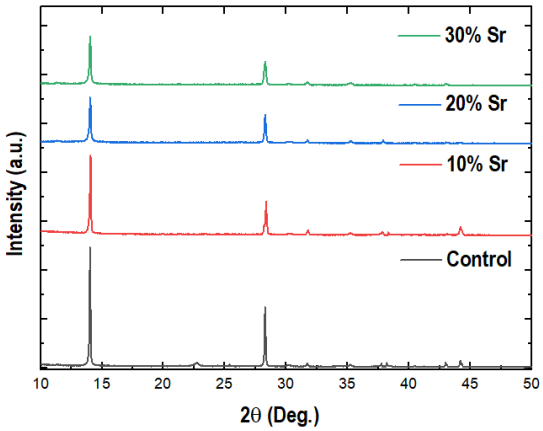

Fig. 5.1 XRD spectra of perovskite with different Sr alloying conditions

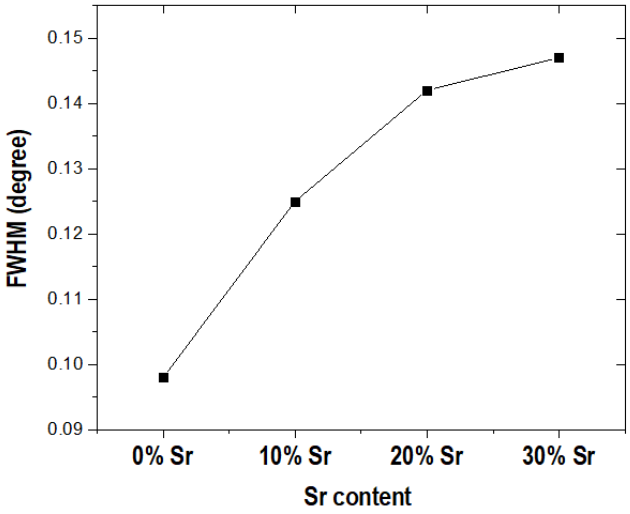

Fig. 5.2 FWHM trend of perovskite with different Sr alloying conditions

The main reaction mechanism can be estimated according to reaction 1 and 2 as follows:

$$x\ Sr(CH_3COO)_2 + (1\text{-}x)\ Pb(CH_3COO)_2 + CH_3NH_3I = CH_3NH_3Sr_xPb_{1-x}I_3 + CH_3NH_3(COO)_2\uparrow \quad (5.1)$$

To be noted is the use of excessive concentration of Pb/Sr acetate precursors, which have a strong influence on the morphology and crystallization kinetics. The use of excess Pb acetate precursors with long spin-coating times and short annealing times has yielded highly crystalline perovskites, as shown in our previous work [104]. It has been reported that Pb with halogens supports highly directional coordination, unlike Sr [156,157]. With increasing % of Sr in the precursor solution, the crystallization is reduced due to the lack of Pb to support the octahedral coordination necessary for perovskites. This most likely results in a change from large grain sizes (*i.e.*, over >1μm) for the control sample to a more compact morphology with few hundred nm for a 20 % Sr alloyed sample. Further increasing the concentration to 30 %, Sr seems to be inducing a thin layer on top of the grains with pinholes.

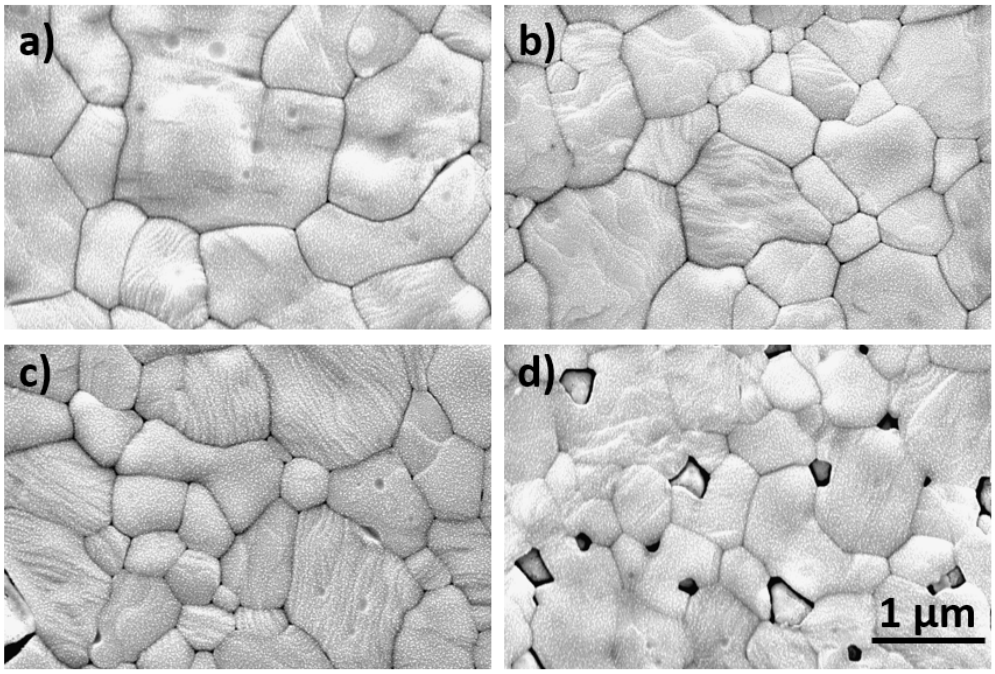

Fig. 5.3.SEM images of a) Control; b) 10 % Sr; c) 20 % Sr; d) 30 % Sr

Sr incorporation into the perovskite was confirmed by comparing the XPS data of the control sample and 10 % Sr alloyed perovskite, as shown in Fig. 5.4. It can be observed that the peaks around 143.5 eV and 138.8 eV, in Fig. 5.4a, which confirms the presence of Pb peaks, and a small peak around 134.5 eV, which confirms the presence of Sr [64]. The Iodine 3*d* peaks occur around 619 eV and 631 eV, as shown in Fig. 5.4b. A significant shift in the binding energy (BE) positions was not observed from the spectra for the Pb peaks. However, a decrease in the intensity of the Pb peaks is evident for the 10 % Sr substituted spectra. The reduction in intensity, coupled with the appearance of the Sr 3*d* peak in this spectrum, confirms its incorporation into the lattice. The Sr 3*d* peak appears to be broad and overlaps around 133.5 eV, which is the BE for $SrCO_3$. Carbon 1*s* peaks are shown in Fig. A1 (see appendix A) shows a broader spectrum for the 10 % alloyed sample (close to 288 eV), which indicates C-O bonding on the surface [65]. Strontium acetate that remained unreacted in the precursor solution would have resulted in partial segregation on the

surface, similar to the report by Perez *et al*. [65]. No shift in Iodine peaks can be observed, but the small reduction in intensity suggests there is a difference in the bonding between the incorporated Sr and I, as shown in Fig. A2. Overall, it appears Sr is successful in replacing the Pb sites.

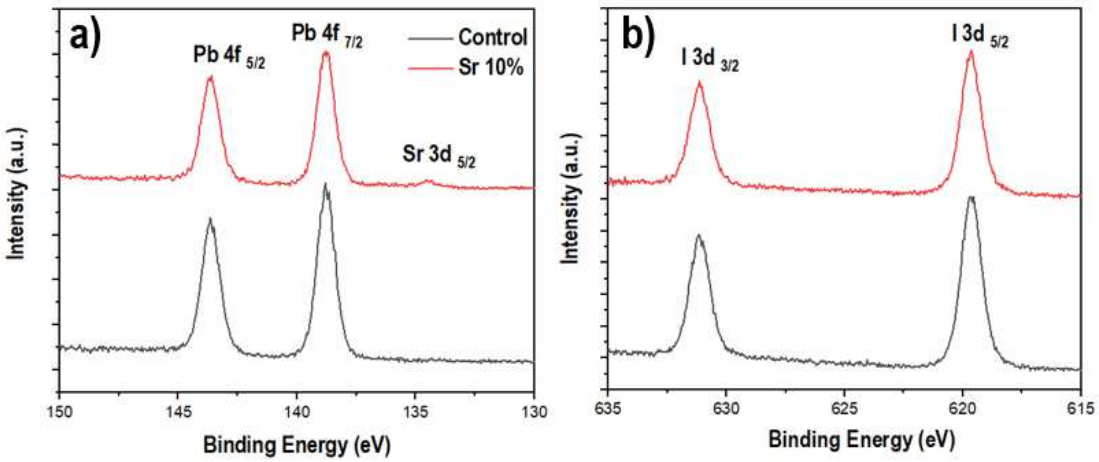

Fig. 5.4 XPS spectra comparison of the perovskite control sample and 10 % Sr alloyed sample – a) Pb peaks, and b) I peaks

The absorbance of the samples was investigated and shown in Fig 5.5. The difference in absorbance is not much for the control sample and 10 % Sr alloyed perovskite. While all the samples show an onset around 760 nm (~1.6 eV), the intensity of absorbance drastically decreases with increasing % of Sr. This could be due to the reduced quality of perovskite with Sr insertion as a similar trend can be observed in XRD. Charge-carrier lifetimes were estimated through Time-resolved Photoluminescence (TRPL) and plotted in Fig 5.6. The corresponding fitting parameters were summarized in Table 5.1. A bi-exponential decay function defined by $I(t) = A_1e_1^{-(t/\tau 1)} + A_2e_2^{-(t/\tau 2)}$ where τ_1 (fast decay component), represents defects from non-radiative recombination while the, τ_2 (slow component), relates to radiative recombination [158,159]. Further, $\tau_{PL} = \alpha_1\tau_1 + \alpha_2\tau_2$, where $\alpha_1 = A_1/(A_1 + A_2)$ and $\alpha_2 = A_2/(A_1 + A_2)$. The total lifetime of charge carriers has improved

with adding Sr into the perovskite. Both τ_1 and τ_2 were found to be higher for increasing Sr %. Note that τ_1 significantly improved from ~ 49 ns to over 97 ns for 10 % Sr introduction. The improvement in lifetime values suggests a strong passivation effect, most likely at the grain boundaries through the formation of carbonate compounds. While increasing lifetime value is observed generally for all Sr alloyed samples, compared to the control sample, beyond 10 %, no significant enhancement is observed. τ_1 is observed to increase from 97.6 ns in 10 % Sr to 101.3 ns in 30 % Sr alloyed samples, which could be due to poor crystallization of the perovskite itself, limiting the lifetime value.

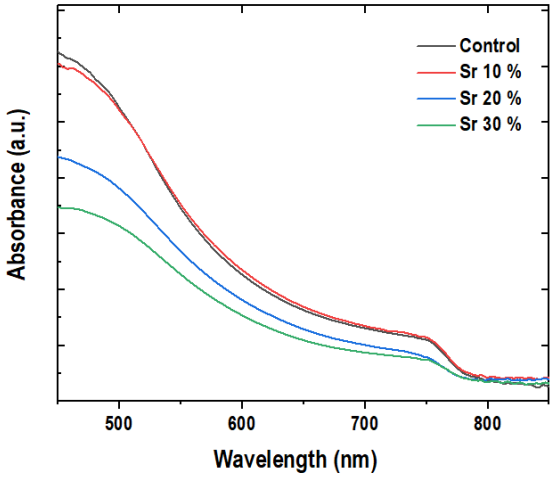

Fig. 5.5 UV-Vis absorbance spectra of perovskite with different Sr alloying conditions

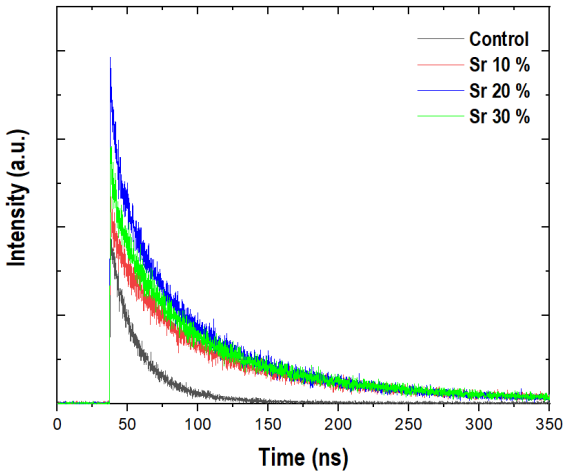

Fig. 5.6 TRPL spectra of perovskite with different Sr alloying conditions

Table 5.1. TRPL fitting parameters of perovskite with different Sr alloying conditions

Sample	τ_1	τ_2	A1	A2	τ_1 %	τ_2 %	Chi2	τ_{PL}
Control	48.7	17.0	28.5	75.2	27.5	72.5	1.06	25.7
10 % Sr	97.6	24.6	131.7	190.2	40.9	59.0	1.25	53.5
20 % Sr	107.5	28.5	59.4	52.1	53.2	46.7	1.07	63.0
30 % Sr	101.3	26.4	105.6	141.9	42.7	57.3	1.18	67.6

Device characteristics with an inverted architecture show a similar trend to the various other properties with reducing the efficiency with increasing Sr content, as shown in Fig 5.7. Current density values are lower with increasing Sr %, which could be down to the poor absorption values. A small increase in V_{OC} is observed with the 10 % Sr device showing 1.01 V compared to 0.93 V from the control sample. The passivation effect induced in the perovskite due to the addition of Sr % would be responsible for the sustained built-in electric fields. This effect is reflected in the efficiency with the 10 % Sr device giving 11.23 % PCE, which is significant for acetate derived perovskite with Sr and Pb. Increasing the amount of Sr decreases the photovoltaic parameters, and subsequently, the device efficiency is affected. Smaller grain sizes and poor absorption of the perovskite are the likely reasons for the poor performance. Also, the thin film layers formed on the surface are known to be highly insulating and could be limiting efficient charge transport and extraction across the interface [65]. Eight devices in each composition were fabricated to demonstrate reproducibility. A similar trend in device properties is observed with decreasing efficiency with increasing % of Sr, as shown in Fig. 5.8. V_{OC} appears to be increased in the 10 % alloyed Sr samples while current density generally decreases, as shown in Figs. A3 and A4, respectively. The fill Factor trend, similar to $V_{OC,}$ is shown in Fig. A5.

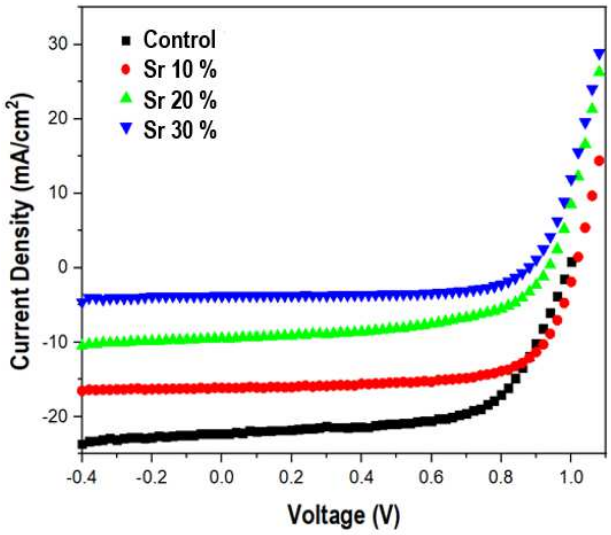

Fig. 5.7 Device characteristics of perovskite with different Sr alloying conditions

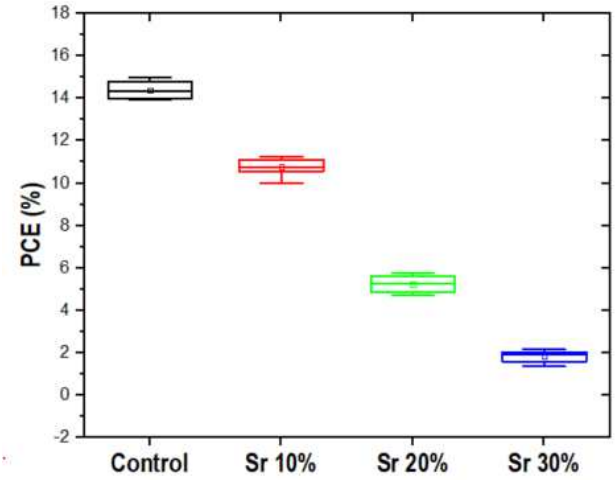

Fig. 5.8 Box plot for efficiency comparison of perovskite with different Sr alloying conditions

Table 5.2. Solar cell device parameters of perovskite with different Sr alloying conditions

Sample	J_{SC} (mA/cm^2)	V_{OC} (V)	FF (%)	PCE (%)
Control	-23.78	0.93	0.64	15.21
10 % Sr	-16.14	1.01	0.68	11.23
20 % Sr	-11.59	0.89	0.65	5.78
30 % Sr	-3.78	0.84	0.63	2.15

The stability of the 10 % Sr alloyed and control perovskite devices was investigated over 75 days of unencapsulated storage in the glovebox. The normalized degradation plot

of PCE is shown in Fig. 5.9, while the other device parameters J_{SC}, V_{OC}, and FF are shown in Figs. A6, A7, and A8, respectively. The J_{SC} degradation trend is almost similar for both devices, which could be attributed to the decomposition of the polymer-based charge transport layers, limiting carrier transport across the interface [160]. The V_{OC} and FF losses, however, were not significant, and the possible reason could be the passivation effect of the Sr carbonate compounds on the perovskite surface. Overall, a PCE decay of only 25% was observed for 10 % Sr based devices, while the control device had a loss of nearly 50%.

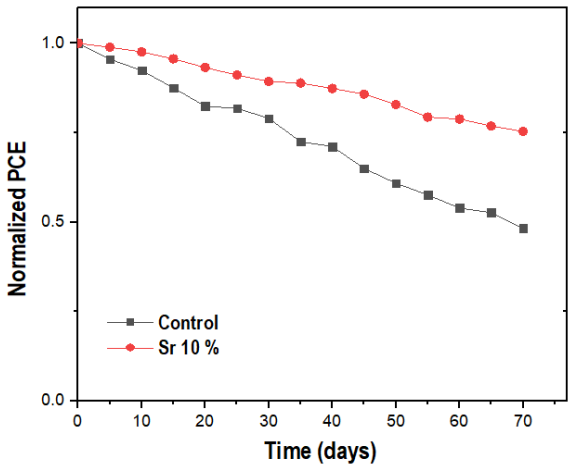

Fig. 5.9 Stability comparison of PCE values of perovskite with different Sr alloying conditions

5.4 Conclusion

In conclusion, higher-order incorporation of Sr into the perovskite is demonstrated using acetate-derived precursors for the first time. The structural, morphological, and optoelectronic properties were studied for samples prepared with different amounts of Sr in the perovskites and compared to the control sample. It was found that with increasing Sr % in the perovskite, the quality of the perovskite is affected, with reduced crystallinity and

absorbance for Sr-based samples. The Sr incorporation resulted in surface enrichment, forming Sr acetate and carbonate compounds, which passivated the surface of the perovskite and increased charge carrier lifetimes. In this regard, the 10 % Sr alloyed device prepared in an inverted device configuration demonstrated 11.23 % PCE with a higher V_{OC} value than the control device. Higher Sr alloyed devices showed poor performance attributed to the poor quality of the perovskite formed. Although the performance of the 10 % Sr device was lower than that of the control device without Sr, stability measurements indicated better retention of PCE for the Sr 10 % based device compared to the control device when tested over 75 days. This study can be extended to other perovskite compositions and highlights the potential for using acetate-derived precursors.

CHAPTER 6

PHENYL ETHYLAMMONIUM IODIDE INTRODUCTION INTO INVERTED TRIPLE-CATION PEROVSKITE SOLAR CELLS FOR IMPROVED VOC AND STABILITY

6.1 Introduction

Organic-Inorganic Hybrid perovskites have emerged recently as excellent materials for light-harvesting and delivered efficiencies beyond 25 % [18]. Versatility in solution processing [161] and unique properties such as small exciton binding energy [37], long charge-carrier diffusion length [38], low trap density [162], and very high absorption coefficient [163] make perovskites a very exciting choice as solar cell materials. Despite the remarkable progress, several hurdles for commercialization, such as moisture- and light-induced degradation, persist [160,164,165]. Overcoming these hurdles was challenging with all-inorganic perovskite solar cells explored thoroughly by several researchers as a means to improve the stability [166,167]. Encapsulation of devices as a method to prevent degradation was also thoroughly investigated [168–170]. Despite the remarkable progress made through these methods for stability against moisture, they still required high-temperature fabrication methods and suffered from degradation due to UV irradiation [171,172].

Further research is necessary for improving the stability of perovskites while demonstrating high efficiencies. Among the current research efforts, two dimensional (2D) Ruddlesden-Popper perovskites have garnered much interest wherein smaller cations such as Methylammonium (MA), Formamidinium (FA), and Cesium (Cs) replaced with much

larger cations [173]. Given their hydrophobic nature and Van der Waals interactions, these cations improved the stability of the perovskites [100]. Despite research on several new cations, some of the most successful and commonly reported perovskites were Guanidinium (GA), Butylammonium (BA), Amino Valeric acid (AVA), and Phenylethylammonium (PEA) [174–177]. The introduction of large cations served to improve overall stability, increased the band-gap, increase excitonic binding energies, and lower charge mobility, all achieved from the proper tuning of the composition through varying the amount of the cations introduced [178–183]. Compositional engineering can bring in certain complications with the retaining of 3D structure necessary for good optical properties to demonstrate high efficiencies[184,185]. For these complications, the majority of the studies involve large cation introductions only in single cation perovskite systems such as $MAPbI_3$ and $FAPbI_3$ [177,181,182,186,187]. Only recently, Wang *et al.* demonstrated more than 17.5% power conversion efficiency (PCE) through the incorporation of n-butylammonium into $FA_{0.83}MA_{0.17}(PbI_yBr_{1-y})_3$ [74]. Through introducing less than 4.5 % PEA, Lee *et al.* demonstrated improved V_{OC} and carrier lifetimes in $(FAPbI_3)_{0.85}(MAPbBr_3)_{0.15}$ compositions [188]. Incorporation of large cations such as GA in triple-cation compositions was only recently investigated by Zhang *et al.,* who achieved 20.29 % PCE [189]. Through precise tuning of GA in the quadruple cation perovskite, they demonstrated that the formation of 2D phases was made possible, with effective passivation of defects leading to high V_{OC}'s and subsequent efficiencies.

Besides the focus on stability, a substantial amount of effort directed towards exploring inverted architectures for low-temperature processing and faster commercialization routes provides scope for flexible solar cells [77,190–193].

Polyethylenedioxythiophene: polystyrene sulfonate (PEDOT: PSS) is widely used due to good optical transparency, mechanical flexibility, high thermal stability, and adequate energy levels. [194–197]. However, the active layer in these inverted architectures uses $MAPbI_3$ and other single and dual cation compositions, with only a few studies on triple-cation perovskite prepared on PEDOT [198] and NiO_x [199,200]. The research involving NiO_X as the HTL involves high-temperature processing; hence, it is not commercially viable for large scale applications. Therefore, further research into doping triple-cation perovskites with large cations and their integration in an inverted configuration with PEDOT HTL is necessary for progress towards commercialization and development of flexible solar cells.

In this work, a quadruple cation composition was demonstrated through the introduction of PEA cation into triple-cation perovskite – $FA_{0.80}MA_{0.15}Cs_{0.5}(PbI_yBr_{1-y})_3$ in different proportions. The ratio of PEA was tuned from 1.67 %, 3 %, and 5 % with respect to FA/MA/Cs cations in the perovskite through solution engineering. More uniform coverage with pinhole-free morphology for low doping of PEA samples in the triple-cation perovskite on a PEDOT surface was observed. An inverted configuration with PEDOT as the HTL, 1.67 % PEA device gives the improved V_{OC} values and an efficiency of 12.77 % compared to 10.16 % for a control device. Further, the stability of the devices investigated for 600 hours of storing in ambient conditions show that all the PEA doped devices fared better compared to the control device. A maximum loss of only 25 % PCE was observed in PEA doped samples compared to nearly 60 % loss of PCE in the control device.

6.2 Experimental Procedure

The chemicals, PEAI, Formamidinium Iodide, FAI, and Methylammonium Bromide, MABr, were purchased from GreatCell Solar. Lead Iodide, PbI_2 (99.99 %), Lead Bromide, $PbBr_2$ (99.99 %), and Cesium Iodide, CsI (99.99 %) were purchased from Sigma Aldrich. All chemicals were used as received. Firstly, stock solutions of 1.5M PbI_2 and $PbBr_2$ were prepared by dissolving the salts in a 4:1 V/V mixture of dimethylformamide (DMF) / dimethyl sulfoxide (DMSO). Both the solutions were then heated to 180 °C for 10 min. CsI solution was prepared to 1.5 M by dissolving in DMSO and heated to 150 °C for 10 min. All solutions were heated to facilitate dissolution until a clear looking solution was obtained. $FAPbI_3$ solution was prepared to a concentration of 1.2 M by dissolving FAI in the PbI_2 solution. Likewise, $MAPbBr_3$ was prepared to 1.2 M by dissolving MABr in the $PbBr_2$ solution. Both these solutions are mixed in the ratio 5:1 ($FAPbI_3$: $MAPbBr_3$) to form FAMA perovskite. A 5 % vol CsI solution was then added to the prepared solution to obtain the FAMACs triple-cation perovskite. Of note is that the solution results in excess Pb precursor. PEA was introduced by first preparing a solution of $PEAPb(I_{0.7}Br_{0.3})_3$ from dissolving 1.2 M PEAI and 1.5 M PbI_2 and $PbBr_2$ in DMF: DMSO (4:1). $PEAPb(I_{0.7}Br_{0.3})_3$ was added in vol % to the perovskite solution in various amounts of 1.67 %, 3 %, and 5 % and designated as P1, P2, and P3, respectively, and the control sample without PEA denoted P0.

Device fabrication was carried out on 2.5 × 2.5 cm^2 patterned indium doped tin oxide on glass substrates (ITO/glass). The substrates were initially cleaned in soap water, followed by ultrasonication in deionized water, acetone, and isopropyl alcohol for 10 mins each. They were then subjected to UV-Ozone treatment for 12 mins to remove organic

contaminants. For the hole transport layer, PEDOT: PSS (Clevios PVP Al 4083) was filtered using 0.45 μm filter and spin-coated at 4000 rpm for 30 s. The substrate was then annealed at 130 °C for 15 min. The perovskite layer was prepared via the one-step method with anhydrous ethyl acetate (EA) as the antisolvent. 120 μL perovskite solution was dropped and spin-coated at 5000 rpm for 35 s. After 10 s from the start, 300 μL of EA was dropped onto the substrate within a span of 3 s followed by an anneal at 100 °C for 1 hour. Phenyl-C_{61}-Butyric-acid methyl ester (PCBM) dissolved in Chlorobenzene (20 mg/ml) was used as the electron transport layer. The PCBM solution was spin-coated at 1000 rpm for 30 s, and the substrates were left to dry for a few mins. For device preparation, 80 nm of Al was thermally evaporated using a shadow mask, and a total area of 0.2 cm^2 was defined.

The as-prepared samples were further characterized to understand various properties and were transferred using a moisture-sensitive apparatus. Scanning electron microscope (SEM-XL30 Environmental FEG) and X-ray diffractometer (Panalytical) were used to study the surface morphology and crystallinity of the samples. For the X-ray diffraction (XRD) measurements, Cu-Kα radiation at a step of 0.01° with a beam current of 45 mA and a voltage of 40 kV was used. Absorbance spectra were recorded using a Cary 5000 UV-Vis spectrometer. Steady-state PL measurements were conducted using a Reinshaw InVia spectroscopy system with an x100 objective lens and 460 nm excitation wavelength. Lifetimes of charge carriers were estimated using a Picosecond Time-Correlated Single Photon Counting (TCSPC) Spectrofluorometer. The decay was monitored at 765 nm, with the samples excited at 460 nm using a white light laser (Fianium) with 6-ps pulses.

The current-voltage measurements (J-V) of the prepared devices were conducted under simulated AM 1.5G (100mW/cm^2) radiation from a Xenon lamp (Spectra Physics, Oriel Instruments, USA). Devices were stored in ambient between measurements with an approximate relative humidity of 30 %.

6.3 Results and Discussion

Figures 6.1a and 6.1b show the schematic of PEA cation incorporation into the perovskite lattice and XRD spectra of the triple-cation perovskite with different doping conditions of PEA, respectively. The samples for XRD shown in Fig. 6.1b prepared on a PEDOT/ITO/glass substrate show typical peaks of the perovskite structure. Characteristic peaks observed at 14.1° and 28.3° correspond to the (110) and (220) planes, respectively. Other peaks of perovskite were indexed at 19.90°, 24.44°, 31.76°, and 35.22° as (012), (003), (123), and (114), respectively. With increasing % of PEA, the intensities of the perovskite peak also increase, implying a distinct improvement in crystallinity. This result is similar to previous studies of PEA and BA incorporation in dual cation systems [175,188]. Full width half maximum (FWHM) values shown in Fig. 6.2a further shows a narrowing of the peak with increasing PEA incorporation, which implies higher crystallinity. To understand if the preferred orientation along (110) and (220) also plays a role in the increased intensity, α is defined to inspect the relative intensity of (110) and (220) with respect to other peaks from randomly oriented grains as follows.

$$\alpha = \frac{\sum I(110)+(220)}{\sum hkl} \times 100\ \% \qquad (6.1)$$

The corresponding values of α in % plotted in Fig. B1 (see appendix B), show that a preferred orientation is also introduced with the relative intensity values of (110) and

(220) increasing with PEA doping and saturates at higher concentration. The FWHM and α values for all samples are summarized in Table. B1. Hence, these results prove that PEA doping in small amounts (P1, P2, and P3) promotes crystallization and preferred orientation in triple-cation systems.

A more detailed understanding of the nature of PEA doping was obtained by analyzing normalized peak position data, as shown in Fig. 6.2b. A shift in the peak maximum was observed with increasing doping levels of PEA. The shift is likely due to the reduced lattice constant due to compressive strain from the introduction of large cations as observed by Wang *et al.* [175] when BA was introduced to replace FA/Cs in their work. Note that the precisely tuning the dopant ratio of PEA to I^-/Br^- has to be the same as that of FA/MA/Cs for direct substitution. The increase in the PbI_2 intensity at 12.1° is attributed to PbI_2 and $PbBr_2$ introduction along with PEA in the same stoichiometry as the triple-cation perovskite composition. The film formation and morphology is generally not straightforward when a large cation such as PEA is introduced into mixed cation systems [181,188], and this is further discussed in the next section. Fig. B2 shows the XRD spectra of samples prepared on ITO/glass to see if the effect of adding PEA cation is also reproduced on the ITO substrate. The intensity of perovskite and PbI_2 still increases with PEA doping, although the intensities are lower than those prepared on PEDOT. These above results further confirm the universal nature of PEA doping in the crystallization of FAMACs perovskite.

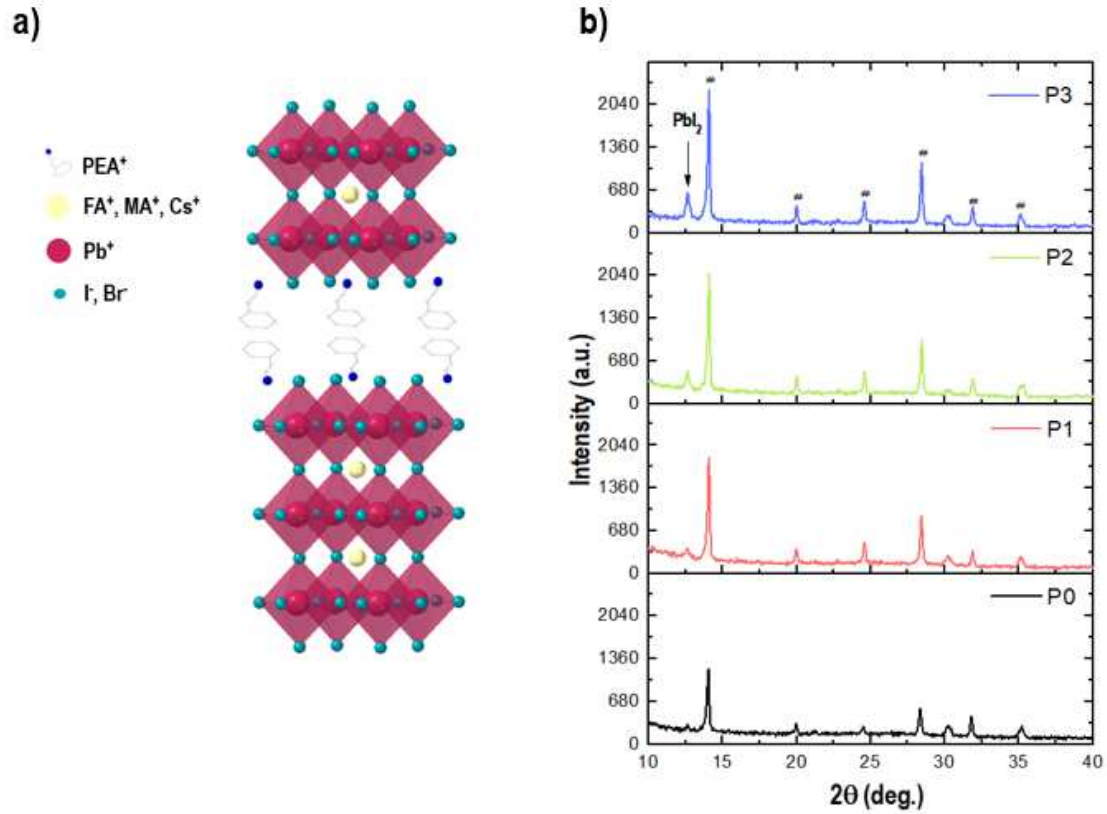

Figs. 6.1 a) Schematic of PEA doping into triple-cation perovskite
b) XRD spectra of perovskite with different PEA doping conditions prepared on a PEDOT/ITO/glass substrate (# represents perovskite)

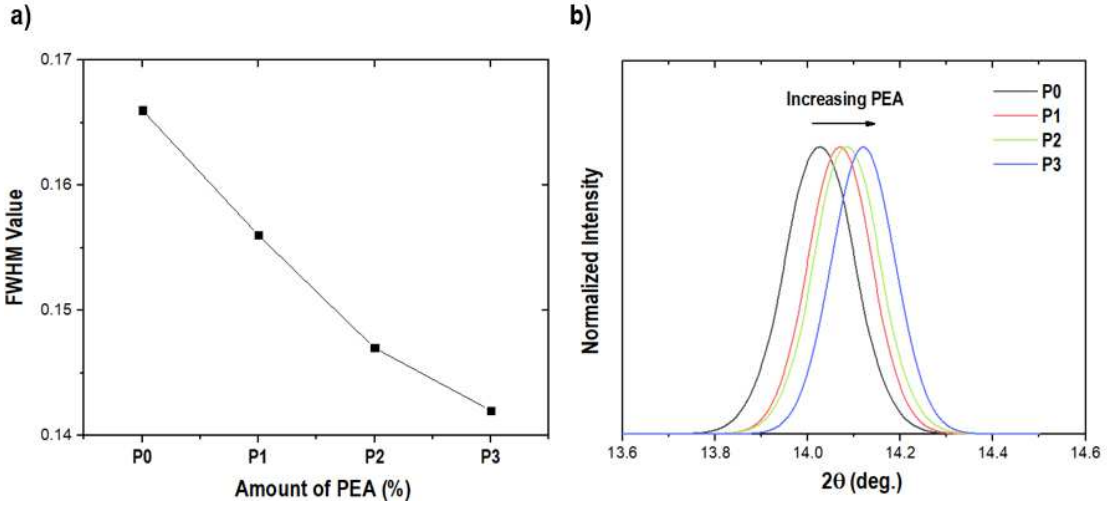

Fig. 6.2 a) FWHM values plotted for perovskite and PEA doped samples
b) Normalized intensity of peak maxima for perovskite and PEA doped samples

Figure 6.3 shows the SEM images of the triple-cation perovskite on PEDOT/ITO/glass with different PEA doping levels. The introduction of large cations

creates a layered morphology with plate-like structures as the amount increases, according to previous reports [181,201]. In our case, the control sample, which is the triple-cation perovskite, appears mostly uniform with few pinholes. The introduction of 1.67 % PEA (P1) seems to make the film very uniform and dense with slightly larger grain sizes and almost no pinholes. The sample P2 (3 % PEA) shows a slightly disparate grain size distribution and aggregates deposited, which is likely due to an increased rate of crystallization [175]. Further increasing the amount to 5 % PEA (P3) introduces the aggregates, with platelets like structures interspersed with small grains and a large number of pinholes. The nature of PEA was suggested as quasi-2D when introduced into dual cation perovskites [188] and that 2D/3D phases coexist when PEA is introduced as $PEAPbI_3$. It is suspected that the formation of $PEAPb(I_{0.7}Br_{0.3})_3$ results in mixed 2D/3D phases, with the quasi-2D amount increasing in the case of P3. Further, samples prepared on ITO/glass also show similar phenomena, as observed in Fig. B3. The grain size and morphology improve for P1 (1.67 % PEA), while aggregates and pinholes start appearing in P2 (3 % PEA). Platelet-like structures distributed between grains occur for P3 (5 % PEA). A uniform morphology is a key to smooth charge transport across the perovskite/charge transport layer interface, and the optoelectronic properties will be discussed in the next sections.

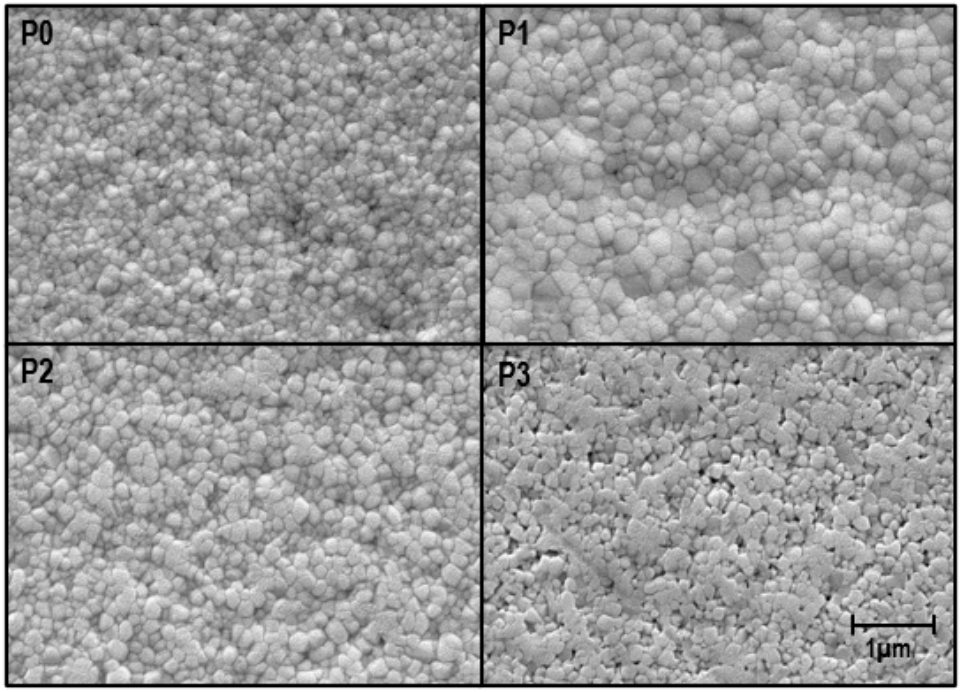

Fig. 6.3 SEM images of perovskite with different amounts of PEA doping conditions prepared on PEDOT/ITO/glass

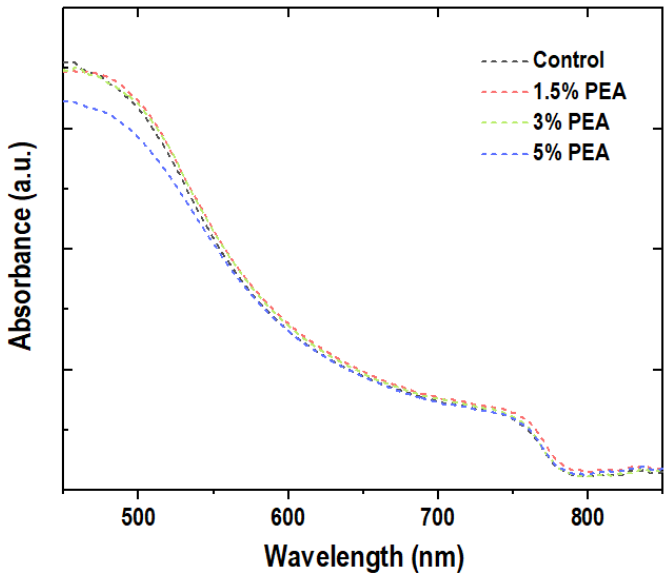

Fig. 6.4 UV-Vis spectra of perovskite with different PEA doping conditions

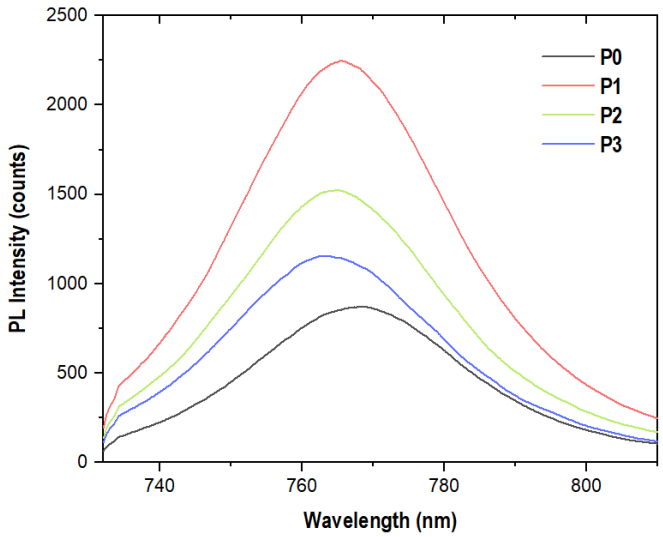

Fig. 6.5 Steady-State PL spectra of perovskite with different PEA doping conditions

The optical properties are investigated for the perovskite with different PEA doping, prepared on ITO/glass. Fig. 6.4 shows the UV-Vis absorption spectra of the samples with no noticeable change in the band edge observed for higher PEA doping. Only the P3 (5 % PEA) sample shows slightly weaker absorption around 450 nm – 550 nm. Higher amounts of $PEAPb(I_{0.7}Br_{0.3})_3$ results in loss of the 3D nature of perovskites and could be a reason for the low absorption in this range. Fig. 6.5 shows steady-state PL spectra with all the samples illuminated from the front (perovskite) side. The intensity increases with higher PEA doping (P1 and P2) compared to the control sample without any PEA and then decreases for P3. This increase in PL intensity is consistent with the reports from Lee *et al.* [188], where they observed increased intensity of the PL when incorporating PEA into double cation perovskite. The decrease in intensity for P3 is likely due to the increased amount of 2D $PEAPb(I_{0.7}Br_{0.3})_3$, resulting in aggregates or deposition at the grain boundaries, along with loss of 3D nature of perovskite could be the result of poor absorption and luminescence. This phenomenon of mixed 2D/3D could also explain

the observed blueshift in the normalized PL intensity, as shown in Fig. B4, where the 2D perovskite presence introduces large potential barriers with charge carriers difficult to escape [177]. The effect was found to be apparent in P3, which is only 5 % PEA doping and hence is the likely threshold in our case of triple-cation perovskite.

The lifetimes of charge carriers are shown in Fig. 6.6, which is the time-resolved spectra of perovskite with different PEA doping prepared on ITO/glass. All the samples were illuminated from the front side, and the spectra are fitted with a bi-exponential decay function based on the equation $I(t) = A_1e_1^{-(t/\tau 1)} + A_2e_2^{-(t/\tau 2)}$ with the corresponding decay parameters shown in Table B2. The fast decay component (τ_1), which is associated with charge carrier trapping induced through trap states, gives information on the structural disorder and defects formed during crystallization. The slow decay component (τ_2) is related to free carrier radiative recombination [158,202,203]. τ_1 increased from 58.27 ns for the control to 83.60 ns and 65.23 ns for P1 and P2, respectively, while the proportion of this component decreased from 40.31 % to 25.26 % and 30.64%. τ_2, on the other hand, improved from 144.07 ns to 196.37 ns and 157.34 ns for P1 and P2, respectively. This is the result of improved crystallinity of the triple-cation perovskite from the addition of PEA, as previously reported [177,188]. Increasing the amount of PEA to 5 % (P3) induces the quasi 2D phase, which further improved the lifetime to 393.80 ns due to the suppressed carrier recombination and low defect density. Also, the presence of higher amounts of 2D perovskite allows confining the carriers for longer periods before recombination.

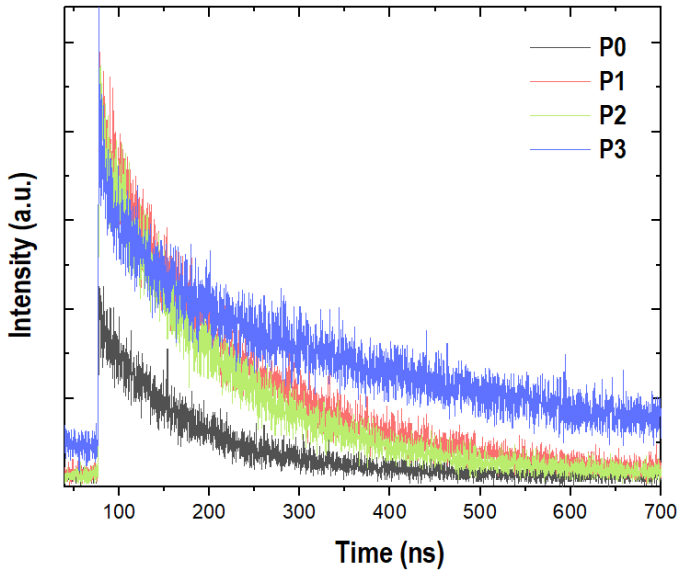

Fig. 6.6 TRPL spectra of perovskite with different PEA doping conditions

The current density characteristics are shown in Fig. 6.7 with the corresponding device parameters listed in Table 6.1. The devices were fabricated in an inverted configuration with PEDOT and PCBM as the respective HTL and ETL, as shown in the inset of Fig. 6.7. For all the devices with PEAI, improved V_{OC} was observed compared to the control sample, which only demonstrated 0.72 V. The V_{OC} improved with increasing amounts of PEA incorporated into the perovskite with 0.80 V for P1 (1.67 % PEA) and 0.85 V for P3 (5 % PEA). Notably, the current density decreased for the 5 % PEA device due to the formation of the 2D $PEAPb(I_{0.7}Br_{0.3})_3$ on the surface, which can inhibit charge transport, given its insulating nature [188]. Overall, the efficiency improved to 12.77 % for the P1 (1.67 % PEA) device and 11.57 % for the P2 (3% PEA) device compared to 10.16 % for the control device. The efficiency values were considerably lower when compared to conventional triple-cation perovskite devices values [72]. Note that the inverted configuration was prepared with PEDOT and PCBM as the HTL and ETL, respectively.

Few reports have demonstrated high efficiency for devices in the inverted configuration with the triple-cation perovskite as the active layer [198] due to the formation of several defects and small grains. PEA doping in small levels improved the morphology and size of the triple-cation perovskite on PEDOT, and hence better device parameters and efficiency were observed. Further, ten devices in each variation were prepared and tested for investigating reproducibility in device performance. Box plots of the PCE and V_{OC} are shown in Figs. 6.8a and 6.8b, respectively. The corresponding J_{SC} and FF box plots are shown in Fig. B5 and B6, respectively. These plots further validate the improved V_{OC} with increasing PEAI concentration and demonstrate good reproducibility. A decrease in J_{SC} and FF for 5 % PEAI introduction explains the lower PCE.

Table 6.1 Solar cell device parameters of perovskite with different PEA doping

Sample	PCE (%)	V_{OC} (V)	J_{SC} (mA/cm^2)	FF (%)
P0	10.16	0.72	22.21	61
P1	12.77	0.80	22.44	68
P2	11.57	0.82	21.90	63
P3	7.27	0.85	13.60	55

The stability of the devices was evaluated over a period of 600 hours while stored in ambient, and the corresponding decay in the efficiency is shown in Fig. 6.9. All the devices with PEA incorporated in the perovskite demonstrate superior stability, which is primarily attributed to the 2D phase formation resulting in improved moisture stability. The control device efficiency decayed much faster relative to the PEA devices. Figs B7, B8, and B9 show the decay regarding other device parameters, J_{SC}, V_{OC}, and FF, respectively.

The higher V_{OC} is retained for the PEA devices with P3 showing a high value after several hours. This result can be explained on the basis of a higher amount of mixed 2D/3D phases present, which stabilized the V_{OC}. The decrease in J_{SC} (Fig. B7) and FF (Fig. B9) follow a similar trend to the control device due to the decomposition of the perovskite, as observed in several reports [204,205].

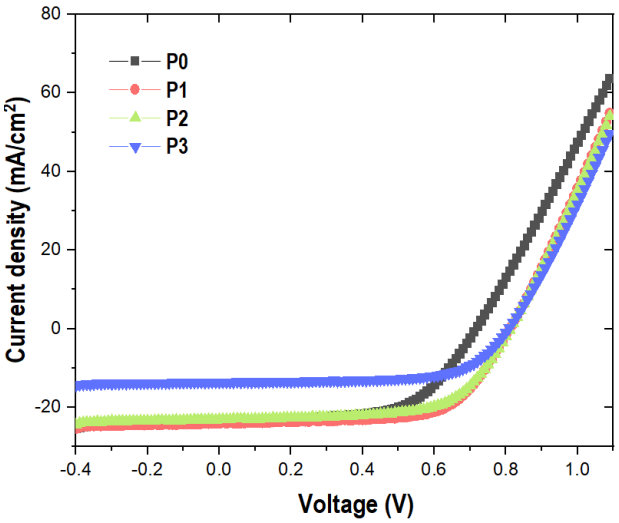

Fig. 6.7 Current-voltage characteristics of perovskite device with different PEA doping conditions

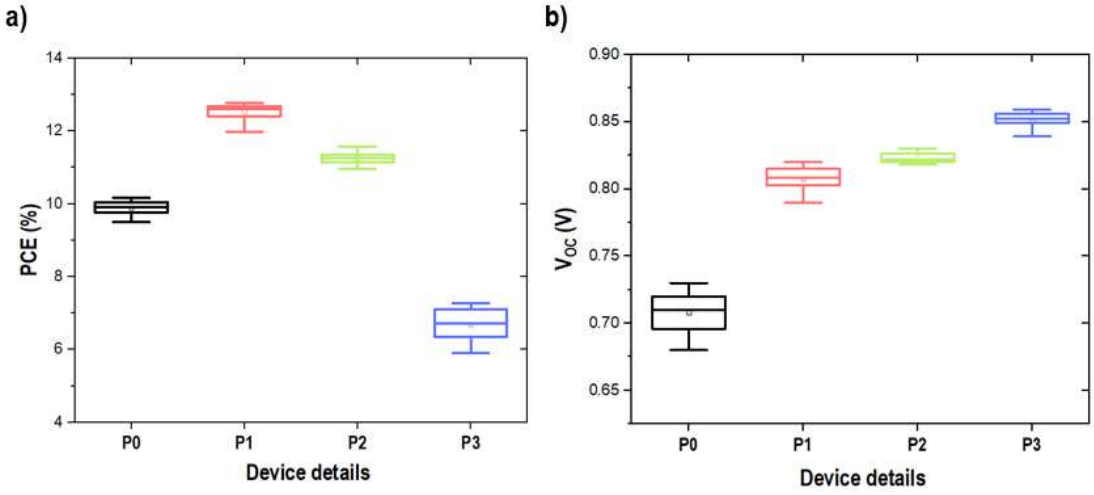

Fig. 6.8 Box plots of a) PCE and b) V_{OC} of perovskite device with different PEA doping conditions

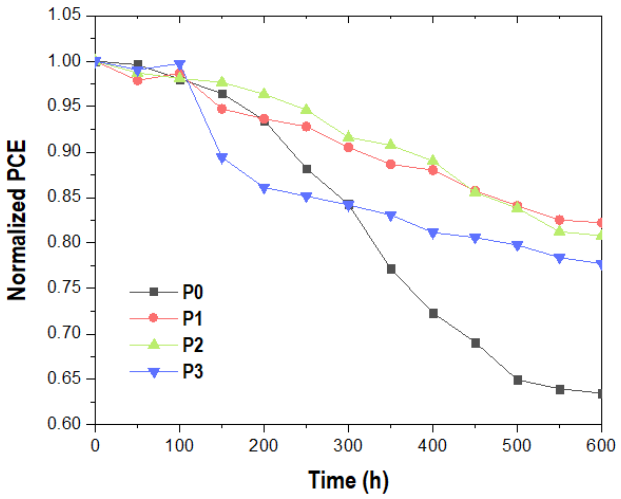

Fig. 6.9 Degradation of PCE of perovskite devices with different PEA doping conditions

6.4 Conclusion

To summarize, this work demonstrates the effect of introducing PEA cations into a triple-cation perovskite with a composition of $PEA_x(FA_{0.85}MA_{0.10}Cs_{0.05})_{1-x}$ with x varying from 0 – 5 %. Adding PEA improves the overall crystallinity of the perovskite, with fewer pinholes and better coverage for samples prepared on both PEDOT and ITO surfaces. Higher amounts of PEA, such as 5 %, results in the formation of 2D $PEAPb(I_{0.7}Br_{0.3})_3$ platelet-like structures on the surface. The improved crystallinity of the perovskites, from adding PEA, also results in higher PL intensity and lifetimes due to reduced surface recombination and fewer defects. Subsequently, the performance of the device in an inverted configuration is superior for 1.67 % and 3 % PEA doped devices compared to the control device. Higher-order doping (5 % PEA) shows poor conductivity, given the high impedance of the 2D phase to charge transport across the interface between the active layer and the charge transport layers. Low conductivity, coupled with a loss of 3D nature of perovskite in the 5 % PEA doped sample, results in poor optical properties and PCE. The

overall stability of the PEA-doped devices improves due to the enhanced moisture resistance built-in by the introduction of PEA. This work shows the effect of the addition of PEA in multi-cation systems, especially triple-cation perovskite, and provide a better understanding of crystallization on a polymer surface, with scope for further extending the work to flexible solar cells.

CHAPTER 7

PASSIVATION OF TRIPLE-CATION PEROVSKITES USING GUANIDINIUM IODIDE IN INVERTED SOLAR CELLS FOR IMPROVED OPEN-CIRCUIT VOLTAGE AND

7.1 Introduction

Organic-Inorganic hybrid perovskite solar cells (PSCs) have attracted a lot of attention since they first came out in 2009 [83]. Owing to some unique properties such as strong absorption [206], tunable bandgap [207], excellent charge carrier mobility, and long diffusion lengths [174], small exciton binding energies [208], PSCs oversaw significant development. A high record of 25.2% power conversion efficiency (PCE) was reported to date [209], which is comparable to what is achieved by most conventional solar industry technologies. Further increase in the efficiencies can be expected through improvements in open-circuit voltages (V_{OC}) and fill-factor (FF) since the short-circuit density (J_{SC}) has almost reached its limit with a recent record of ~28mA/cm^2 reported [210].

The V_{OC} of the devices is regarded as a strong function of defects in the bulk or on the surface of the perovskite [211–214]. Perovskite materials are considered highly polycrystalline and have a structural disorder associated with grain boundary and crystallographic defects [215]. The commonly reported composition – $CH_3NH_3PbI_3$ is known to have shallow defects on the surface, which could be potential recombination centers and contribute to voltage losses [203,216]. A multi cation system with dual [217] and triple-cations [218] in place of Methylammonium (MA) would also lead to several defects on the surface due to the competing nature of crystallization. Also, the solution processing methodology, a commonly used fabrication route in research on PSCs, is known

to induce several defects on the surface [219,220]. For any given composition, the solution route gives rise to dangling bonds on the surface, which need to be passivated. Several groups have addressed this through the introduction of halide compounds such as diammonium iodide [221], quaternary ammonium halides [219], potassium halide [222], and iodopentafluorobenzene [223]. Other methods of passivation include deliberately inducing the PbI_2 phase into the perovskite to for a type – I band alignment and suppress charge carrier recombination [106,107]. Grain boundary passivation through excess Pb in the precursors was investigated by several groups as a means to promote stability and efficiency [104,152,224–227]. The introduction of large cation groups such as phenyl ethyl ammonium iodide (PEAI) [217] into the perovskite resulted in excellent improvements to the efficiency and stability of the device through passivation mechanisms. However, fewer reports investigated the effect of introducing large cations into triple-cation perovskite compositions – $Cs_{0.05}(FA_{0.83}MA_{0.17})Pb(I_{0.83}Br_{0.17})$ [189] and double cation compositions – $(FAPbI_3)_{0.85}(CH_3NH_3PbI_3)_{0.15}$ [188] and $FA_{0.8}Cs_{0.2}PbI_{2.7}Br_{0.3}$ [228]. While these studies have shown improved performances and stabilities of single and dual cation perovskites, further investigation is needed for post-treatment procedures of triple-cation perovskite compositions along with improvements in the solution processing and passivation.

A planar-inverted architecture is known to have lower processing temperature and simpler fabrication routes, making them faster to commercialization than mesoporous architecture [42,78,192], especially for flexible solar cells. Of the various hole transport layer (HTL) materials used in an inverted configuration, Polyethylenedioxythiophene: poly(styrene sulfonate) (PEDOT: PSS) has been widely used due to good processability, high mechanical flexibility, good thermal stability, adequate transparency, and energy

levels [190,195,229–234] and also extend their applicability to inverted device architectures. Crystallization of perovskites on a PEDOT surface is quite different from that of other materials with Reza *et al.,* demonstrating that post-treated PEDOT improved the contact angle and hence grain sizes of $MAPbI_3$ [235]. Triple-cation perovskite in an inverted configuration with PEDOT and phenyl-C61-butyric acid methyl ester as the electron transport layer (ETL) has been explored by Ji *et al.,* primarily to prevent degradation of Sn-based perovskites by salt doped HTL such as Spiro-OMeTAD [198]. In this regard, there is a need to explore the crystallization and morphology of triple and dual cation perovskites on a PEDOT surface. Research on triple-cation perovskites in an inverted configuration is also necessary to facilitate simpler processing and fast commercialization, especially for future flexible solar cells.

In this work, the effect of post-treatment of triple-cation perovskites with Guanidinium Iodide (GUAI) is explored. The structural and optical properties of adding different concentrations of GUAI on triple-cation perovskite prepared on a PEDOT surface were studied. Further, the device performances in an inverted configuration with PEDOT: PSS and PCBM as the HTL and ETL, respectively, were investigated. The post-treatment with GUAI yields better morphology and demonstrate improved V_{OC}'s from 0.73V for a control sample to 0.86V for GUAI loaded sample and a subsequent power conversion efficiency (PCE) of 13.01%. A passivation effect that plays in suppressing recombination and the reason behind the improved V_{OC} is proposed

7.2 Experimental Procedure

GUAI (99.99%), Methylammonium Bromide, MABr (99.99%), Formamidinium Iodide, FAI (99.99%) were purchased from GreatCell Solar. Lead Iodide, PbI_2 (99%), Lead

Bromide, $PbBr_2$ (99.99%), and Cesium Iodide (CsI) were purchased from TCI America. All the chemicals were used as received without any further processing. PbI_2 and $PbBr_2$ were prepared to 1.5M as a stock solution in a 4:1 V/V mixture of dimethylformamide (DMF) and dimethylsulfoxide (DMSO). The solutions were heated to 180°C for 10mins to facilitate dissolution. Both these solutions were used within a week of preparation. CsI solution was prepared to 1.5M in DMSO and heated to 150°C for 10 mins and cooled to room temperature before use. FAI and MABr were dissolved in PbI_2 and $PbBr_2$ solutions, respectively, to a concentration of 1.2M to prepare $FAPbI_3$ and $MAPbBr_3$. These were mixed in the ratio 5:1 of $FAPbI_3$ and $MAPbBr_3$ to form the FAMA precursor solution. CsI (5% vol) was then added to the FAMA perovskite to obtain the FAMACs triple-cation perovskite. GUAI was dissolved to different concentrations of 1mg/ml, 2mg/ml, and 3mg/ml in isopropyl alcohol (IPA) with stirring for a few mins. PEDOT: PSS (purchased from Xi'an polymer light corporation) filtered through a 0.45µm filter was used as the hole transport layer. Phenyl-C_{61}-Butyric-acid methyl ester (PCBM) (purchased from Sigma Aldrich) was dissolved in Chlorobenzene (20mg/ml) for use as the electron transport layer. For the device fabrication, a 2.5x2.5 cm^2 patterned indium doped tin oxide on glass (ITO/glass) was used as the substrate. These substrates were thoroughly cleaned in soap water, followed by ultrasonication in deionized water, acetone, and IPA for 10mins each. They were further treated to UV-Ozone for 12mins to remove organic contaminants. Substrates were then transferred to a Nitrogen filled glovebox for device fabrication. PEDOT: PSS was spin-coated for 30s at 4000rpm, followed by annealing at 130°C. This was followed by the deposition of the perovskite with anhydrous ethyl acetate, EA (Sigma) as the antisolvent through a one-step method. 120µL of perovskite was dropped on the

substrate and spin-coated at 5000rpm for 35s. 10s from the start, 300µL of EA was dropped within 3s, resulting in dark brown color. Substrates were then annealed at 100°C for 1 hour. Different GUAI solutions were then spin-coated at 4000rpm for 30s to give G1, G2, and G3 for 1mg/ml, 2mg/ml, and 3mg/ml, respectively, with G0 assigned as the control sample. This was followed by spin coating PCBM at 1000rpm for 30s with no post-annealing. Finally, 80nm of Al was deposited by thermal evaporation using a shadow mask. The final device area was measured to be $0.2cm^2$.

The prepared samples were characterized using different techniques to further understand various properties. X-ray diffraction was performed using a diffractometer with Cu-Kα radiation with a corresponding beam current of 45mA and anode tension of 45kV. A Scanning electron microscope (SEM XL-30 Environmental FEG) was used to study the morphology and film formation. Absorbance spectra were recorded using Cary 5000 UV-Vis spectrometer. Steady-state photoluminescence (PL) measurements were carried out on the perovskite samples using a Reinshaw InVia spectroscopy with an x100 objective lens and 460nm excitation wavelength. The samples were excited from the front side for all PL measurements. The lifetime of minority carriers was estimated using a Picosecond Time-Correlated Single Photon Counting (TCSPC) Spectrofluorometer. Decay was monitored at 765nm when the samples were excited at 460nm using a white light laser (Fianium) with 6-ps pulses. Current-voltage measurements (J-V) of the devices were carried under simulated AM 1.5G ($100mW/cm^2$) radiation using a Xenon lamp (Spectra-Physics, Oriel Instruments, USA).

7.2 Results and Discussion

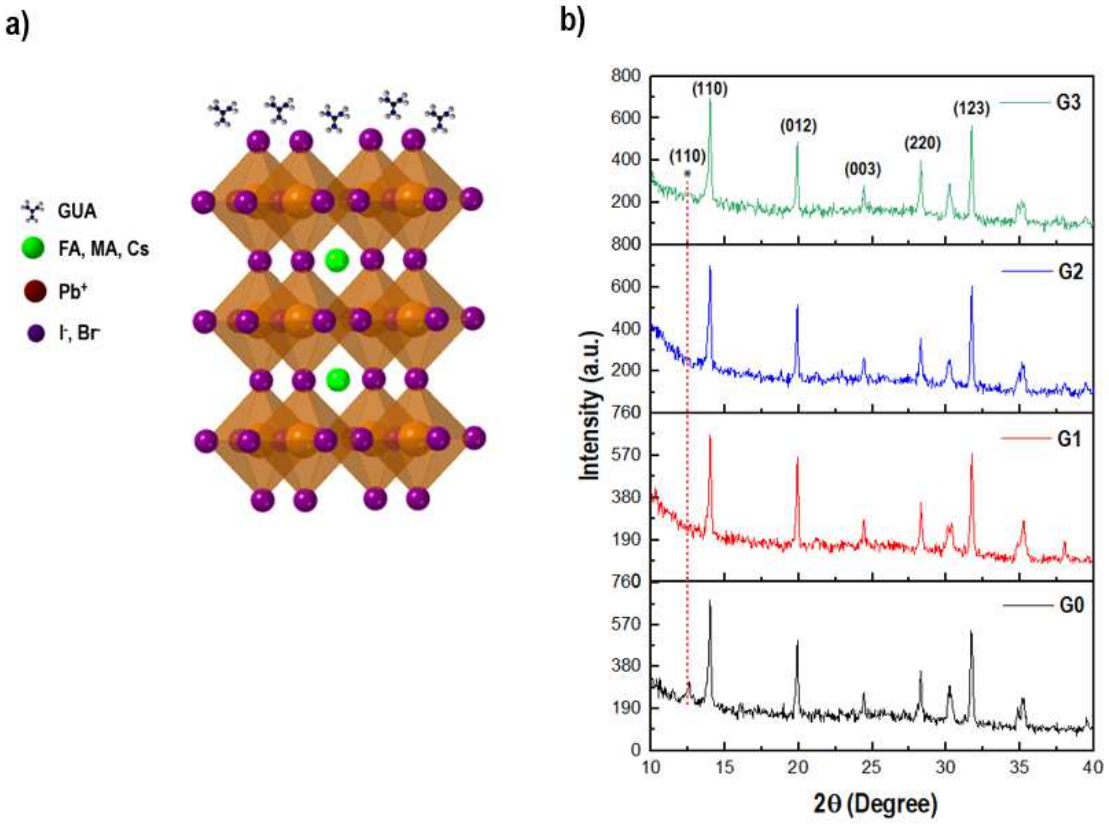

Fig. 7.1 a) Schematic of GUAI passivation in triple-cation perovskite, and b) XRD spectra of perovskite with different GUAI loading conditions prepared on PEDOT/ITO/glass (* represents PbI_2)

Figure 7.1a shows the schematic of the passivation effect of adding GUAI on triple-cation perovskite. Fig. 7.1b shows the XRD spectra of the triple-cation perovskite with the theoretical composition $FA_{0.85}MA_{0.10}Cs_{0.05}Pb(I_{0.7}Br_{0.3})_3$, with different loading conditions of GUAI, prepared on a PEDOT/ITO/glass substrate. The observed peaks at 14.10°, 19.8°, 24.4°, 28.1°, 31.5°, and 34.6° correspond to (110), (012), (003), (220), (123), and (114) planes, respectively of the triple-cation perovskite [72,236]. The peak at 12.67° (also indicated by the dashed red line) corresponds to PbI_2 [237]. PEAI as a surface modifier

was investigated by a lot of groups, and additional diffraction peaks were not observed compared to control samples [217,228]. The spectra from Fig. 7.1b also indicates a similar trend with GUAI potentially residing in the grain boundaries and on the surface. No additional 2D phases were noticeable from the XRD spectra, while the intensity of the perovskite was found to be similar across all the samples. The intensity of the PbI_2 peak around 12.6° gradually decreases with increasing GUAI loading. This effect indicates that the GUAI is reacting with the PbI_2 to partially form $GUAPbI_3$, which was known to be 1D in nature [238]. Although, there are no discernible peaks indicating the presence of $GUAPbI_3$, possibly due to a very weak signal from this phase. In the work of Jodlowski *et al.* [238], a peak of $GUAPbI_3$ was only possible at very high concentrations of GUA in the perovskite solution. The choice of triple-cation perovskite in our case could have led to unreacted PbI_2 forming on the surface, which explains the origin of the peak at 12.6° in the control sample. Also, given the large size of GUA cation, the incorporation into the perovskite itself is impeded [238]. To further validate the reproducibility of the morphology, the XRD spectra of triple-cation perovskite on ITO/glass is shown in Fig. C1 (see appendix C). The general intensity of the perovskite prepared on ITO decreased a little compared to that of PEDOT/ITO/glass, and a similar trend was observed with the PbI_2 peak at 12.6° decreases with increasing GUAI loading. The surface modification of adding GUAI will be further explored in the next section.

SEM images of the triple-cation perovskite with different loading conditions of GUAI, prepared on PEDOT/ITO/glass, are shown in Fig. 7.2. All the samples which have the triple-cation composition exhibit a uniform morphology with little to no pin-holes and similar grain sizes. The surface appears to be modified for GUAI based samples compared

to the control sample. Several bright spots (indicated by yellow circles) that appear in the control sample, which are most likely unreacted PbI_2 crystals, have been minimized with increasing GUAI loading. Further, a more compact morphology with smoother surfaces and almost no bright spots was observed for G3, which is the highest concentration. A passivation effect is likely induced due to GUAI depositing at grain boundaries and further reacting with PbI_2, as evidenced in the XRD spectra. However, unlike the passivation induced by adding GUA in the precursor through the formation of δD $FAPbI_3$ and 2D $FAGAPbI_4$ [189], in this case, it is from post-treatment of the perovskite with GUAI. Higher concentrations of GUAI would yield thicker layers on top of the perovskite, thereby increasing passivation, although this effect is not apparent in the morphology images. Charge transport across the passivated perovskite layers would be significant and will be discussed in the next sections. The SEM was also carried on samples prepared on an ITO/glass surface and shown in Fig. C2. The triple-cation perovskite crystallizes as a large number of grains on the PEDOT with slightly smaller sizes than on PEDOT/ITO/glass, as also evidenced by the XRD spectra. Nonetheless, this also leads to the appearance of bright spots that were found to be minimized and disappear with increasing GUAI concentration in post-treatment. A smoother morphology that is pin-hole free and homogenous across the surface was realized post GUAI treatment. The formation of this kind of morphology is important in forming a good interface with PCBM, to minimize shunt pathways and losses during operation.

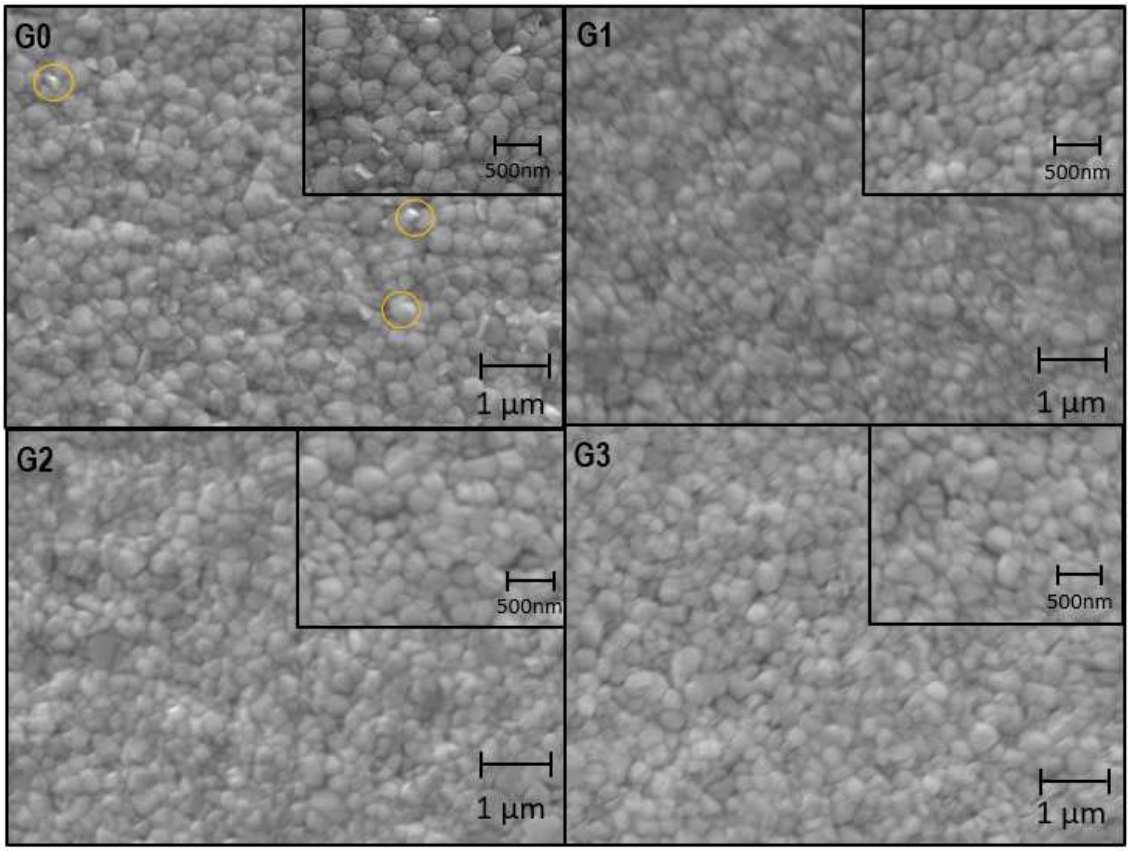

Fig. 7.2 SEM images of perovskite with different GUAI loading conditions prepared on a PEDOT/ITO/glass

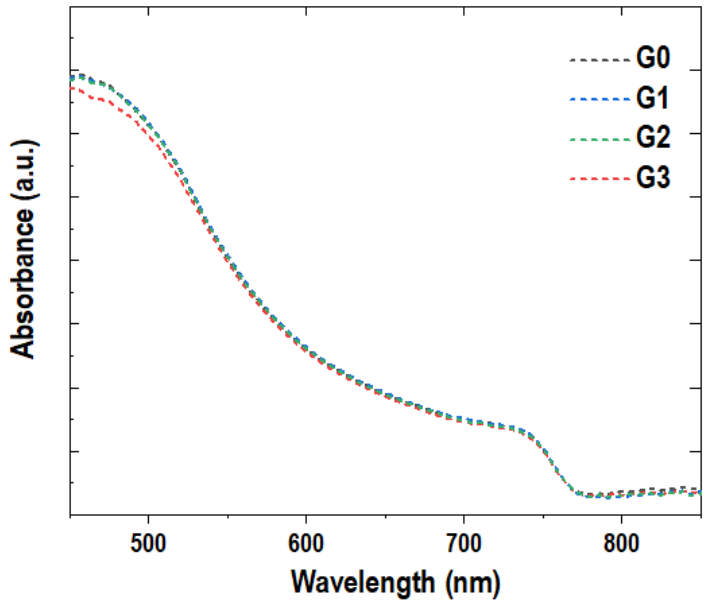

Fig. 7.3 UV-Vis spectra of perovskite with different GUA loading conditions

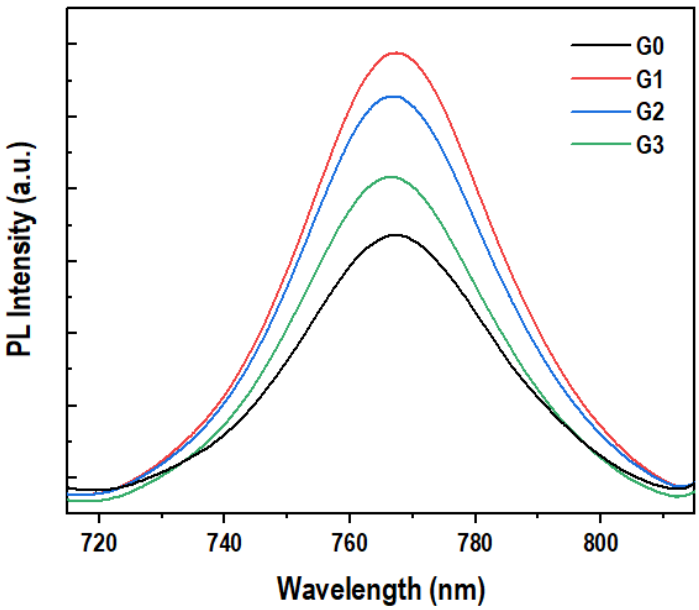

Fig. 7.4 Steady-state PL spectra of perovskite with different GUA loading conditions

The optical properties can be explained by the UV-Vis absorption and Steady-state photoluminescence (PL) results in Figs. 7.3 and 7.4, respectively. A small reduction in absorbance is observed for the G3 sample, which has a higher concentration of GUAI

(3mg/ml). Other than this, the absorbance is similar for all the samples relative to the control sample without GUAI. The steady-state PL spectra indicate that the PL intensity improves for all loading conditions of GUA, which is a sign of suppressed non-radiative recombination [239]. The suppressed recombination due to a surface treatment using a large cation salt is similar to the results observed by Jiang *et al.* [217]. Higher loading of GUA, however, does not seem beneficial with the PL intensity dropping for G3 (3mg/ml). Although additional peaks of a specific 2D phase are not observed in XRD results, it is likely that the higher concentration induces a weak form of $GUAPbI_3$ present on the surface, which could also be playing a role in the suppressing non-radiative recombination.

Time-resolved PL studies were carried out on the samples with different GUA loading, and the corresponding spectra are shown in Fig. 7.5. A bi-exponential decay function defined by $I(t) = A_1e_1^{-(t/\tau 1)} + A_2e_2^{-(t/\tau 2)}$ was used to fit the parameters and shown in Table 7.1. The fast decay component, τ_1, represents defects from non-radiative recombination while the slow component, τ_2, relates to radiative recombination [158,159,202]. τ_{PL} which can be defined as the average lifetime, was determined by the equation, $\tau_{PL} = \alpha_1\tau_1 + \alpha_2\tau_2$, where $\alpha_1 = A_1/(A_1 + A_2)$ and $\alpha_2 = A_2/(A_1 + A_2)$. The average lifetime, τ_{PL}, which takes into account both the components, increases for all GUA loading conditions compared to the control perovskite. Specifically, the value increases from 89.90ns for a control sample to 119.76ns for G1. Similar values were observed for G2 as well, but the lifetime of carriers in G3 goes down relative to G1 and G2. This can be explained due to the induced passivation effect from adding GUAI on the perovskite surface and similar to the effect observed by Jiang *et al.* [217] from adding PEAI. The lower lifetime for G3 (3mg/ml) can be likely explained due to the partial formation of

GUAPbI$_3$ relatively higher than G1 and G2, on the surface of the perovskite, inhibiting charge transport. The nature of charge transport as related to the device performance is discussed in the following section.

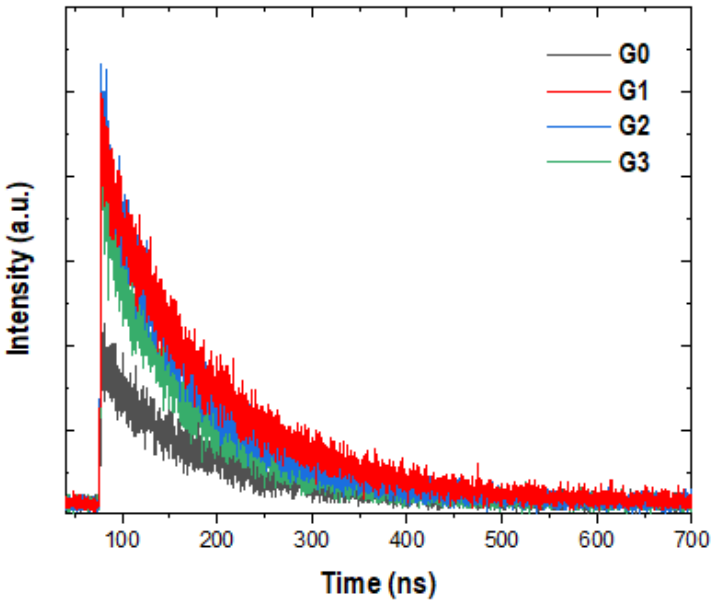

Fig. 7.5 Time-resolved PL spectra of perovskite with different GUA loading conditions

Table. 7.1. TRPL fitting parameters of perovskite with different GUAI loading conditions

Sample	τ_1(ns)	$\tau_{1\%}$	τ_2 (ns)	$\tau_{2\%}$	τ_{PL} (ns)
G0	60.64	46.34	115.19	53.65	89.90
G1	89.89	68.32	184.29	31.67	119.76
G2	77.98	62.43	188.41	37.56	119.46
G3	58.93	31.35	137.28	68.64	112.71

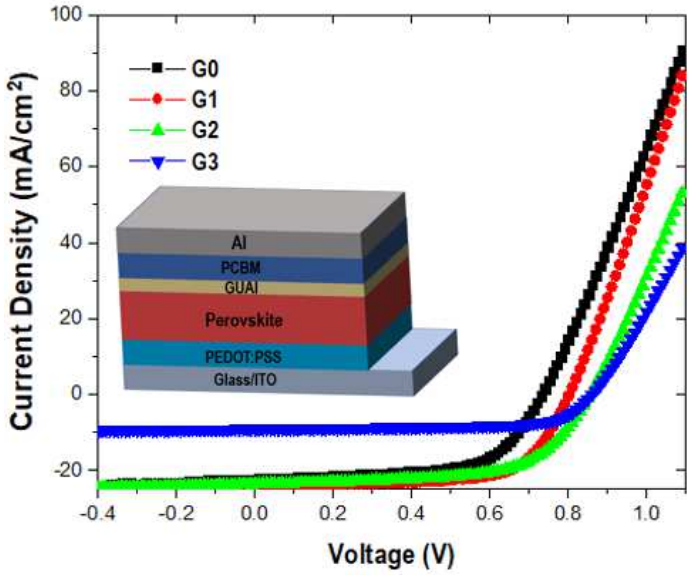

Fig. 7.6 Current-Voltage characteristics of perovskite device with different GUAI loading conditions

Table. 7.2 Solar cell device parameters of perovskite with different GUAI loading conditions

Device	J_{SC} [mA/cm^2]	V_{OC} [V]	FF	PCE [%]
G0	22.29	0.72	0.62	10.16
G1	23.78	0.80	0.68	13.01
G2	23.50	0.83	0.63	12.68
G3	9.18	0.86	0.69	5.50

Current-voltage characteristics were performed on devices prepared in an inverted configuration with PEDOT and PCBM as the hole and electron transport layers, respectively, and shown in Fig. 7.6 with the corresponding device parameters in Table 7.2. While the control device demonstrated a PCE of 10.16%, G1 and G2 demonstrated 13.01% and 12.68% in forward scans. The PCE values were not very high, possibly due to a slight mismatch between the energy levels of PEDOT/PCBM and the triple-cation perovskite. Ji

et al. demonstrated a PCE of 9.69% for a forward scan in a triple-cation perovskite device with PEDOT and PCBM as the HTL and ETL, respectively. They found that adding an optimized amount of Sn as a partial replacement to Pb would more suitably align the band levels and give a higher PCE of 16.10%. In our case, the V_{OC} was found to be improved for GUAI loaded samples, which is the reason behind the boost in efficiency to 13.01%. The primary reason behind the improved V_{OC} can be attributed to the surface passivation of defects on the perovskite. Increasing the concentration to 3mg/ml, however, results in lower efficiency due to the reduced current densities across the perovskite-charge transport layers interface. Small improvements in J_{SC} were also observed for low concentrations, G1 and G2, from 22.29mA/cm^2 for G0 to 23.78mA/cm^2 and 23.50mA/cm^2, respectively. These improvements can be attributed to the suppression of defects from adding GUAI. However, G3 shows a drastic decrease in J_{SC} to 9.18mA/cm^2 from the control device. Previous reports indicated GUAI could be insulating in nature, similar to PEAI, [217], which along with a partial formation of $GUAPbI_3$, would be the reason for the lower J_{SC} values.

For investigating the reproducibility in performance from the addition of GUAI, box plots of PCE are shown in Fig.7.7, which are the results of 8 devices fabricated with the same conditions. The corresponding plots of V_{OC}, J_{SC}, and FF are shown in Supplementary Figs. C3, C4, and C5, respectively. A similar trend in the values as the main data in the box plots with small distributions indicating good reproducibility.

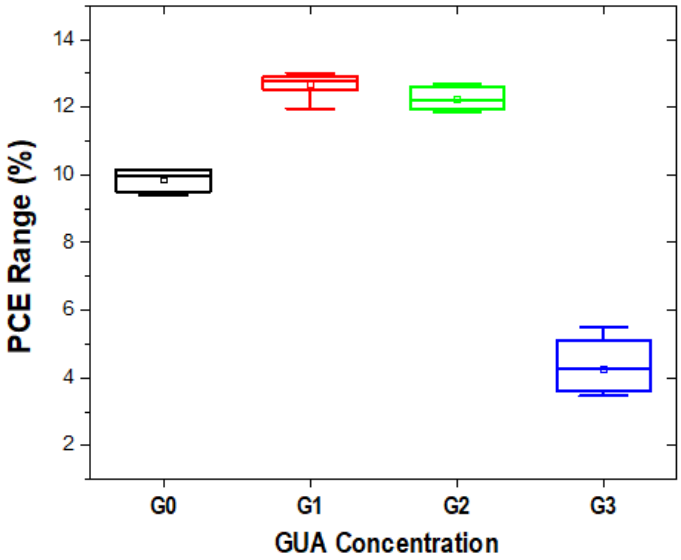

Fig. 7.7 Box plot of PCE for perovskite devices with different GUAI loading conditions

The stability of the devices prepared with different loading conditions was assessed and plotted the normalized device parameters of them tested over a period of 600 hours in Fig. 7.8. The samples were stored in the ambient between measurements. Both G1 and G2 devices demonstrate superior stability in PCE and only degraded by approximately 20%, compared to the control device, which decomposed by more than 40%. G3, however, degrades a little more (35%) relative to G1 and G2 but still proves to be more stable than the control device. Other device parameters are shown in Figs C6, C7, and C8. The J_{SC} values follow a similar trend in degradation along with FF, but the V_{OC} is shown to be retained over extended periods as opposed to decay of nearly 90% for the control device. The higher stability can be attributed to the passivation effect induced by the addition of GUAI on the perovskite.

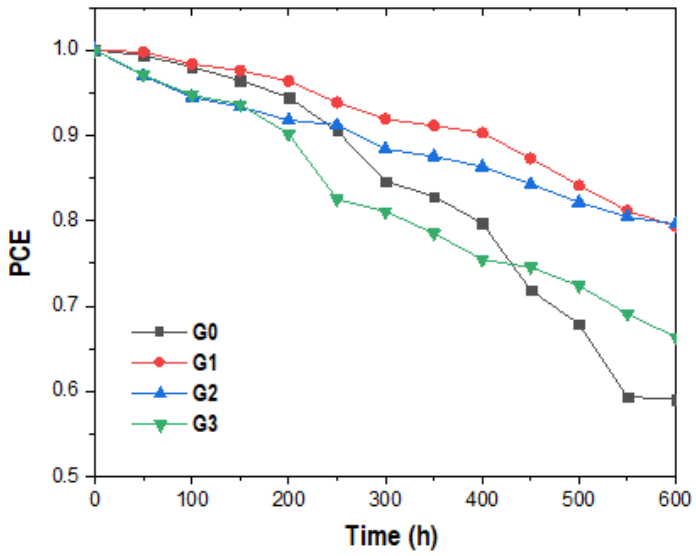

Fig. 7.8 PCE decay of perovskite devices with different GUAI loading conditions

7.4 Conclusion

To summarize, the effect of adding different concentrations of GUAI in IPA to triple-cation perovskite, and the resulting changes in selective properties was investigated. In this regard, three different concentrations of GUAI on perovskite were investigated. Although higher crystallization was not observed, a passivation effect is understood to be induced on the surface, especially on unreacted PbI_2. Analysis of the steady-state PL spectra shows improved intensity and lifetime on all GUA loaded samples compared to the control sample. The fitted parameters for the lifetime values indicate suppressed carrier recombination, and an overall reduced defect density for the GUA loaded samples. Device performance was then evaluated with respect to the control sample, and both 1mg/ml (G1) and 2mg/ml (G2) demonstrate superior performance with improved V_{OC}. Although an even higher V_{OC} was observed for a higher concentration of 3mg/ml (G3), J_{SC} was found to be low, likely due to the insulating nature of GUAI, resulting in minimized charge transport

across the interface between the perovskite and charge transport layers. Further studies on stability, evaluated over a period of 600 hours, demonstrate the retaining of V_{OC} for GUA-based devices with only a loss of 20% PCE observed, compared to the control device.

CHAPTER 8

SUMMARY AND FUTURE WORK

8.1 Summary

Perovskite Solar Cells (PSCs) have made huge strides in terms of progress in efficiency and stability compared to several alternative solar technologies. However, there is still a great need to push the limits and realize their potential even more, especially as the need for renewable technologies grows by the day. This work aims to investigate approaches for improving both the efficiency and operational stability of PSCs. Efforts were directed towards compositional tuning to realize superior morphologies and structures that can withstand moisture penetration and maintain high efficiency for extended periods while minimizing toxicity. The addition of new layers for inducing passivation of defects and traps, and improving the morphology and smoothness of the active layer and charge transport layers were also investigated.

In chapter 3, the addition of excess Pb to precursors for solution processing of $MAPbI_3$ was investigated. Improvements in the efficiency and overall stability were demonstrated for 5% excess Pb in the precursors. Chapter 4 discusses the effect of ZAC as a secondary buffer layer on PCBM for reduced roughness and to facilitate better charge extraction leading to the higher efficiency of $MAPbI_3$ devices. Chapter 5 discusses the introduction of Sr for partially replacing Pb, up to 30%, in $MAPbI_3$ perovskites, and demonstrates improved stability for 10% Sr alloyed devices.

Chapter 6 is focused on the role of introducing PEA cations into FAMACs triple-cation perovskite for improving the crystallinity and morphology of the perovskite. It was

demonstrated that 1.67% of PEA is optimal for obtaining a smooth and pinhole-free morphology, which results in better efficiency. In addition, the stability of the device was found to be improved due to reduced moisture penetration into the perovskite structure. Chapter 7 discusses the role of adding different concentrations of GUAI layers on top of triple-cation perovskite to induce a passivation effect and to suppress non-radiative recombination. Both 1mg/ml and 2mg/ml of GUAI in IPA proved to be effectively passivating the perovskite surface with a reduced amount of PbI_2 and increased minority carrier lifetimes. As a result, the efficiency was found to be improved for both 1mg/ml and 2mg/ml GUAI based devices, compared to the control perovskite device.

8.2 Future Work

Despite the remarkable progress achieved in the field of perovskites, questions remain regarding the commercial viability of perovskites as a mainstream solar cell technology. Some of these questions are critical to the development of perovskites, such as long-term operational stability and toxicity of Pb. While encapsulation methods were investigated to mitigate some of the issues, concerns remain on the use of organic components, which tend to degrade easily, and the environmental impact of Pb in the perovskite. Also, while the reduced cost of processing perovskite devices is considered a positive compared to Si-based solar cells, there is scope for research to further reduce the cost and to extend the fabrication to other than conventional glass-based substrates

Compositional engineering of perovskites can be done using simple solution processing routes, and materials with a variety of properties can be realized. The effect of large cation groups in the perovskite is a new area that is relatively underexplored. By

effectively tuning the ratios of the cation to anion within the Goldschmidt's tolerance factor, a large cation introduction can be explored in more detail to tune the bandgap for high absorption and material stability.

Although both planar and inverted architectures were demonstrated in perovskites, the majority of the focus of most research groups is on planar architectures. This interest is partly due to the ease of crystallization and interface formation of the perovskite on metal oxide layers. Several new compositions, especially triple-cation perovskites, hold great potential compared to single and dual cation perovskites. These new compositions need to be explored in more detail in an inverted configuration with polymer-based layers on the substrate. Research on inverted configurations improves the scope for the development of PSCs on flexible substrates and could increase their applicability to energy production technologies.

REFERENCES

[1] P. V. Kamat, Meeting the clean energy demand: Nanostructure architectures for solar energy conversion, J. Phys. Chem. C. 111 (2007) 2834-2860. doi:10.1021/jp066952u.

[2] C.B. Hatfield, Oil back on the global agenda, Nature. 387, 121 (1997). doi:10.1038/387121a0.

[3] J.L. Kolar, Alternative energy technologies, Environ. Qual. Manag. (2000). doi:10.1002/1520-6483(200024)10:2<45::AID-TQEM6>3.0.CO;2-P.

[4] S.A. Holditch, R.R. Chianelli, Factors that will influence oil and gas supply and demand in the 21st century, MRS Bull. (2008) 317-323. doi:10.1557/mrs2008.65.

[5] H.D. Matthews, N.P. Gillett, P.A. Stott, K. Zickfeld, The proportionality of global warming to cumulative carbon emissions, Nature. 459 (2009) 829–832. doi:10.1038/nature08047.

[6] M. Meinshausen, N. Meinshausen, W. Hare, S.C.B. Raper, K. Frieler, R. Knutti, D.J. Frame, M.R. Allen, Greenhouse-gas emission targets for limiting global warming to 2 °C, Nature. 458 (2009) 1158–1162. doi:10.1038/nature08017.

[7] D.P. Van Vuuren, M. Meinshausen, G.-K. Plattner, F. Joos, K.M. Strassmann, S.J. Smith, T.M.L. Wigley, S.C.B. Raper, K. Riahi, F. de la Chesnaye, M.G.J. den Elzen, J. Fujino, K. Jiang, N. Nakicenovic, S. Paltsev, J.M. Reilly, Temperature increase of 21st century mitigation scenarios., Proc. Natl. Acad. Sci. U. S. A. 105 (2008) 15258–62. doi:10.1073/pnas.0711129105.

[8] P. Friedlingstein, R.M. Andrew, J. Rogelj, G.P. Peters, J.G. Canadell, R. Knutti, G. Luderer, M.R. Raupach, M. Schaeffer, D.P. van Vuuren, C. Le Quéré, Persistent growth of CO2 emissions and implications for reaching climate targets, Nat. Geosci. 7 (2014) 709–715. doi:10.1038/ngeo2248.

[9] M. Hart, Hubris: The troubling science, economics, and politics of climate change, 2015. https://books.google.com/books?hl=en&lr=&id=B-OzCgAAQBAJ&oi=fnd&pg=PR7&ots=OyjRqiGVTW&sig=ylkjXkJ7VZDCo8nm6hJ9xNRMSt8 (accessed August 28, 2019).

[10] M. Luqman, S.R. Ahmad, S. Khan, U. Ahmad, A. Raza, F. Akmal, M. Luqman, S.R. Ahmad, S. Khan, U. Ahmad, A. Raza, F. Akmal, Estimation of Solar Energy Potential from Rooftop of Punjab Government Servants Cooperative Housing Society Lahore Using GIS, Smart Grid Renew. Energy. 06 (2015) 128–139. doi:10.4236/sgre.2015.65012.

[11] Clouds and the Earth's Radiant Energy System (CERES), (n.d.). https://ceres.larc.nasa.gov/ (accessed August 28, 2019).

[12] I. Renewable Energy Agency, Estimating the Renewable Energy Potential in Africa: A GIS-based approach, 2014. https://www.irena.org/DocumentDownloads/Publications/IRENA_Africa_Resource_Potential_Aug2014.pdf (accessed August 29, 2019).

[13] M. Adaramola, Solar energy : application, economics, and public perception, n.d. https://www.crcpress.com/Solar-Energy-Application-Economics-and-Public-Perception/Adaramola/p/book/9781771880909 (accessed August 29, 2019).

[14] R.W. Miles, G. Zoppi, I. Forbes, Inorganic photovoltaic cells, Mater. Today. 10 (2007) 20–27. doi:10.1016/S1369-7021(07)70275-4.

[15] M.A. Green, K. Emery, Y. Hishikawa, W. Warta, E.D. Dunlop, Solar cell efficiency tables (Version 45), Prog. Photovoltaics Res. Appl. 23 (2015) 1–9. doi:10.1002/pip.2573.

[16] H.J. (Hans J. Möller, Semiconductors for solar cells, Artech House, 1993. https://catalogue.nla.gov.au/Record/1195708 (accessed August 28, 2019).

[17] N.W. Ashcroft, N.D. Mermin, Solid state physics, Holt, Rinehart, and Winston, 1976.

[18] National Renewable Energy Laboratory efficiency-chart-20180716.jpg https://www.nrel.gov/pv/assets/images/efficiency-chart-20180716.jpg (accessed September 3, 2019).

[19] H. Hoppe, N.S. Sariciftci, Organic solar cells: An overview, J. Mater. Res. 19 (2004) 1924–1945. doi:10.1557/JMR.2004.0252.

[20] G.A. Chamberlain, Organic solar cells: A review, Sol. Cells. 8 (1983) 47–83. doi:10.1016/0379-6787(83)90039-X.

[21] J.M. Ball, M.M. Lee, A. Hey, H.J. Snaith, Low-temperature processed meso-superstructured to thin-film perovskite solar cells, Energy Environ. Sci. 6 (2013) 1739. doi:10.1039/c3ee40810h.

[22] C.J. Brabec, N.S. Sariciftci, J.C. Hummelen, Plastic Solar Cells, Adv. Funct. Mater. 11 (2001) 15–26. doi:10.1002/1616-3028(200102)11:1<15::AID-ADFM15>3.3.CO;2-1.

[23] G. Hadziioannou, G.G. Malliaras, Γ. Χατζηιωάννου, Γ.Γ. Μαλλιάρας, Semiconducting polymers : chemistry, physics, and engineering., Wiley-VCH,

2007. https://www.wiley.com/en-us/Semiconducting+Polymers%3A+Chemistry%2C+Physics+and+Engineering%2C+2nd+Edition%2C+Two+Volume+Set-p-9783527312719 (accessed August 29, 2019).

[24] B. Ratier, J.-M. Nunzi, M. Aldissi, T.M. Kraft, E. Buncel, Organic solar cell materials and active layer designs-improvements with carbon nanotubes: a review, Polym. Int. 61 (2012) 342–354. doi:10.1002/pi.3233.

[25] M.H. Kumar, N. Yantara, S. Dharani, M. Graetzel, P.P. Boix, N. Mathews, Flexible, low-temperature, solution processed ZnO-based perovskite solid state solar cells, Chem. Commun. 49 (2013) 11089–11091. doi:10.1039/c3cc46534a.

[26] S.S. Shin, W.S. Yang, J.H. Noh, J.H. Suk, N.J. Jeon, J.H. Park, J.S. Kim, W.M. Seong, S. Il Seok, High-performance flexible perovskite solar cells exploiting Zn2SnO4 prepared in solution below 100 °C, Nat. Commun. 6 (2015) 1–8. doi:10.1038/ncomms8410.

[27] D. Liu, T.L. Kelly, Perovskite solar cells with a planar heterojunction structure prepared using room-temperature solution processing techniques, Nat. Photonics. 8 (2013) 133–138. doi:10.1038/nphoton.2013.342.

[28] G. Niu, X. Guo, L. Wang, Review of recent progress in chemical stability of perovskite solar cells, J. Mater. Chem. A. 3 (2015) 8970–8980. doi:10.1039/c4ta04994b.

[29] M. Grätzel, The light and shade of perovskite solar cells, Nat. Mater. 13 (2014) 838–842. doi:10.1038/nmat4065.

[30] L. Schmidt-Mende, J. Weickert, Organic and hybrid solar cells : an introduction, n.d.

[31] M. He, D. Zheng, M. Wang, C. Lin, Z. Lin, High efficiency perovskite solar cells: from complex nanostructure to planar heterojunction, J. Mater. Chem. A. 2 (2014) 5994–6003. doi:10.1039/C3TA14160H.

[32] J.S. Yun, A. Ho-Baillie, S. Huang, S.H. Woo, Y. Heo, J. Seidel, F. Huang, Y.-B. Cheng, M.A. Green, Benefit of Grain Boundaries in Organic–Inorganic Halide Planar Perovskite Solar Cells, J. Phys. Chem. Lett. 6 (2015) 875–880. doi:10.1021/acs.jpclett.5b00182.

[33] I. Mesquita, L. Andrade, A. Mendes, Perovskite solar cells: Materials, configurations and stability, Renew. Sustain. Energy Rev. 82 (2018) 2471–2489. doi:10.1016/J.RSER.2017.09.011.

[34] H.S. Jung, N.G. Park, Perovskite solar cells: From materials to devices, Small. 11 (2015) 10–25. doi:10.1002/smll.201402767.

[35] N. Marinova, S. Valero, J.L. Delgado, Organic and perovskite solar cells: Working principles, materials and interfaces, J. Colloid Interface Sci. 488 (2017) 373–389. doi:10.1016/J.JCIS.2016.11.021.

[36] J.-L. Brédas, J.E. Norton, J. Cornil, V. Coropceanu, Molecular Understanding of Organic Solar Cells: The Challenges, Acc. Chem. Res. 42 (2009) 1691–1699. doi:10.1021/ar900099h.

[37] G. Xing, N. Mathews, S. Sun, S.S. Lim, Y.M. Lam, M. Graẗzel, S. Mhaisalkar, T.C. Sum, Long-range balanced electron-and hole-transport lengths in organic-inorganic CH3NH3PbI3, Science. 342 (2013) 344–347. doi:10.1126/science.1243167.

[38] S.D. Stranks, G.E. Eperon, G. Grancini, C. Menelaou, M.J.P. Alcocer, T. Leijtens, L.M. Herz, A. Petrozza, H.J. Snaith, Electron-hole diffusion lengths exceeding 1 micrometer in an organometal trihalide perovskite absorber, Science. 342 (2013) 341–344. doi:10.1126/science.1243982.

[39] Q. Lin, A. Armin, R. Chandra, R. Nagiri, P.L. Burn, P. Meredith, Electro-optics of perovskite solar cells, 9 (2015) 106-115. doi:10.1038/NPHOTON.2014.284.

[40] F. Zheng, L.Z. Tan, S. Liu, A.M. Rappe, Rashba spin-orbit coupling enhanced carrier lifetime in CH 3 NH 3 PbI 3, Nano Lett. 15 (2015) 7794–7800. doi:10.1021/acs.nanolett.5b01854.

[41] L.M. Herz, Charge-Carrier Dynamics in Organic-Inorganic Metal Halide Perovskites, Annu. Rev. Phys. Chem. 67 (2016) 65–89. doi:10.1146/annurev-physchem-040215-112222.

[42] D. Bi, C. Yi, J. Luo, J.-D. Décoppet, F. Zhang, S.M. Zakeeruddin, X. Li, A. Hagfeldt, M. Grätzel, Polymer-templated nucleation and crystal growth of perovskite films for solar cells with efficiency greater than 21%, Nat. Energy. 1 (2016) 16142. doi:10.1038/nenergy.2016.142.

[43] E.H. Anaraki, A. Kermanpur, L. Steier, K. Domanski, T. Matsui, W. Tress, M. Saliba, A. Abate, M. Grätzel, A. Hagfeldt, J.-P. Correa-Baena, Highly efficient and stable planar perovskite solar cells by solution-processed tin oxide, Energy Environ. Sci. 9 (2016) 3128–3134. doi:10.1039/C6EE02390H.

[44] M.I. Dar, F.J. Ramos, Z. Xue, B. Liu, S. Ahmad, S.A. Shivashankar, M.K. Nazeeruddin, M. Grätzel, Photoanode Based on (001)-Oriented Anatase Nanoplatelets for Organic–Inorganic Lead Iodide Perovskite Solar Cell, Chem. Mater. 26 (2014) 4675–4678. doi:10.1021/cm502185s.

[45] Y. Shao, Z. Xiao, C. Bi, Y. Yuan, J. Huang, Origin and elimination of photocurrent hysteresis by fullerene passivation in CH3NH3PbI3planar heterojunction solar cells, Nat. Commun. 5 (2014). doi:10.1038/ncomms6784.

[46] Y. Guo, C. Liu, K. Inoue, K. Harano, H. Tanaka, E. Nakamura, Enhancement in the efficiency of an organic–inorganic hybrid solar cell with a doped P3HT hole-transporting layer on a void-free perovskite active layer, J. Mater. Chem. A. 2 (2014) 13827–13830. doi:10.1039/C4TA02976C.

[47] J.Y. Jeng, Y.F. Chiang, M.H. Lee, S.R. Peng, T.F. Guo, P. Chen, T.C. Wen, CH3NH3PbI3 perovskite/fullerene planar-heterojunction hybrid solar cells, Adv. Mater. 25 (2013) 3727–3732. doi:10.1002/adma.201301327.

[48] C.Y. Chang, W.K. Huang, J.L. Wu, Y.C. Chang, K.T. Lee, C.T. Chen, Room-Temperature Solution-Processed n-Doped Zirconium Oxide Cathode Buffer Layer for Efficient and Stable Organic and Hybrid Perovskite Solar Cells, Chem. Mater. 28 (2016) 242–251. doi:10.1021/acs.chemmater.5b03991.

[49] L. Hu, J. Peng, W. Wang, Z. Xia, J. Yuan, J. Lu, X. Huang, W. Ma, H. Song, W. Chen, Y.-B. Cheng, J. Tang, Sequential Deposition of $CH_3NH_3PbI_3$ on Planar NiO Film for Efficient Planar Perovskite Solar Cells, ACS Photonics. 1 (2014) 547–553. doi:10.1021/ph5000067.

[50] Z. Zhu, Y. Bai, X. Liu, C.-C. Chueh, S. Yang, A.K.-Y. Jen, Enhanced Efficiency and Stability of Inverted Perovskite Solar Cells Using Highly Crystalline SnO_2 Nanocrystals as the Robust Electron-Transporting Layer, Adv. Mater. 28 (2016) 6478–6484. doi:10.1002/adma.201600619.

[51] N.J. Jeon, J.H. Noh, W.S. Yang, Y.C. Kim, S. Ryu, J. Seo, S. Il Seok, Compositional engineering of perovskite materials for high-performance solar cells, Nature. (2015). doi:10.1038/nature14133.

[52] Y. Rong, Y. Hu, A. Mei, H. Tan, M.I. Saidaminov, S. Il Seok, M.D. McGehee, E.H. Sargent, H. Han, Challenges for commercializing perovskite solar cells, Science. 361 (2018). doi:10.1126/science.aat8235.

[53] K. Domanski, E.A. Alharbi, A. Hagfeldt, M. Grätzel, W. Tress, Systematic investigation of the impact of operation conditions on the degradation behaviour of perovskite solar cells, Nat. Energy. 3 (2018) 61–67. doi:10.1038/s41560-017-0060-5.

[54] M. Jung, S.G. Ji, G. Kim, S. Il Seok, Perovskite precursor solution chemistry: From fundamentals to photovoltaic applications, Chem. Soc. Rev. 48 (2019) 2011–2038. doi:10.1039/c8cs00656c.

[55] V.M. Goldschmidt, The principles of distribution of chemical elements in minerals and rocks. The seventh Hugo Müller Lecture, delivered before the Chemical Society on March 17th, 1937, J. Chem. Soc. 0 (1937) 655–673. doi:10.1039/JR9370000655.

[56] H. Chen, F. Ye, W. Tang, J. He, M. Yin, Y. Wang, F. Xie, E. Bi, X. Yang, M. Grätzel, L. Han, A solvent-and vacuum-free route to large-area perovskite films for efficient solar modules, Nature. 550 (2017) 92–95. doi:10.1038/nature23877.

[57] N.K. Noel, S.N. Habisreutinger, B. Wenger, M.T. Klug, M.T. Hörantner, M.B. Johnston, R.J. Nicholas, D.T. Moore, H.J. Snaith, A low viscosity, low boiling point, clean solvent system for the rapid crystallisation of highly specular perovskite films, Energy Environ. Sci. 10 (2017) 145–152. doi:10.1039/c6ee02373h.

[58] W. Ke, M.G. Kanatzidis, Prospects for low-toxicity lead-free perovskite solar cells, Nat. Commun. 10 (2019) 965. doi:10.1038/s41467-019-08918-3.

[59] F. Giustino, H.J. Snaith, Toward Lead-Free Perovskite Solar Cells, ACS Energy Lett. 1 (2016) 1233–1240. doi:10.1021/acsenergylett.6b00499.

[60] W. Ke, C.C. Stoumpos, M.G. Kanatzidis, "Unleaded" Perovskites: Status Quo and Future Prospects of Tin-Based Perovskite Solar Cells, Adv. Mater. 31 (2019). doi:10.1002/adma.201803230.

[61] F. Hao, C.C. Stoumpos, D.H. Cao, R.P.H. Chang, M.G. Kanatzidis, Lead-free solid-state organic-inorganic halide perovskite solar cells, Nat. Photonics. (2014). doi:10.1038/nphoton.2014.82.

[62] E. Jokar, C.H. Chien, C.M. Tsai, A. Fathi, E.W.G. Diau, Robust Tin-Based Perovskite Solar Cells with Hybrid Organic Cations to Attain Efficiency Approaching 10%, Adv. Mater. 31 (2019) 1804835. doi:10.1002/adma.201804835.

[63] M. Chen, M.G. Ju, H.F. Garces, A.D. Carl, L.K. Ono, Z. Hawash, Y. Zhang, T. Shen, Y. Qi, R.L. Grimm, D. Pacifici, X.C. Zeng, Y. Zhou, N.P. Padture, Highly stable and efficient all-inorganic lead-free perovskite solar cells with native-oxide passivation, Nat. Commun. 10 (2019). doi:10.1038/s41467-018-07951-y.

[64] C.F.J. Lau, M. Zhang, X. Deng, J. Zheng, J. Bing, Q. Ma, J. Kim, L. Hu, M.A. Green, S. Huang, A. Ho-Baillie, Strontium-Doped Low-Temperature-Processed CsPbI2Br Perovskite Solar Cells, ACS Energy Lett. (2017). doi:10.1021/acsenergylett.7b00751.

[65] D. Pérez-del-Rey, D. Forgács, E.M. Hutter, T.J. Savenije, D. Nordlund, P. Schulz, J.J. Berry, M. Sessolo, H.J. Bolink, Strontium Insertion in Methylammonium Lead Iodide: Long Charge Carrier Lifetime and High Fill-Factor Solar Cells, Adv. Mater. (2016). doi:10.1002/adma.201603016.

[66] J.P. Correa-Baena, M. Saliba, T. Buonassisi, M. Grätzel, A. Abate, W. Tress, A. Hagfeldt, Promises and challenges of perovskite solar cells, Science (80-.). 358 (2017) 739–744. doi:10.1126/science.aam6323.

[67] B. Conings, J. Drijkoningen, N. Gauquelin, A. Babayigit, J. D'Haen, L. D'Olieslaeger, A. Ethirajan, J. Verbeeck, J. Manca, E. Mosconi, F. De Angelis, H.-G. Boyen, Intrinsic Thermal Instability of Methylammonium Lead Trihalide Perovskite, Adv. Energy Mater. 5 (2015) 1500477. doi:10.1002/aenm.201500477.

[68] W. Liu, T. Wu, M. Liu, W. Niu, Y. Chueh, Recent Challenges in Perovskite Solar Cells Toward Enhanced Stability, Less Toxicity, and Large□Area Mass Production, Adv. Mater. Interfaces. 6 (2019) 1801758. doi:10.1002/admi.201801758.

[69] Z. Cheng, J. Lin, Layered organic-inorganic hybrid perovskites: Structure, optical properties, film preparation, patterning and templating engineering, CrystEngComm. 12 (2010) 2646–2662. doi:10.1039/c001929a.

[70] J. You, L. Meng, T. Bin Song, T.F. Guo, W.H. Chang, Z. Hong, H. Chen, H. Zhou, Q. Chen, Y. Liu, N. De Marco, Y. Yang, Improved air stability of perovskite solar cells via solution-processed metal oxide transport layers, Nat. Nanotechnol. 11 (2016) 75–81. doi:10.1038/nnano.2015.230.

[71] M. Saliba, T. Matsui, K. Domanski, J.-Y. Seo, A. Ummadisingu, S.M. Zakeeruddin, J.-P. Correa-Baena, W.R. Tress, A. Abate, A. Hagfeldt, M. Grätzel, Incorporation of rubidium cations into perovskite solar cells improves photovoltaic performance., Science. 354 (2016) 206–209. doi:10.1126/science.aah5557.

[72] M. Saliba, T. Matsui, J.Y. Seo, K. Domanski, J.P. Correa-Baena, M.K. Nazeeruddin, S.M. Zakeeruddin, W. Tress, A. Abate, A. Hagfeldt, M. Grätzel, Cesium-containing triple-cation perovskite solar cells: Improved stability, reproducibility and high efficiency, Energy Environ. Sci. 9 (2016) 1989–1997. doi:10.1039/c5ee03874j.

[73] A. Amat, E. Mosconi, E. Ronca, C. Quarti, P. Umari, M.K. Nazeeruddin, M. Grätzel, F. De Angelis, Cation-induced band-gap tuning in organohalide perovskites: Interplay of spin-orbit coupling and octahedra tilting, Nano Lett. 14 (2014) 3608–3616. doi:10.1021/nl5012992.

[74] Z. Wang, D.P. McMeekin, N. Sakai, S. van Reenen, K. Wojciechowski, J.B. Patel, M.B. Johnston, H.J. Snaith, Efficient and Air-Stable Mixed-Cation Lead Mixed-Halide Perovskite Solar Cells with n-Doped Organic Electron Extraction Layers, Adv. Mater. (2017). doi:10.1002/adma.201604186.

[75] H. Tan, A. Jain, O. Voznyy, X. Lan, F.P.G. De Arquer, J.Z. Fan, R. Quintero-Bermudez, M. Yuan, B. Zhang, Y. Zhao, F. Fan, P. Li, L.N. Quan, Y. Zhao, Z.H. Lu, Z. Yang, S. Hoogland, E.H. Sargent, Efficient and stable solution-processed

planar perovskite solar cells via contact passivation, Science. 355 (2017) 722–726. doi:10.1126/science.aai9081.

[76] P. Kung, M. Li, P. Lin, Y. Chiang, C. Chan, T. Guo, P. Chen, A Review of Inorganic Hole Transport Materials for Perovskite Solar Cells, Adv. Mater. Interfaces. 5 (2018) 1800882. doi:10.1002/admi.201800882.

[77] D. Bi, C. Yi, J. Luo, J.D. Décoppet, F. Zhang, S.M. Zakeeruddin, X. Li, A. Hagfeldt, M. Grätzel, Polymer-templated nucleation and crystal growth of perovskite films for solar cells with efficiency greater than 21%, Nat. Energy. 1 (2016) 1–5. doi:10.1038/nenergy.2016.142.

[78] J.H. Heo, M.S. You, M.H. Chang, W. Yin, T.K. Ahn, S.-J. Lee, S.-J. Sung, D.H. Kim, S.H. Im, Hysteresis-less mesoscopic CH3NH3PbI3 perovskite hybrid solar cells by introduction of Li-treated TiO2 electrode, Nano Energy. 15 (2015) 530–539. doi:10.1016/j.nanoen.2015.05.014.

[79] Z. Liu, L. Qiu, E.J. Juarez-Perez, Z. Hawash, T. Kim, Y. Jiang, Z. Wu, S.R. Raga, L.K. Ono, S. Liu, Y. Qi, Gas-solid reaction based over one-micrometer thick stable perovskite films for efficient solar cells and modules, Nat. Commun. 9 (2018) 3880. doi:10.1038/s41467-018-06317-8.

[80] Y. Rong, Y. Ming, W. Ji, D. Li, A. Mei, Y. Hu, H. Han, Toward Industrial-Scale Production of Perovskite Solar Cells: Screen Printing, Slot-Die Coating, and Emerging Techniques, J. Phys. Chem. Lett. 9 (2018) 2707–2713. doi:10.1021/acs.jpclett.8b00912.

[81] J.Y. Kim, K. Lee, N.E. Coates, D. Moses, T.Q. Nguyen, M. Dante, A.J. Heeger, Efficient tandem polymer solar cells fabricated by all-solution processing, Science (80-.). 317 (2007) 222–225. doi:10.1126/science.1141711.

[82] H.-Y.Y. Chen, J.H. Hou, S.Q. Zhang, Y.Y. Liang, G.W. Yang, Y. Yang, L.P. Yu, Y. Wu, G. Li, Polymer solar cells with enhanced open-circuit voltage and efficiency, Nat. Photonics. 3 (2009) 649–653. doi:10.1038/nphoton.2009.192.

[83] A. Kojima, K. Teshima, Y. Shirai, T. Miyasaka, Organometal halide perovskites as visible-light sensitizers for photovoltaic cells, J. Am. Chem. Soc. 131 (2009) 6050–6051. doi:10.1021/ja809598r.

[84] M.M. Lee, J. Teuscher, T. Miyasaka, T.N. Murakami, H.J. Snaith, Efficient Hybrid Solar Cells Based on Meso-Superstructured Organometal Halide Perovskites, Science (80-.). 338 (2012) 643–647. doi:10.1126/science.1228604.

[85] H. Zhou, Q. Chen, G. Li, S. Luo, T. Song, H.-S. Duan, Z. Hong, J. You, Y. Liu, Y. Yang, Interface engineering of highly efficient perovskite solar cells, Sci.

(Washington, DC, U. S.). 345 (2014) 542–546. doi:10.1126/science.1254050.

[86] N.J. Jeon, J.H. Noh, Y.C. Kim, W.S. Yang, S. Ryu, S. Il Seok, Solvent engineering for high-performance inorganic-organic hybrid perovskite solar cells, Nat. Mater. 13 (2014) 897–903. doi:10.1038/nmat4014.

[87] S. Guarnera, A. Abate, W. Zhang, J.M. Foster, G. Richardson, A. Petrozza, H.J. Snaith, Improving the Long-Term Stability of Perovskite Solar Cells with a Porous Al 2 O 3 Buffer Layer, J. Phys. Chem. Lett. 6 (2015) 432–437. doi:10.1021/jz502703p.

[88] M. Bag, L.A. Renna, R.Y. Adhikari, S. Karak, F. Liu, P.M. Lahti, T.P. Russell, M.T. Tuominen, D. Venkataraman, Kinetics of Ion Transport in Perovskite Active Layers and Its Implications for Active Layer Stability, J. Am. Chem. Soc. 137 (2015) 13130–13137. doi:10.1021/jacs.5b08535.

[89] X. Li, D. Bi, C. Yi, J.-D. Décoppet, J. Luo, S.M. Zakeeruddin, A. Hagfeldt, M. Grätzel , A vacuum flash-assisted solution process for high-efficiency large-area perovskite solar cells., Science. 353 (2016) 58–62. doi:10.1126/science.aaf8060.

[90] B. Roose, J.P.C. Baena, K.C. Gödel, M. Graetzel, A. Hagfeldt, U. Steiner, A. Abate, Mesoporous SnO2electron selective contact enables UV-stable perovskite solar cells, Nano Energy. 30 (2016) 517–522. doi:10.1016/j.nanoen.2016.10.055.

[91] T. Leijtens, G.E. Eperon, S. Pathak, A. Abate, M.M. Lee, H.J. Snaith, Overcoming ultraviolet light instability of sensitized TiO2 with meso-superstructured organometal tri-halide perovskite solar cells, Nat. Commun. 4 (2013). doi:10.1038/ncomms3885.

[92] S. Ito, S. Tanaka, K. Manabe, H. Nishino, Effects of surface blocking layer of Sb2S3 on nanocrystalline TiO2 for CH3NH3PbI3 perovskite solar cells, J. Phys. Chem. C. 118 (2014) 16995–17000. doi:10.1021/jp500449z.

[93] R.K. Misra, S. Aharon, B. Li, D. Mogilyansky, I. Visoly-Fisher, L. Etgar, E.A. Katz, Temperature- and component-dependent degradation of perovskite photovoltaic materials under concentrated sunlight, J. Phys. Chem. Lett. 6 (2015) 326–330. doi:10.1021/jz502642b.

[94] D. Wei, T. Wang, J. Ji, M. Li, P. Cui, Y. Li, G. Li, J.M. Mbengue, D. Song, Photo-induced degradation of lead halide perovskite solar cells caused by the hole transport layer/metal electrode interface, J. Mater. Chem. A. 4 (2016) 1991–1998. doi:10.1039/C5TA08622A.

[95] H. Yuan, E. Debroye, K. Janssen, H. Naiki, C. Steuwe, G. Lu, M. Moris, E. Orgiu, H. Uji-i, F. De Schryver, P. Samorì, J. Hofkens, M. Roeffaers, Degradation of

Methylammonium Lead Iodide Perovskite Structures through Light and Electron Beam Driven Ion Migration, J. Phys. Chem. Lett. 7 (2016) 561–566. doi:10.1021/acs.jpclett.5b02828.

[96] D. Song, J. Ji, Y. Li, G. Li, M. Li, T. Wang, D. Wei, P. Cui, Y. He, J.M. Mbengue, Degradation of organometallic perovskite solar cells induced by trap states, Appl. Phys. Lett. 108 (2016) 093901. doi:10.1063/1.4943019.

[97] W. Nie, J.C. Blancon, A.J. Neukirch, K. Appavoo, H. Tsai, M. Chhowalla, M.A. Alam, M.Y. Sfeir, C. Katan, J. Even, S. Tretiak, J.J. Crochet, G. Gupta, A.D. Mohite, Light-activated photocurrent degradation and self-healing in perovskite solar cells, Nat. Commun. 7 (2016). doi:10.1038/ncomms11574.

[98] C. Qin, T. Matsushima, T. Fujihara, W.J. Potscavage, C. Adachi, Degradation Mechanisms of Solution-Processed Planar Perovskite Solar Cells: Thermally Stimulated Current Measurement for Analysis of Carrier Traps, Adv. Mater. 28 (2016) 466–471. doi:10.1002/adma.201502610.

[99] A. Dualeh, N. Tétreault, T. Moehl, P. Gao, M.K. Nazeeruddin, M. Grätzel, Effect of annealing temperature on film morphology of organic-inorganic hybrid pervoskite solid-state solar cells, Adv. Funct. Mater. 24 (2014) 3250–3258. doi:10.1002/adfm.201304022.

[100] X. Li, M.I. Dar, C.Y. Yi, J.S. Luo, M. Tschumi, S.M. Zakeeruddin, M.K. Nazeeruddin, H.W. Han, M. Gratzel, Improved performance and stability of perovskite solar cells by crystal crosslinking with alkylphosphonic acid omega-ammonium chlorides, Nat. Chem. 7 (2015) 703–711. doi:10.1038/Nchem.2324.

[101] Z. Yang, A. Rajagopal, S.B. Jo, C.C. Chueh, S. Williams, C.C. Huang, J.K. Katahara, H.W. Hillhouse, A.K.Y. Jen, Stabilized Wide Bandgap Perovskite Solar Cells by Tin Substitution, Nano Lett. 16 (2016) 7739–7747. doi:10.1021/acs.nanolett.6b03857.

[102] W. Qiu, T. Merckx, M. Jaysankar, C. Masse de la Huerta, L. Rakocevic, W. Zhang, U.W. Paetzold, R. Gehlhaar, L. Froyen, J. Poortmans, D. Cheyns, H.J. Snaith, P. Heremans, Pinhole-Free Perovskite Films for Efficient Solar Modules, Energy Environ. Sci. 9 (2016) DOI: 10.1039/C5EE03703D. doi:10.1039/C5EE03703D.

[103] C. Qin, T. Matsushima, T. Fujihara, C. Adachi, Multifunctional Benzoquinone Additive for Efficient and Stable Planar Perovskite Solar Cells, Adv. Mater. 29 (2017). doi:10.1002/adma.201603808.

[104] Y. Chen, A. Yerramilli, Y. Shen, Z. Zhao, T. Alford, Effect of excessive Pb content in the precursor solutions on the properties of the lead acetate derived CH3NH3PbI3perovskite solar cells, Sol. Energy Mater. Sol. Cells. 174 (2018) 478–

484. doi:10.1016/j.solmat.2017.09.039.

[105] R.K. Misra, S. Aharon, B. Li, D. Mogilyansky, I. Visoly-Fisher, L. Etgar, E.A. Katz, Temperature- and Component-Dependent Degradation of Perovskite Photovoltaic Materials under Concentrated Sunlight, J. Phys. Chem. Lett. 6 (2015) 326–330. doi:10.1021/jz502642b.

[106] L. Wang, C. McCleese, A. Kovalsky, Y. Zhao, C. Burda, Femtosecond Time-Resolved Transient Absorption Spectroscopy of CH3NH3PbI3 Perovskite Films: Evidence for Passivation Effect of PbI2, J. Am. Chem. Soc. 110 (2014) 140822082052002. doi:10.1021/ja504632z.

[107] Q. Chen, H. Zhou, T. Bin Song, S. Luo, Z. Hong, H.S. Duan, L. Dou, Y. Liu, Y. Yang, Controllable self-induced passivation of hybrid lead iodide perovskites toward high performance solar cells, Nano Lett. 14 (2014) 4158–4163. doi:10.1021/nl501838y.

[108] J. Seo, S. Park, Y. Chan Kim, N.J. Jeon, J.H. Noh, S.C. Yoon, S. Il Seok, Benefits of very thin PCBM and LiF layers for solution-processed p–i–n perovskite solar cells, Energy Environ. Sci. 7 (2014) 2642–2646. doi:10.1039/C4EE01216J.

[109] K.M. Coakley, M.D. McGehee, Conjugated polymer photovoltaic cells, Chem. Mater. 16 (2004) 4533–4542. doi:10.1021/cm049654n.

[110] P. Gao, M. Gratzel, M.K. Nazeeruddin, N. Mohammad K., P. Gao, M. Grätzel, M. Gratzel, M.K. Nazeeruddin, N. Mohammad K., P. Gao, M. Grätzel, M. Gratzel, M.K. Nazeeruddin, N. Mohammad K., P. Gao, M. Grätzel, M. Gratzel, M.K. Nazeeruddin, Organohalide Lead Perovskites for Photovoltaic Applications, Energy Environ. Sci. 7 (2014) 2448–2463. doi:10.1039/C4EE00942H.

[111] Z. He, H. Wu, Y. Cao, Recent advances in polymer solar cells: Realization of high device performance by incorporating water/alcohol-soluble conjugated polymers as electrode buffer layer, Adv. Mater. 26 (2014) 1006–1024. doi:10.1002/adma.201303391.

[112] F. Wang, Z. Tan, Y. Li, Solution-processable metal oxides/chelates as electrode buffer layers for efficient and stable polymer solar cells, Energy Environ. Sci. 8 (2015) 1059–1091. doi:10.1039/c4ee03802a.

[113] T. Yang, W. Cai, D. Qin, E. Wang, L. Lan, X. Gong, J. Peng, Y. Cao, Solution-Processed Zinc Oxide Thin Film as a Buffer Layer for Polymer Solar Cells with an Inverted Device Structure, J. Phys. Chem. C. (2010). doi:10.1021/jp1003984.

[114] J.Y. Kim, S.H. Kim, H.H. Lee, K. Lee, W. Ma, X. Gong, A.J. Heeger, New architecture for high-efficiency polymer photovoltaic cells using solution-based

titanium oxide as an optical spacer, Adv. Mater. (2006). doi:10.1002/adma.200501825.

[115] J.J. Jasieniak, N.D. Treat, C.R. Mcneill, B.J.T. de Villers, E. Della Gaspera, M.L. Chabinyc, Interfacial Characteristics of Efficient Bulk Heterojunction Solar Cells Fabricated on MoOx Anode Interlayers, Adv. Mater. (2015). doi:10.1002/adma.201503309.

[116] J.R. Manders, S.-W. Tsang, M.J. Hartel, T.-H. Lai, S. Chen, C.M. Amb, J.R. Reynolds, F. So, Solution-Processed Nickel Oxide Hole Transport Layers in High Efficiency Polymer Photovoltaic Cells, Adv. Funct. Mater. (2013). doi:10.1002/adfm.201202269.

[117] K. Wang, Y. Shi, B. Li, L. Zhao, W. Wang, X. Wang, X. Bai, S. Wang, C. Hao, T. Ma, Amorphous Inorganic Electron-Selective Layers for Efficient Perovskite Solar Cells: Feasible Strategy Towards Room-Temperature Fabrication, Adv. Mater. (2016). doi:10.1002/adma.201505241.

[118] Z. Tan, S. Li, F. Wang, D. Qian, J. Lin, J. Hou, Y. Li, High performance polymer solar cells with as-prepared zirconium acetylacetonate film as cathode buffer layer, Sci. Rep. 4 (2015). doi:10.1038/srep04691.

[119] H. Fan, X. Zhu, High-Performance Inverted Polymer Solar Cells with Zirconium Acetylacetonate Buffer Layers, ACS Appl. Mater. Interfaces. 8 (2016) 33856–33862. doi:10.1021/acsami.6b11636.

[120] H. Kim, K.-G. Lim, T.-W. Lee, Planar heterojunction organometal halide perovskite solar cells: roles of interfacial layers, Energy Environ. Sci. 9 (2016) 12–30. doi:10.1039/C5EE02194D.

[121] I. Hancox, E. New, T.S. Jones, Utilising solution processed zirconium acetylacetonate as an electron extracting layer in both regular and inverted small molecule organic photovoltaic cells, Org. Electron. Physics, Mater. Appl. (2015). doi:10.1016/j.orgel.2015.04.019.

[122] S. Yue, kong liu, R. XU, M. Li, M. Azam, K. Ren, J. Liu, yang sun, Z. Wang, D. Cao, X. Yan, S. Qu, Y. Lei, wang zhanguo, Efficacious engineering on charge extraction for realizing high-efficient perovskite solar cells, Energy Environ. Sci. (2017). doi:10.1039/C7EE02685D.

[123] X. Zhang, C. Liang, M. Sun, H. Zhang, C. Ji, Z. Guo, Y. Xu, F. Sun, Q. Song, Z. He, Improved fill factor in inverted planar perovskite solar cells with zirconium acetate as the hole-and-ion-blocking layer, Phys. Chem. Chem. Phys. (2018). doi:10.1039/C8CP00563J.

[124] K. Zhang, C. Zhong, S. Liu, C. Mu, Z. Li, H. Yan, F. Huang, Y. Cao, Highly Efficient Inverted Polymer Solar Cells Based on a Cross-linkable Water-/Alcohol-Soluble Conjugated Polymer Interlayer, ACS Appl. Mater. Interfaces. 6 (2014) 10429–10435. doi:10.1021/am501920z.

[125] Y. Chen, A. Yerramilli, Y. Shen, Z. Zhao, T. Alford, Effect of excessive Pb content in the precursor solutions on the properties of the lead acetate derived CH3NH3PbI3 perovskite solar cells, Sol. Energy Mater. Sol. Cells. 174 (2018). doi:10.1016/j.solmat.2017.09.039.

[126] Y. Chen, A.S. Yerramilli, L. Li, W. Qu, Y. Shen, Y. Song, T.L. Alford, Control of the Nucleation and Growth of the Lead Acetate Solution Derived CH 3 NH 3 PbI 3 Films Leads to Enhanced Power Conversion Efficiency, ACS Appl. Energy Mater. (2018) acsaem.8b00561. doi:10.1021/acsaem.8b00561.

[127] U.K. Thakur, A.M. Askar, R. Kisslinger, B.D. Wiltshire, P. Kar, K. Shankar, Halide perovskite solar cells using monocrystalline TiO $_2$ nanorod arrays as electron transport layers: impact of nanorod morphology, Nanotechnology. 28 (2017) 274001. doi:10.1088/1361-6528/aa75ab.

[128] Y. Hou, X. Du, S. Scheiner, D.P. McMeekin, Z. Wang, N. Li, M.S. Killian, H. Chen, M. Richter, I. Levchuk, N. Schrenker, E. Spiecker, T. Stubhan, N.A. Luechinger, A. Hirsch, P. Schmuki, H.P. Steinrück, R.H. Fink, M. Halik, H.J. Snaith, C.J. Brabec, A generic interface to reduce the efficiency-stability-cost gap of perovskite solar cells, Science. 358 (2017) 1192–1197. doi:10.1126/science.aao5561.

[129] H. Cho, S.H. Jeong, M.H. Park, Y.H. Kim, C. Wolf, C.L. Lee, J.H. Heo, A. Sadhanala, N.S. Myoung, S. Yoo, S.H. Im, R.H. Friend, T.W. Lee, Overcoming the electroluminescence efficiency limitations of perovskite light-emitting diodes, Science. (2015). doi:10.1126/science.aad1818.

[130] D.A. Egger, A.M. Rappe, L. Kronik, Hybrid Organic-Inorganic Perovskites on the Move, Acc. Chem. Res. (2016). doi:10.1021/acs.accounts.5b00540.

[131] J. Berry, T. Buonassisi, D.A. Egger, G. Hodes, L. Kronik, Y.L. Loo, I. Lubomirsky, S.R. Marder, Y. Mastai, J.S. Miller, D.B. Mitzi, Y. Paz, A.M. Rappe, I. Riess, B. Rybtchinski, O. Stafsudd, V. Stevanovic, M.F. Toney, D. Zitoun, A. Kahn, D. Ginley, D. Cahen, Hybrid Organic-Inorganic Perovskites (HOIPs): Opportunities and Challenges, Adv. Mater. (2015). doi:10.1002/adma.201502294.

[132] C.C. Stoumpos, M.G. Kanatzidis, Halide Perovskites: Poor Man's High-Performance Semiconductors, Adv. Mater. (2016). doi:10.1002/adma.201600265.

[133] X. Li, M. Tschumi, H. Han, S.S. Babkair, R.A. Alzubaydi, A.A. Ansari, S.S. Habib, M.K. Nazeeruddin, S.M. Zakeeruddin, M. Grätzel, Outdoor Performance and

Stability under Elevated Temperatures and Long-Term Light Soaking of Triple-Layer Mesoporous Perovskite Photovoltaics, Energy Technol. (2015). doi:10.1002/ente.201500045.

[134] W.S. Yang, J.H. Noh, N.J. Jeon, Y.C. Kim, S. Ryu, J. Seo, S. Il Seok, High-performance photovoltaic perovskite layers fabricated through intramolecular exchange, Science. 348 (2015) 1234–1237. doi:10.1126/science.aaa9272.

[135] Z. Li, M. Yang, J.S. Park, S.H. Wei, J.J. Berry, K. Zhu, Stabilizing Perovskite Structures by Tuning Tolerance Factor: Formation of Formamidinium and Cesium Lead Iodide Solid-State Alloys, Chem. Mater. (2016). doi:10.1021/acs.chemmater.5b04107.

[136] A. Mancini, P. Quadrelli, C. Milanese, M. Patrini, G. Guizzetti, L. Malavasi, CH3NH3SnxPb1-xBr3 Hybrid Perovskite Solid Solution: Synthesis, Structure, and Optical Properties., Inorg. Chem. (2015). doi:10.1021/acs.inorgchem.5b01843.

[137] M.A. Peña, J.L.G. Fierro, Chemical structures and performance of perovskite oxides, Chem. Rev. (2001). doi:10.1021/cr980129f.

[138] N.K. Noel, S.D. Stranks, A. Abate, C. Wehrenfennig, S. Guarnera, A.A. Haghighirad, A. Sadhanala, G.E. Eperon, S.K. Pathak, M.B. Johnston, A. Petrozza, L.M. Herz, H.J. Snaith, Lead-free organic-inorganic tin halide perovskites for photovoltaic applications, Energy Environ. Sci. (2014). doi:10.1039/c4ee01076k.

[139] B.W. Park, B. Philippe, X. Zhang, H. Rensmo, G. Boschloo, E.M.J. Johansson, Bismuth Based Hybrid Perovskites A3Bi2I9 (A: Methylammonium or Cesium) for Solar Cell Application, Adv. Mater. (2015). doi:10.1002/adma.201501978.

[140] R.L.Z. Hoye, R.E. Brandt, A. Osherov, V. Stevanovic, S.D. Stranks, M.W.B. Wilson, H. Kim, A.J. Akey, J.D. Perkins, R.C. Kurchin, J.R. Poindexter, E.N. Wang, M.G. Bawendi, V. Bulovic, T. Buonassisi, Methylammonium Bismuth Iodide as a Lead-Free, Stable Hybrid Organic-Inorganic Solar Absorber, Chem. - A Eur. J. (2016). doi:10.1002/chem.201505055.

[141] S.A.U. Hasan, D.S. Lee, S.H. Im, K.-H. Hong, Present Status and Research Prospects of Tin□based Perovskite Solar Cells, Sol. RRL. 4 (2020) 1900310. doi:10.1002/solr.201900310.

[142] F. Hao, C.C. Stoumpos, R.P.H. Chang, M.G. Kanatzidis, Anomalous band gap behavior in mixed Sn and Pb perovskites enables broadening of absorption spectrum in solar cells, J. Am. Chem. Soc. (2014). doi:10.1021/ja5033259.

[143] W. Ming, H. Shi, M.H. Du, Large dielectric constant, high acceptor density, and deep electron traps in perovskite solar cell material CsGeI3, J. Mater. Chem. A.

(2016). doi:10.1039/c6ta04685a.

[144] C.C. Stoumpos, L. Frazer, D.J. Clark, Y.S. Kim, S.H. Rhim, A.J. Freeman, J.B. Ketterson, J.I. Jang, M.G. Kanatzidis, Hybrid germanium iodide perovskite semiconductors: Active lone pairs, structural distortions, direct and indirect energy gaps, and strong nonlinear optical properties, J. Am. Chem. Soc. (2015). doi:10.1021/jacs.5b01025.

[145] J. Navas, A. Sánchez-Coronilla, J.J. Gallardo, N. Cruz Hernández, J.C. Piñero, R. Alcántara, C. Fernández-Lorenzo, D.M. De Los Santos, T. Aguilar, J. Martín-Calleja, New insights into organic-inorganic hybrid perovskite CH3NH3PbI3 nanoparticles. An experimental and theoretical study of doping in Pb2+ sites with Sn2+, Sr2+, Cd2+ and Ca2+, Nanoscale. (2015). doi:10.1039/c5nr00041f.

[146] E.P. Yao, P. Sun, W. Huang, E.P. Yao, Y. Yang, M. Wang, Efficient planar perovskite solar cells using halide Sr-substituted Pb perovskite, Nano Energy. (2017). doi:10.1016/j.nanoen.2017.04.047.

[147] B. Philippe, B.W. Park, R. Lindblad, J. Oscarsson, S. Ahmadi, E.M.J. Johansson, H. Rensmo, Chemical and electronic structure characterization of lead halide perovskites and stability behavior under different exposures-A photoelectron spectroscopy investigation, Chem. Mater. 27 (2015) 1720–1731. doi:10.1021/acs.chemmater.5b00348.

[148] A.S. Yerramilli, Y. Chen, D. Sanni, J. Asare, N.D. Theodore, T.L. Alford, Impact of excess lead on the stability and photo-induced degradation of lead halide perovskite solar cells, Org. Electron. Physics, Mater. Appl. (2018). doi:10.1016/j.orgel.2018.04.052.

[149] G. Tumen□Ulzii, C. Qin, D. Klotz, M.R. Leyden, P. Wang, M. Auffray, T. Fujihara, T. Matsushima, J. Lee, S. Lee, Y. Yang, C. Adachi, Detrimental Effect of Unreacted PbI_2 on the Long□Term Stability of Perovskite Solar Cells, Adv. Mater. 32 (2020) 1905035. doi:10.1002/adma.201905035.

[150] T.M. Koh, V. Shanmugam, J. Schlipf, L. Oesinghaus, P. Müller-Buschbaum, N. Ramakrishnan, V. Swamy, N. Mathews, P.P. Boix, S.G. Mhaisalkar, Nanostructuring Mixed-Dimensional Perovskites: A Route Toward Tunable, Efficient Photovoltaics, Adv. Mater. 28 (2016) 3653–3661. doi:10.1002/adma.201506141.

[151] H. Tsai, W. Nie, J.C. Blancon, C.C. Stoumpos, R. Asadpour, B. Harutyunyan, A.J. Neukirch, R. Verduzco, J.J. Crochet, S. Tretiak, L. Pedesseau, J. Even, M.A. Alam, G. Gupta, J. Lou, P.M. Ajayan, M.J. Bedzyk, M.G. Kanatzidis, A.D. Mohite, High-efficiency two-dimensional ruddlesden-popper perovskite solar cells, Nature. 536 (2016) 312–317. doi:10.1038/nature18306.

[152] F. Arabpour Roghabadi, M. Alidaei, S.M. Mousavi, T. Ashjari, A.S. Tehrani, V. Ahmadi, S.M. Sadrameli, Stability progress of perovskite solar cells dependent on the crystalline structure: From 3D ABX3 to 2D Ruddlesden-Popper perovskite absorbers, J. Mater. Chem. A. 7 (2019) 5898–5933. doi:10.1039/c8ta10444a.

[153] T. Wang, Q. Tai, X. Guo, J. Cao, C.K. Liu, N. Wang, D. Shen, Y. Zhu, C.S. Lee, F. Yan, Highly Air-Stable Tin-Based Perovskite Solar Cells through Grain-Surface Protection by Gallic Acid, ACS Energy Lett. 5 (2020) 1741–1749. doi:10.1021/acsenergylett.0c00526.

[154] T. Rath, J. Handl, S. Weber, B. Friesenbichler, P. Fürk, L. Troi, T. Dimopoulos, B. Kunert, R. Resel, G. Trimmel, Photovoltaic properties of a triple-cation methylammonium/formamidinium/phenylethylammonium tin iodide perovskite, J. Mater. Chem. A. 7 (2019) 9523–9529. doi:10.1039/c9ta02835h.

[155] S. Adjokatse, S. Kahmann, H. Duim, M.A. Loi, Effects of strontium doping on the morphological, structural, and photophysical properties of FASnI3 perovskite thin films, APL Mater. 7 (2019). doi:10.1063/1.5087110.

[156] T.J. Jacobsson, M. Pazoki, A. Hagfeldt, T. Edvinsson, Goldschmidt's Rules and Strontium Replacement in Lead Halogen Perovskite Solar Cells: Theory and Preliminary Experiments on $CH_3NH_3SrI_3$, J. Phys. Chem. C. 119 (2015) 25673–25683. doi:10.1021/acs.jpcc.5b06436.

[157] H. Zhang, H. Wang, S.T. Williams, D. Xiong, W. Zhang, C.-C. Chueh, W. Chen, A.K.-Y. Jen, $SrCl_2$ Derived Perovskite Facilitating a High Efficiency of 16% in Hole-Conductor-Free Fully Printable Mesoscopic Perovskite Solar Cells, Adv. Mater. 29 (2017) 1606608. doi:10.1002/adma.201606608.

[158] M.L. Agiorgousis, Y.Y. Sun, H. Zeng, S. Zhang, Strong covalency-induced recombination centers in perovskite solar cell material CH3NH3PbI3, J. Am. Chem. Soc. 136 (2014) 14570–14575. doi:10.1021/ja5079305.

[159] W.J. Yin, T. Shi, Y. Yan, Unusual defect physics in CH3NH3PbI3 perovskite solar cell absorber, Appl. Phys. Lett. 104 (2014) 063903. doi:10.1063/1.4864778.

[160] R. Wang, M. Mujahid, Y. Duan, Z.-K. Wang, J. Xue, Y. Yang, A Review of Perovskites Solar Cell Stability, Adv. Funct. Mater. (2019) 1808843. doi:10.1002/adfm.201808843.

[161] M.A. Green, A. Ho-Baillie, Perovskite Solar Cells: The Birth of a New Era in Photovoltaics, ACS Energy Lett. (2017). doi:10.1021/acsenergylett.7b00137.

[162] D. Shi, V. Adinolfi, R. Comin, M. Yuan, E. Alarousu, A. Buin, Y. Chen, S. Hoogland, A. Rothenberger, K. Katsiev, Y. Losovyj, X. Zhang, P.A. Dowben, O.F. Mohammed, E.H. Sargent, O.M. Bakr, Low trap-state density and long carrier diffusion in organolead trihalide perovskite single crystals, Science. 347 (2015) 519–522. doi:10.1126/science.aaa2725.

[163] S. De Wolf, J. Holovsky, S.J. Moon, P. Löper, B. Niesen, M. Ledinsky, F.J. Haug, J.H. Yum, C. Ballif, Organometallic halide perovskites: Sharp optical absorption edge and its relation to photovoltaic performance, J. Phys. Chem. Lett. 5 (2014) 1035–1039. doi:10.1021/jz500279b.

[164] H.J. Snaith, A. Abate, J.M. Ball, G.E. Eperon, T. Leijtens, N.K. Noel, S.D. Stranks, J.T.-W. Wang, K. Wojciechowski, W. Zhang, Anomalous Hysteresis in Perovskite Solar Cells, J. Phys. Chem. Lett. 5 (2014) 1511–1515. doi:10.1021/jz500113x.

[165] Y. Zhao, K. Zhu, Organic-inorganic hybrid lead halide perovskites for optoelectronic and electronic applications, Chem. Soc. Rev. 45 (2016) 655–689. doi:10.1039/c4cs00458b.

[166] C. Liu, W. Li, C. Zhang, Y. Ma, J. Fan, Y. Mai, All-Inorganic $CsPbI_2Br$ Perovskite Solar Cells with High Efficiency Exceeding 13%, J. Am. Chem. Soc. 140 (2018) 3825–3828. doi:10.1021/jacs.7b13229.

[167] J. Liang, C. Wang, Y. Wang, Z. Xu, Z. Lu, Y. Ma, H. Zhu, Y. Hu, C. Xiao, X. Yi, G. Zhu, H. Lv, L. Ma, T. Chen, Z. Tie, Z. Jin, J. Liu, All-Inorganic Perovskite Solar Cells, J. Am. Chem. Soc. 138 (2016) 15829–15832. doi:10.1021/jacs.6b10227.

[168] T. Leijtens, T. Giovenzana, S.N. Habisreutinger, J.S. Tinkham, N.K. Noel, B.A. Kamino, G. Sadoughi, A. Sellinger, H.J. Snaith, Hydrophobic Organic Hole Transporters for Improved Moisture Resistance in Metal Halide Perovskite Solar Cells, ACS Appl. Mater. Interfaces. 8 (2016) 5981–5989. doi:10.1021/acsami.5b10093.

[169] Y. Bai, Q. Dong, Y. Shao, Y. Deng, Q. Wang, L. Shen, D. Wang, W. Wei, J. Huang, Enhancing stability and efficiency of perovskite solar cells with crosslinkable silane-functionalized and doped fullerene, Nat. Commun. 7 (2016). doi:10.1038/ncomms12806.

[170] H.C. Weerasinghe, Y. Dkhissi, A.D. Scully, R.A. Caruso, Y.B. Cheng, Encapsulation for improving the lifetime of flexible perovskite solar cells, Nano Energy. 18 (2015) 118–125. doi:10.1016/j.nanoen.2015.10.006.

[171] Q. Tai, K.C. Tang, F. Yan, Recent progress of inorganic perovskite solar cells, Energy Environ. Sci. 12 (2019) 2375–2405. doi:10.1039/c9ee01479a.

[172] J. Ding, J. Duan, C. Guo, Q. Tang, Toward charge extraction in all-inorganic perovskite solar cells by interfacial engineering, J. Mater. Chem. A. 6 (2018) 21999–22004. doi:10.1039/C8TA02522C.

[173] J.C. Blancon, H. Tsai, W. Nie, C.C. Stoumpos, L. Pedesseau, C. Katan, M. Kepenekian, C.M.M. Soe, K. Appavoo, M.Y. Sfeir, S. Tretiak, P.M. Ajayan, M.G. Kanatzidis, J. Even, J.J. Crochet, A.D. Mohite, Extremely efficient internal exciton dissociation through edge states in layered 2D perovskites, Science (80-.). 355 (2017) 1288–1292. doi:10.1126/science.aal4211.

[174] Q. Dong, Y. Fang, Y. Shao, P. Mulligan, J. Qiu, L. Cao, J. Huang, Solar cells. Electron-hole diffusion lengths >175 μm in solution-grown CH3NH3PbI3 single crystals., Science. 347 (2015) 967–70. doi:10.1126/science.aaa5760.

[175] Z. Wang, Q. Lin, F.P. Chmiel, N. Sakai, L.M. Herz, H.J. Snaith, Efficient ambient-air-stable solar cells with 2D-3D heterostructured butylammonium-caesium-formamidinium lead halide perovskites, Nat. Energy. (2017). doi:10.1038/nenergy.2017.135.

[176] T. Zhang, L. Xie, L. Chen, N. Guo, G. Li, Z. Tian, B. Mao, Y. Zhao, In Situ Fabrication of Highly Luminescent Bifunctional Amino Acid Crosslinked 2D/3D $NH_3C_4H_9COO(CH_3NH_3PbBr_3)_n$ Perovskite Films, Adv. Funct. Mater. 27 (2017) 1603568. doi:10.1002/adfm.201603568.

[177] J.W. Lee, Z. Dai, T.H. Han, C. Choi, S.Y. Chang, S.J. Lee, N. De Marco, H. Zhao, P. Sun, Y. Huang, Y. Yang, 2D perovskite stabilized phase-pure formamidinium perovskite solar cells, Nat. Commun. 9 (2018). doi:10.1038/s41467-018-05454-4.

[178] N. Li, Z. Zhu, C.C. Chueh, H. Liu, B. Peng, A. Petrone, X. Li, L. Wang, A.K.Y. Jen, Mixed Cation FA x PEA 1–x PbI 3 with Enhanced Phase and Ambient Stability toward High-Performance Perovskite Solar Cells, Adv. Energy Mater. (2017). doi:10.1002/aenm.201601307.

[179] K. Yao, X. Wang, F. Li, L. Zhou, Mixed perovskite based on methyl-ammonium and polymeric-ammonium for stable and reproducible solar cells, Chem. Commun. 51 (2015) 15430–15433. doi:10.1039/c5cc05879a.

[180] B.-E. Cohen, M. Wierzbowska, L. Etgar, High Efficiency and High Open Circuit Voltage in Quasi 2D Perovskite Based Solar Cells, Adv. Funct. Mater. 27 (2017) 1604733. doi:10.1002/adfm.201604733.

[181] L.N. Quan, M. Yuan, R. Comin, O. Voznyy, E.M. Beauregard, S. Hoogland, A. Buin, A.R. Kirmani, K. Zhao, A. Amassian, D.H. Kim, E.H. Sargent, Ligand-Stabilized Reduced-Dimensionality Perovskites, J. Am. Chem. Soc. 138 (2016) 2649–2655. doi:10.1021/jacs.5b11740.

[182] D. Bi, P. Gao, R. Scopelliti, E. Oveisi, J. Luo, M. Grätzel, A. Hagfeldt, M.K. Nazeeruddin, High-Performance Perovskite Solar Cells with Enhanced Environmental Stability Based on Amphiphile-Modified $CH_3NH_3PbI_3$, Adv. Mater. 28 (2016) 2910–2915. doi:10.1002/adma.201505255.

[183] I.C. Smith, E.T. Hoke, D. Solis-Ibarra, M.D. McGehee, H.I. Karunadasa, A Layered Hybrid Perovskite Solar-Cell Absorber with Enhanced Moisture Stability, Angew. Chemie. 126 (2014) 11414–11417. doi:10.1002/ange.201406466.

[184] Q. Jiang, D. Rebollar, J. Gong, E.L. Piacentino, C. Zheng, T. Xu, Pseudohalide-Induced Moisture Tolerance in Perovskite $CH_3NH_3Pb(SCN)_2I$ Thin Films, Angew. Chemie. 127 (2015) 7727–7730. doi:10.1002/ange.201503038.

[185] T.C. Jellicoe, J.M. Richter, H.F.J. Glass, M. Tabachnyk, R. Brady, S.E. Dutton, A. Rao, R.H. Friend, D. Credgington, N.C. Greenham, M.L. Böhm, Synthesis and Optical Properties of Lead-Free Cesium Tin Halide Perovskite Nanocrystals, J. Am. Chem. Soc. 138 (2016) 2941–2944. doi:10.1021/jacs.5b13470.

[186] N. Li, Z. Zhu, C.-C. Chueh, H. Liu, B. Peng, A. Petrone, X. Li, L. Wang, A.K.-Y. Jen, Mixed Cation $FA_xPEA_{1-x}PbI_3$ with Enhanced Phase and Ambient Stability toward High-Performance Perovskite Solar Cells, Adv. Energy Mater. 7 (2017) 1601307. doi:10.1002/aenm.201601307.

[187] J.F. Liao, H.S. Rao, B.X. Chen, D. Bin Kuang, C.Y. Su, Dimension engineering on cesium lead iodide for efficient and stable perovskite solar cells, J. Mater. Chem. A. 5 (2017) 2066–2072. doi:10.1039/c6ta09582h.

[188] D.S. Lee, J.S. Yun, J. Kim, A.M. Soufiani, S. Chen, Y. Cho, X. Deng, J. Seidel, S. Lim, S. Huang, A.W.Y. Ho-Baillie, Passivation of Grain Boundaries by Phenethylammonium in Formamidinium-Methylammonium Lead Halide Perovskite Solar Cells, ACS Energy Lett. 3 (2018) 647–654. doi:10.1021/acsenergylett.8b00121.

[189] W. Zhang, J. Xiong, J. Li, W.A. Daoud, Guanidinium induced phase separated perovskite layer for efficient and highly stable solar cells, J. Mater. Chem. A. 7 (2019) 9486–9496. doi:10.1039/c9ta01893j.

[190] J.W. Jo, M.S. Seo, M. Park, J.Y. Kim, J.S. Park, I.K. Han, H. Ahn, J.W. Jung, B.H. Sohn, M.J. Ko, H.J. Son, Improving Performance and Stability of Flexible Planar-Heterojunction Perovskite Solar Cells Using Polymeric Hole-Transport Material, Adv. Funct. Mater. 26 (2016) 4464–4471. doi:10.1002/adfm.201600746.

[191] J.H. Heo, H.J. Han, D. Kim, T.K. Ahn, S.H. Im, Hysteresis-less inverted CH3NH3PbI3 planar perovskite hybrid solar cells with 18.1% power conversion efficiency, Energy Environ. Sci. 8 (2015) 1602–1608. doi:10.1039/c5ee00120j.

[192] E. Halvani Anaraki, A. Kermanpur, M.T. Mayer, L. Steier, T. Ahmed, S.H. Turren-Cruz, J. Seo, J. Luo, S.M. Zakeeruddin, W.R. Tress, T. Edvinsson, M. Grätzel, A. Hagfeldt, J.P. Correa-Baena, Low-Temperature Nb-Doped SnO2 Electron-Selective Contact Yields over 20% Efficiency in Planar Perovskite Solar Cells, ACS Energy Lett. 3 (2018) 773–778. doi:10.1021/acsenergylett.8b00055.

[193] J.H. Lee, J.H. Heo, S.H. Im, O.O. Park, Reproducible Dry Stamping Transfer of PEDOT:PSS Transparent Top Electrode for Flexible Semitransparent Metal Halide Perovskite Solar Cells, ACS Appl. Mater. Interfaces. 12 (2020) 10527–10534. doi:10.1021/acsami.9b22657.

[194] K. Sun, J. Chang, F.H. Isikgor, P. Li, J. Ouyang, Efficiency enhancement of planar perovskite solar cells by adding zwitterion/LiF double interlayers for electron collection, Nanoscale. 7 (2015) 896–900. doi:10.1039/c4nr05975a.

[195] F. Wu, P. Li, K. Sun, Y. Zhou, W. Chen, J. Fu, M. Li, S. Lu, D. Wei, X. Tang, Z. Zang, L. Sun, X. Liu, J. Ouyang, Conductivity Enhancement of PEDOT:PSS via Addition of Chloroplatinic Acid and Its Mechanism, Adv. Electron. Mater. 3 (2017) 1700047. doi:10.1002/aelm.201700047.

[196] C.-H. Chiang, Z.-L. Tseng, C.-G. Wu, Planar heterojunction perovskite/PC $_{71}$ BM solar cells with enhanced open-circuit voltage via a (2/1)-step spin-coating process, J. Mater. Chem. A. 2 (2014) 15897–15903. doi:10.1039/C4TA03674C.

[197] C. Ma, C. Leng, Y. Ji, X. Wei, K. Sun, L. Tang, J. Yang, W. Luo, C. Li, Y. Deng, S. Feng, J. Shen, S. Lu, C. Du, H. Shi, 2D/3D perovskite hybrids as moisture-tolerant and efficient light absorbers for solar cells, Nanoscale. 8 (2016) 18309–18314. doi:10.1039/c6nr04741f.

[198] L. Ji, X. Zhang, T. Zhang, Y. Wang, F. Wang, Z. Zhong, Z.D. Chen, Z. Xiao, L. Chen, S. Li, Band alignment of Pb-Sn mixed triple-cation perovskites for inverted solar cells with negligible hysteresis, J. Mater. Chem. A. 7 (2019) 9154–9162. doi:10.1039/c8ta11891d.

[199] Y. Kang, S. Kwon, S. Cho, Y. Seo, M. Choi, S. Kim, S. Na, J. Accepted, Antisolvent additive engineering containing dual- function additive for triple-cation p-i-n perovskite solar cells with over 20 % PCE, ACS Energy Lett. 2020 (2020). doi:10.1021/acsenergylett.0c01130.

[200] M. Afzaal, H.M. Yates, A. Walter, S. Nicolay, Improved FTO/NiOx Interfaces for Inverted Planar Triple-Cation Perovskite Solar Cells, IEEE J. Photovoltaics. 9 (2019) 1302–1308. doi:10.1109/JPHOTOV.2019.2927927.

[201] W. Zhang, J. Xiong, L. Jiang, J. Wang, T. Mei, X. Wang, H. Gu, W.A. Daoud, J. Li, Thermal Stability-Enhanced and High-Efficiency Planar Perovskite Solar Cells with

Interface Passivation, ACS Appl. Mater. Interfaces. 9 (2017) 38467–38476. doi:10.1021/acsami.7b10994.

[202] D.Y. Son, J.W. Lee, Y.J. Choi, I.H. Jang, S. Lee, P.J. Yoo, H. Shin, N. Ahn, M. Choi, D. Kim, N.G. Park, Self-formed grain boundary healing layer for highly efficient CH3 NH3 PbI3 perovskite solar cells, Nat. Energy. 1 (2016) 1–8. doi:10.1038/nenergy.2016.81.

[203] W.J. Yin, T. Shi, Y. Yan, Unusual defect physics in CH3NH3PbI3 perovskite solar cell absorber, Appl. Phys. Lett. 104 (2014) 063903. doi:10.1063/1.4864778.

[204] J. Yang, X. Liu, Y. Zhang, X. Zheng, X. He, H. Wang, F. Yue, S. Braun, J. Chen, J. Xu, Y. Li, Y. Jin, J. Tang, C. Duan, M. Fahlman, Q. Bao, Comprehensive understanding of heat-induced degradation of triple-cation mixed halide perovskite for a robust solar cell, Nano Energy. 54 (2018) 218–226. doi:10.1016/j.nanoen.2018.10.011.

[205] Y.-H. Seo, J.H. Kim, D.-H. Kim, H.-S. Chung, S.-I. Na, In situ TEM observation of the heat–induced degradation of single– and triple–cation planar perovskite solar cells, Nano Energy. (2020) 105164. doi:10.1016/j.nanoen.2020.105164.

[206] Q. Chen, N. De Marco, Y. Yang, T. Bin Song, C.C. Chen, H. Zhao, Z. Hong, H. Zhou, Y. Yang, Under the spotlight: The organic-inorganic hybrid halide perovskite for optoelectronic applications, Nano Today. 10 (2015) 355–396. doi:10.1016/j.nantod.2015.04.009.

[207] J.H. Noh, S.H. Im, J.H. Heo, T.N. Mandal, S. Il Seok, Chemical Management for Colorful, Efficient, and Stable Inorganic–Organic Hybrid Nanostructured Solar Cells, Nano Lett. 13 (2013) 1764–1769. doi:10.1021/nl400349b.

[208] A. Miyata, A. Mitioglu, P. Plochocka, O. Portugall, J.T.-W. Wang, S.D. Stranks, H.J. Snaith, R.J. Nicholas, Direct Measurement of the Exciton Binding Energy and Effective Masses for Charge carriers in an Organic-Inorganic Tri-halide Perovskite, Nat. Phys. 11 (2015) 582–587. doi:10.1038/nphys3357.

[209] National Renewable Energy Laboratory Best Research Cell Efficiencies. https://www.nrel.gov/pv/assets/pdfs/best-research-cell-efficiencies.20190802.pdf (accessed February 13, 2020).

[210] W. Chen, H. Sun, Q. Hu, A.B. Djurišić, T.P. Russell, X. Guo, Z. He, High Short-Circuit Current Density via Integrating the Perovskite and Ternary Organic Bulk Heterojunction, ACS Energy Lett. 4 (2019) 2535–2536. doi:10.1021/acsenergylett.9b01964.

[211] G.-J.A.H. Wetzelaer, M. Scheepers, A.M. Sempere, C. Momblona, J. Ávila, H.J. Bolink, Trap-Assisted Non-Radiative Recombination in Organic-Inorganic Perovskite Solar Cells, Adv. Mater. 27 (2015) 1837–1841. doi:10.1002/adma.201405372.

[212] Q. Wang, Q. Dong, T. Li, A. Gruverman, J. Huang, Thin Insulating Tunneling Contacts for Efficient and Water-Resistant Perovskite Solar Cells, Adv. Mater. 28 (2016) 6734–6739. doi:10.1002/adma.201600969.

[213] J.S. Manser, M.I. Saidaminov, J.A. Christians, O.M. Bakr, P. V. Kamat, Making and Breaking of Lead Halide Perovskites, Acc. Chem. Res. 49 (2016) 330–338. doi:10.1021/acs.accounts.5b00455.

[214] D.W. DeQuilettes, S.M. Vorpahl, S.D. Stranks, H. Nagaoka, G.E. Eperon, M.E. Ziffer, H.J. Snaith, D.S. Ginger, Impact of microstructure on local carrier lifetime in perovskite solar cells, Science (80-.). 348 (2015) 683–686. doi:10.1126/science.aaa5333.

[215] A. Buin, P. Pietsch, J. Xu, O. Voznyy, A.H. Ip, R. Comin, E.H. Sargent, Materials processing routes to trap-free halide perovskites, Nano Lett. 14 (2014) 6281–6286. doi:10.1021/nl502612m.

[216] F. Wang, S. Bai, W. Tress, A. Hagfeldt, F. Gao, Defects engineering for high-performance perovskite solar cells, Npj Flex. Electron. 2 (2018) 22. doi:10.1038/s41528-018-0035-z.

[217] Q. Jiang, Y. Zhao, X. Zhang, X. Yang, Y. Chen, Z. Chu, Q. Ye, X. Li, Z. Yin, J. You, Surface passivation of perovskite film for efficient solar cells, Nat. Photonics. 13 (2019) 460–466. doi:10.1038/s41566-019-0398-2.

[218] X. Wu, Y. Jiang, C. Chen, J. Guo, X. Kong, Y. Feng, S. Wu, X. Gao, X. Lu, Q. Wang, G. Zhou, Y. Chen, J. Liu, K. Kempa, J. Gao, Stable Triple-cation Perovskite Precursor for Highly Efficient Perovskite Solar Cells Enabled by Interaction with 18C6 Stabilizer, Adv. Funct. Mater. 30 (2020) 1908613. doi:10.1002/adfm.201908613.

[219] X. Zheng, B. Chen, J. Dai, Y. Fang, Y. Bai, Y. Lin, H. Wei, X.C. Zeng, J. Huang, Defect passivation in hybrid perovskite solar cells using quaternary ammonium halide anions and cations, Nat. Energy. 2 (2017) 1–9. doi:10.1038/nenergy.2017.102.

[220] K. Yoshikawa, H. Kawasaki, W. Yoshida, T. Irie, K. Konishi, K. Nakano, T. Uto, D. Adachi, M. Kanematsu, H. Uzu, K. Yamamoto, Silicon heterojunction solar cell with interdigitated back contacts for a photoconversion efficiency over 26%, Nat. Energy. 2 (2017) 1–8. doi:10.1038/nenergy.2017.32.

[221] T. Zhao, C.C. Chueh, Q. Chen, A. Rajagopal, A.K.Y. Jen, Defect Passivation of Organic-Inorganic Hybrid Perovskites by Diammonium Iodide toward High-Performance Photovoltaic Devices, ACS Energy Lett. 1 (2016) 757–763. doi:10.1021/acsenergylett.6b00327.

[222] M. Abdi-Jalebi, Z. Andaji-Garmaroudi, S. Cacovich, C. Stavrakas, B. Philippe, J.M. Richter, M. Alsari, E.P. Booker, E.M. Hutter, A.J. Pearson, S. Lilliu, T.J. Savenije, H. Rensmo, G. Divitini, C. Ducati, R.H. Friend, S.D. Stranks, Maximizing and stabilizing luminescence from halide perovskites with potassium passivation, Nature. 555 (2018) 497–501. doi:10.1038/nature25989.

[223] A. Abate, M. Saliba, D.J. Hollman, S.D. Stranks, K. Wojciechowski, R. Avolio, G. Grancini, A. Petrozza, H.J. Snaith, Supramolecular halogen bond passivation of organic-inorganic halide perovskite solar cells, Nano Lett. 14 (2014) 3247–3254. doi:10.1021/nl500627x.

[224] A.S. Yerramilli, Y. Chen, D. Sanni, J. Asare, N.D. Theodore, T.L. Alford, Impact of excess lead on the stability and photo-induced degradation of lead halide perovskite solar cells, Org. Electron. Physics, Mater. Appl. 59 (2018). doi:10.1016/j.orgel.2018.04.052.

[225] D.M. Sanni, Y. Chen, A.S. Yerramilli, E. Ntsoenzok, J. Asare, S.A. Adeniji, O. V. Oyelade, A.A. Fashina, T.L. Alford, An approach to optimize pre-annealing aging and anneal conditions to improve photovoltaic performance of perovskite solar cells, Mater. Renew. Sustain. Energy. 8 (2019) 3. doi:10.1007/s40243-018-0139-3.

[226] H.M. Yu, H.M. Oh, D.Y. Park, M.S. Jeong, Nanochemical Investigation of Degradation in Organic–Inorganic Hybrid Perovskite Films Using Infrared Nanoscopy, J. Phys. Chem. C. 124 (2020) 3915–3922. doi:10.1021/acs.jpcc.0c00143.

[227] B. Roose, K. Dey, Y.-H. Chiang, R.H. Friend, S.D. Stranks, A Critical Assessment of the Use of Excess Lead Iodide in Lead Halide Perovskite Solar Cells, J. Phys. Chem. Lett. (2020) acs.jpclett.0c01820. doi:10.1021/acs.jpclett.0c01820.

[228] N. Li, Z. Zhu, Q. Dong, J. Li, Z. Yang, C.-C. Chueh, A.K.-Y. Jen, L. Wang, Enhanced Moisture Stability of Cesium-Containing Compositional Perovskites by a Feasible Interfacial Engineering, Adv. Mater. Interfaces. 4 (2017) 1700598. doi:10.1002/admi.201700598.

[229] Y. Xia, K. Sun, J. Chang, J. Ouyang, Effects of organic inorganic hybrid perovskite materials on the electronic properties and morphology of poly(3,4-ethylenedioxythiophene):poly(styrenesulfonate) and the photovoltaic performance of planar perovskite solar cells, J. Mater. Chem. A. 3 (2015) 15897–15904. doi:10.1039/c5ta03456f.

[230] L. Hu, M. Li, K. Yang, Z. Xiong, B. Yang, M. Wang, X. Tang, Z. Zang, X. Liu, B. Li, Z. Xiao, S. Lu, H. Gong, J. Ouyang, K. Sun, PEDOT:PSS monolayers to enhance the hole extraction and stability of perovskite solar cells, J. Mater. Chem. A. 6 (2018) 16583–16589. doi:10.1039/c8ta05234d.

[231] C.G. Wu, C.H. Chiang, Z.L. Tseng, M.K. Nazeeruddin, A. Hagfeldt, M. Grätzel, High efficiency stable inverted perovskite solar cells without current hysteresis, Energy Environ. Sci. 8 (2015) 2725–2733. doi:10.1039/c5ee00645g.

[232] H.L. Yip, A.K.Y. Jen, Recent advances in solution-processed interfacial materials for efficient and stable polymer solar cells, Energy Environ. Sci. 5 (2012) 5994–6011. doi:10.1039/c2ee02806a.

[233] K. Sun, P. Li, Y. Xia, J. Chang, J. Ouyang, Transparent Conductive Oxide-Free Perovskite Solar Cells with PEDOT:PSS as Transparent Electrode, ACS Appl. Mater. Interfaces. 7 (2015) 15314–15320. doi:10.1021/acsami.5b03171.

[234] L. Hu, K. Sun, M. Wang, W. Chen, B. Yang, J. Fu, Z. Xiong, X. Li, X. Tang, Z. Zang, S. Zhang, L. Sun, M. Li, Inverted Planar Perovskite Solar Cells with a High Fill Factor and Negligible Hysteresis by the Dual Effect of NaCl-Doped PEDOT:PSS, ACS Appl. Mater. Interfaces. 9 (2017) 43902–43909. doi:10.1021/acsami.7b14592.

[235] K.M. Reza, A. Gurung, B. Bahrami, S. Mabrouk, H. Elbohy, R. Pathak, K. Chen, A.H. Chowdhury, M.T. Rahman, S. Letourneau, H.C. Yang, G. Saianand, J.W. Elam, S.B. Darling, Q. Qiao, Tailored PEDOT:PSS hole transport layer for higher performance in perovskite solar cells: Enhancement of electrical and optical properties with improved morphology, J. Energy Chem. 44 (2020) 41–50. doi:10.1016/j.jechem.2019.09.014.

[236] Y. Wang, J. Wu, P. Zhang, D. Liu, T. Zhang, L. Ji, X. Gu, Z.D. Chen, S. Li, Stitching triple-cation perovskite by a mixed anti-solvent process for high performance perovskite solar cells, (2017). doi:10.1016/j.nanoen.2017.07.046.

[237] X. Guo, C. McCleese, C. Kolodziej, A.C.S. Samia, Y. Zhao, C. Burda, Identification and characterization of the intermediate phase in hybrid organic-inorganic MAPbI3 perovskite, Dalt. Trans. 45 (2016) 3806–3813. doi:10.1039/c5dt04420k.

[238] A.D. Jodlowski, C. Roldán-Carmona, G. Grancini, M. Salado, M. Ralaiarisoa, S. Ahmad, N. Koch, L. Camacho, G. De Miguel, M.K. Nazeeruddin, Large guanidinium cation mixed with methylammonium in lead iodide perovskites for 19% efficient solar cells, Nat. Energy. 2 (2017) 972–979. doi:10.1038/s41560-017-0054-3.

[239] N.K. Noel, A. Abate, S.D. Stranks, E.S. Parrott, V.M. Burlakov, A. Goriely, H.J. Snaith, Enhanced photoluminescence and solar cell performance via Lewis base passivation of organic-inorganic lead halide perovskites, ACS Nano. 8 (2014) 9815–9821. doi:10.1021/nn5036476.

APPENDIX A

SUPPORTING INFORMATION FOR CHAPTER 5

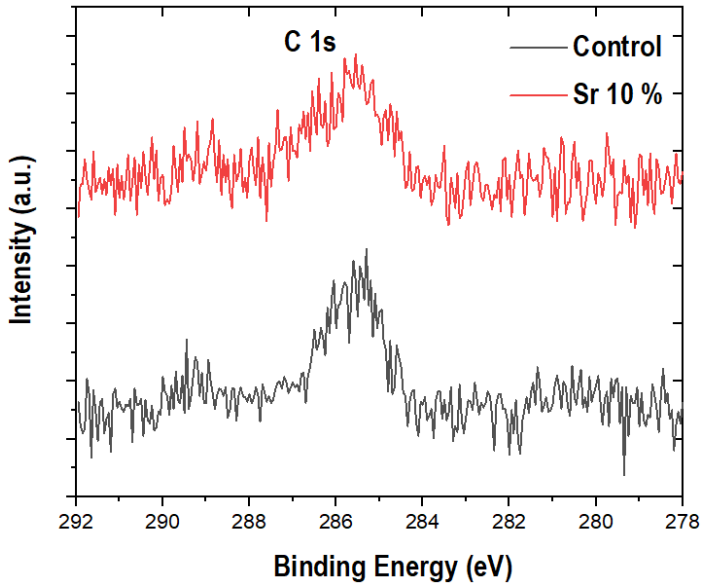

Fig. A1 XPS spectra of C 1*s* peaks in perovskite control and 10% Sr alloyed sample

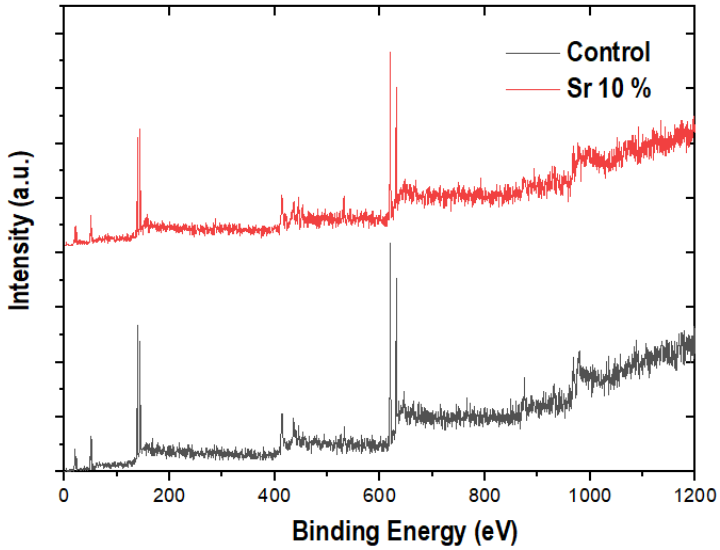

Fig. A2 Full XPS spectra of perovskite control and 10% Sr alloyed sample

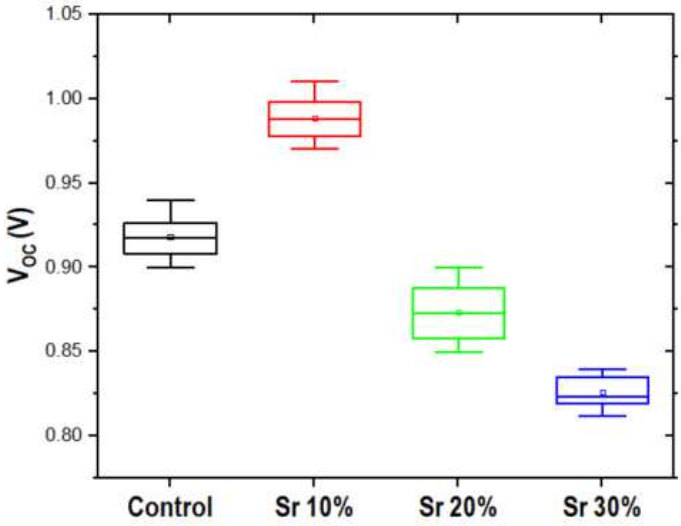

Fig. A3 Box plot for V_{OC} comparison of perovskite with different Sr alloying conditions

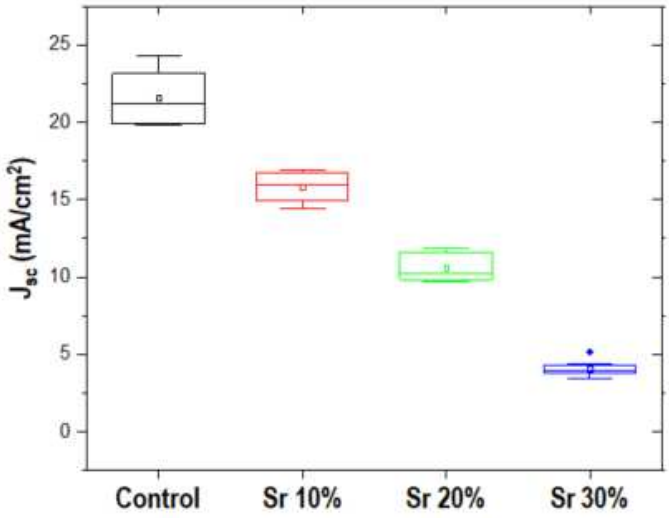

Fig. A4 Box plot for J_{SC} comparison of perovskite with different Sr alloying conditions

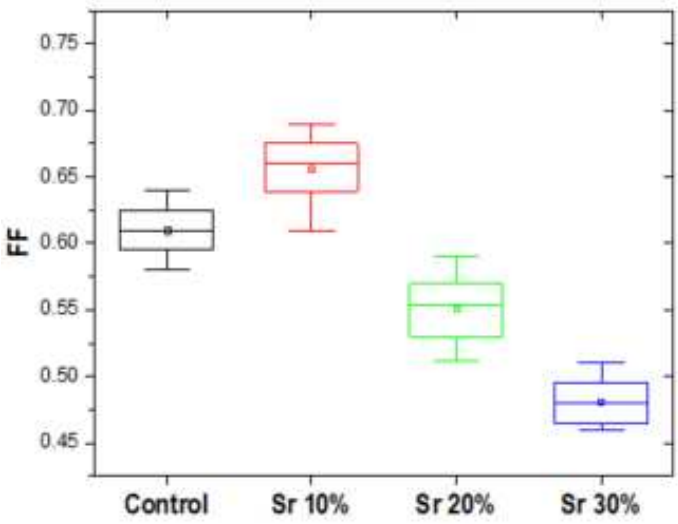

Fig. A5 Box plot for FF comparison of perovskite with different Sr alloying conditions

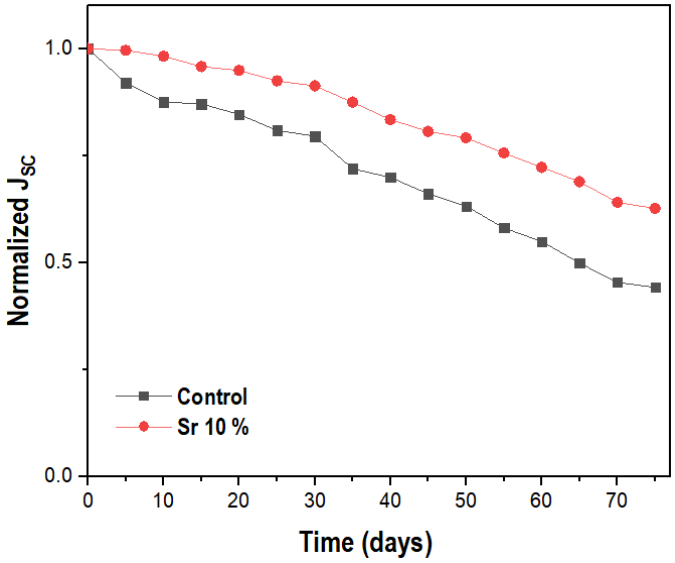

Fig. A6 Stability comparison of J_{SC} values of perovskite control and 10% Sr alloyed device

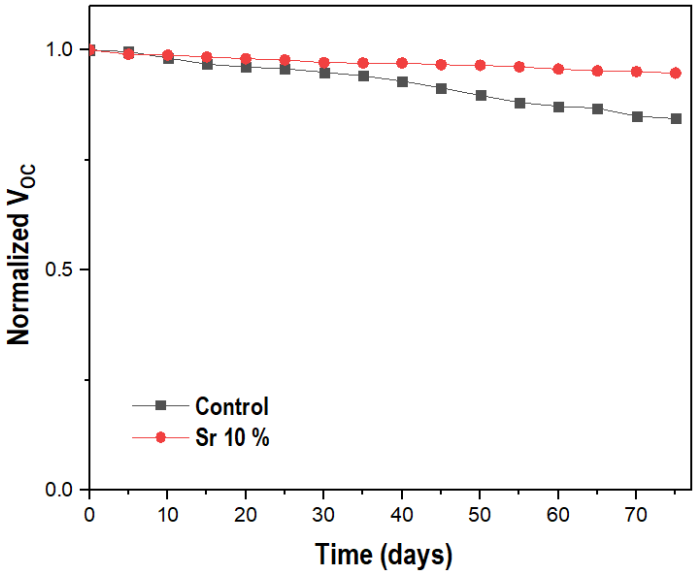

Fig. A7 Stability comparison of V_{OC} values of perovskite control and 10% Sr alloyed device

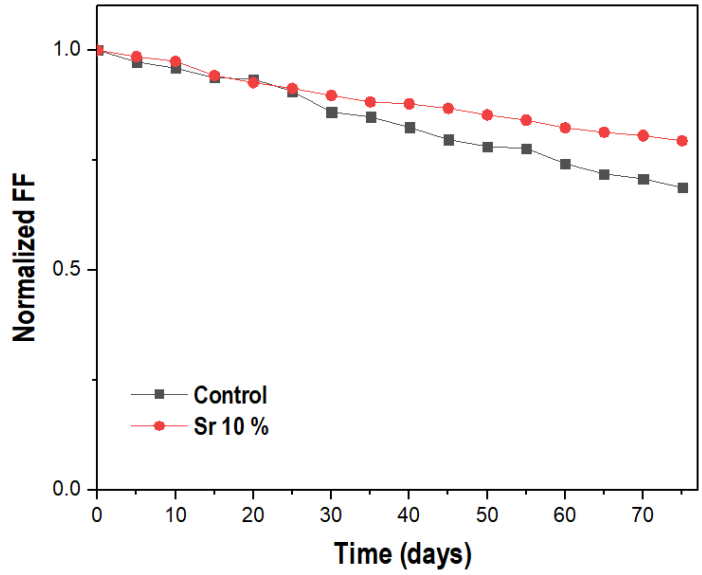

Fig. A8 Stability comparison of FF values of perovskite control and 10% Sr alloyed device

APPENDIX B

SUPPORTING INFORMATION FOR CHAPTER 6

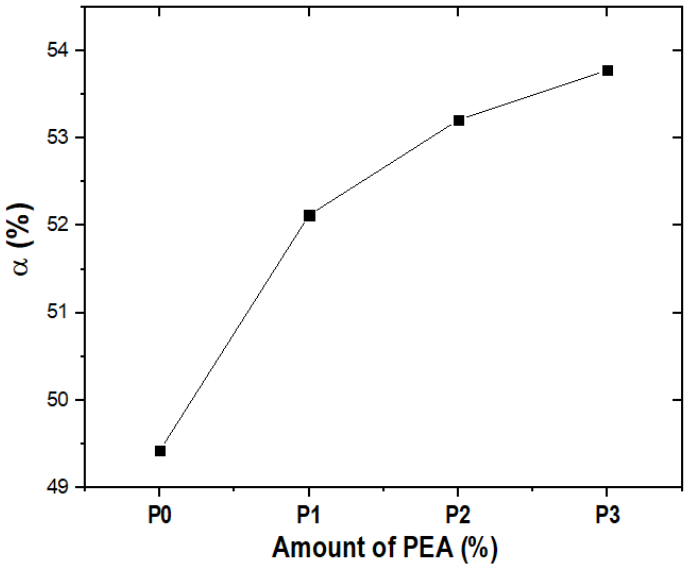

Fig. B1 Intensity ratio trend of perovskite with different PEA doping conditions

Table. B1 FWHM and α values of perovskite with different PEA doping conditions

Sample	FWHM	α (%)
P0	0.166	49.43
P1	0.156	52.12
P2	0.147	53.21
P3	0.142	53.78

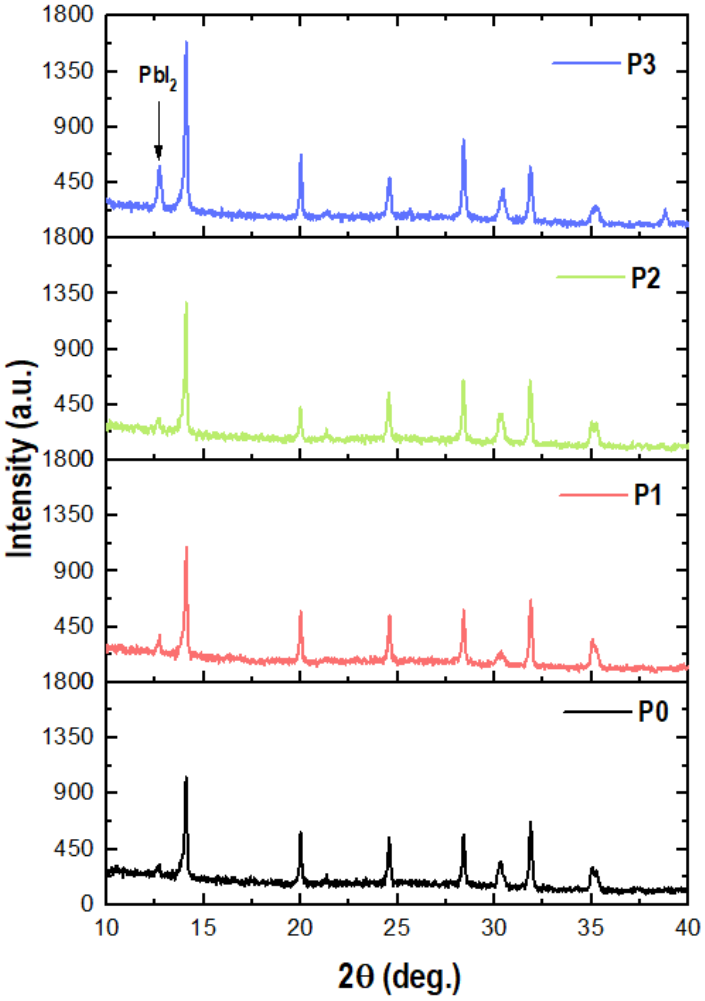

Fig. B2 XRD spectra of perovskite with different PEA doping conditions

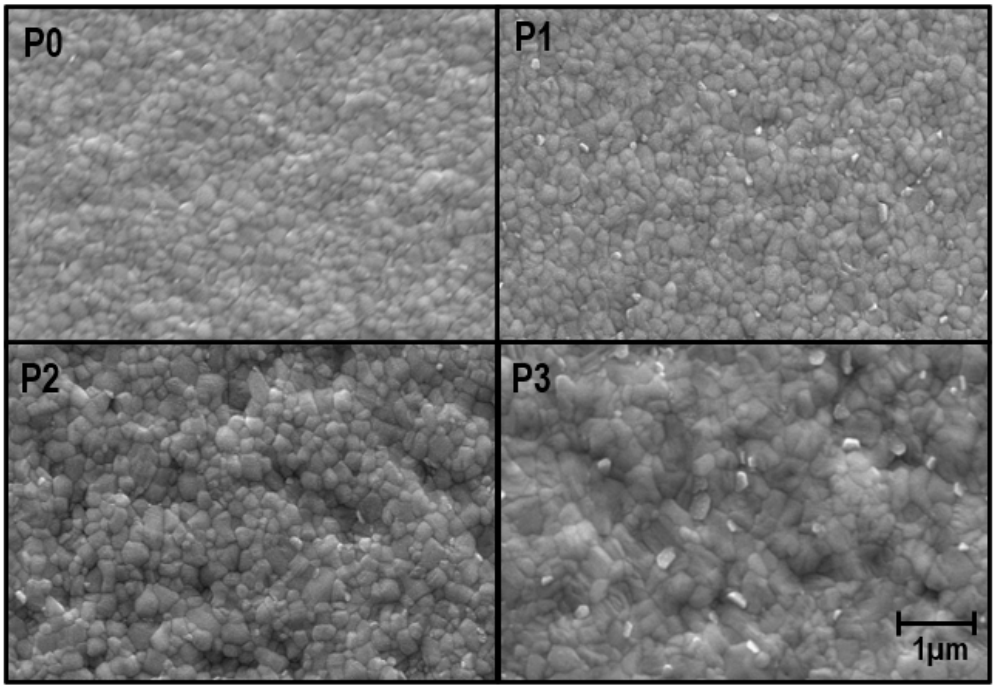

Fig. B3 SEM images of perovskite with different PEA doping conditions

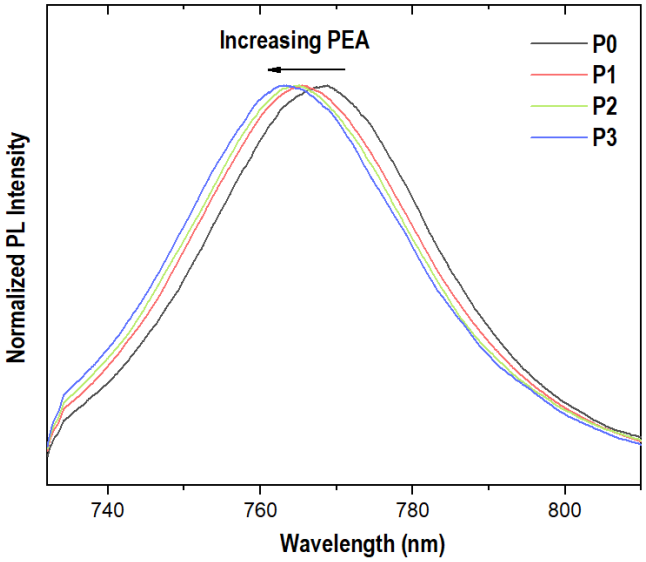

Fig. B4 Normalized PL intensity of perovskite with different PEA doping conditions

Table. B2 TRPL Fitting parameters of perovskite with different PEA doping conditions

Sample	τ_1(ns)	$\tau_{1\%}$	τ_2 (ns)	$\tau_{2\%}$	τ_{PL} (ns)
P0	58.27	40.31	144.07	59.68	122.39
P1	83.60	25.26	196.37	74.73	150.91
P2	65.23	30.64	157.34	69.35	129.11
P3	26.89	25.86	393.80	74.13	298.94

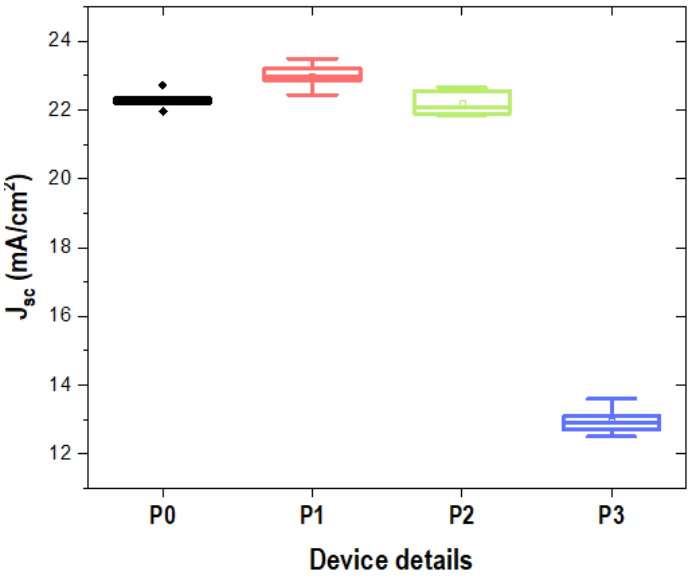

Fig. B5 Box plot of J_{SC} values of perovskite devices with different PEA doping conditions

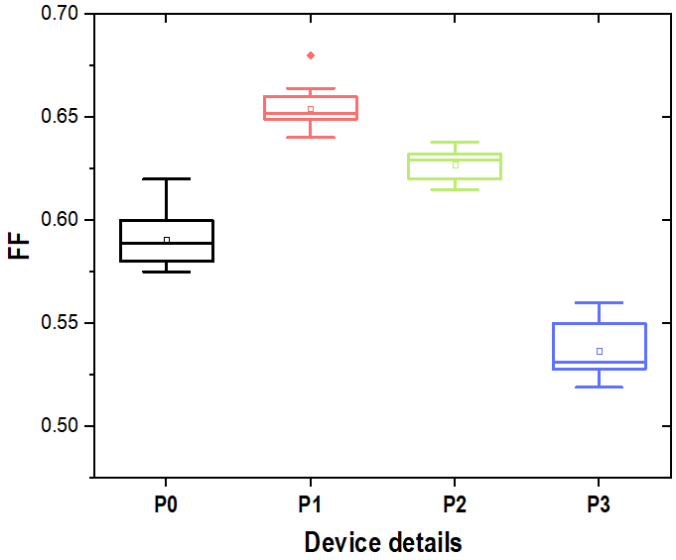

Fig. B6 Box plot of FF values of perovskite devices with different PEA doping conditions

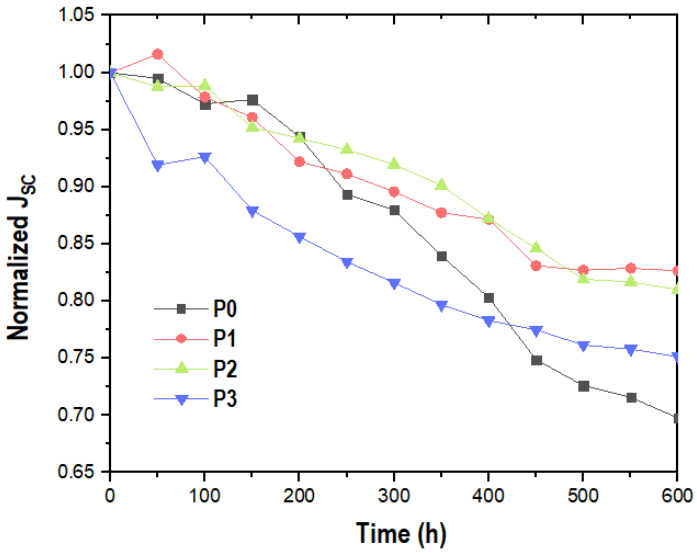

Fig. B7 J_{SC} degradation trend of perovskite devices with different PEA doping conditions

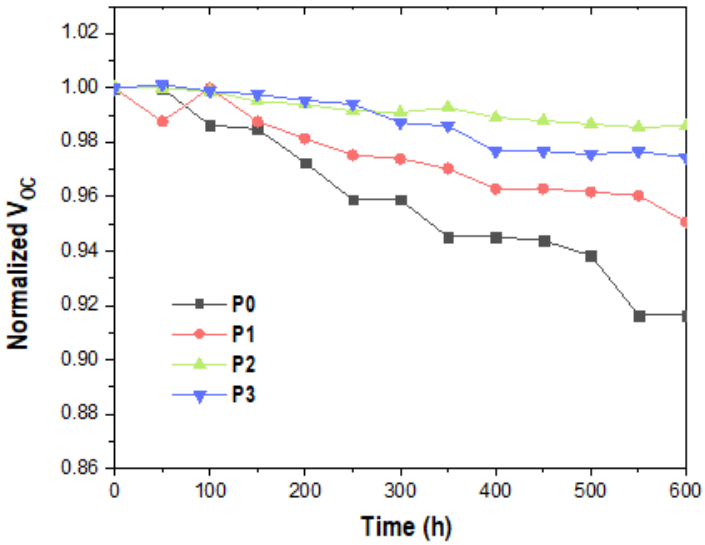

Fig. B8 V_{OC} degradation trend of perovskite devices with different PEA doping conditions

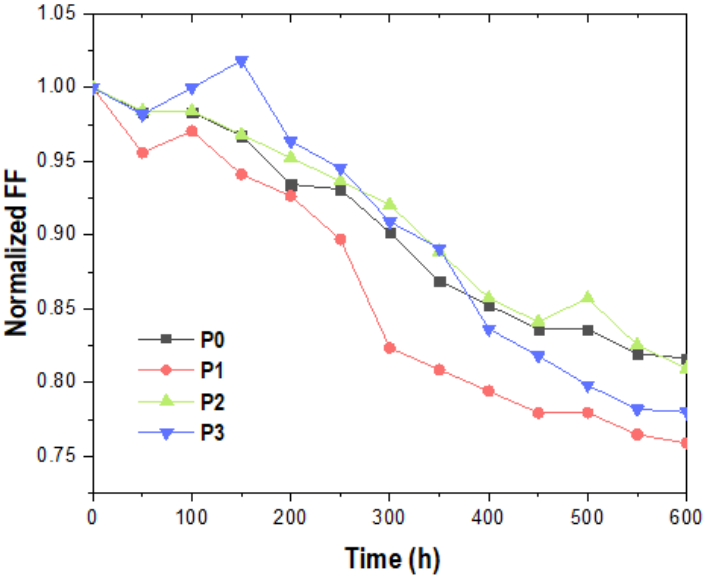

Fig. B9 FF degradation trend of perovskite devices with different PEA doping conditions

APPENDIX C

SUPPORTING INFORMATION FOR CHAPTER 7

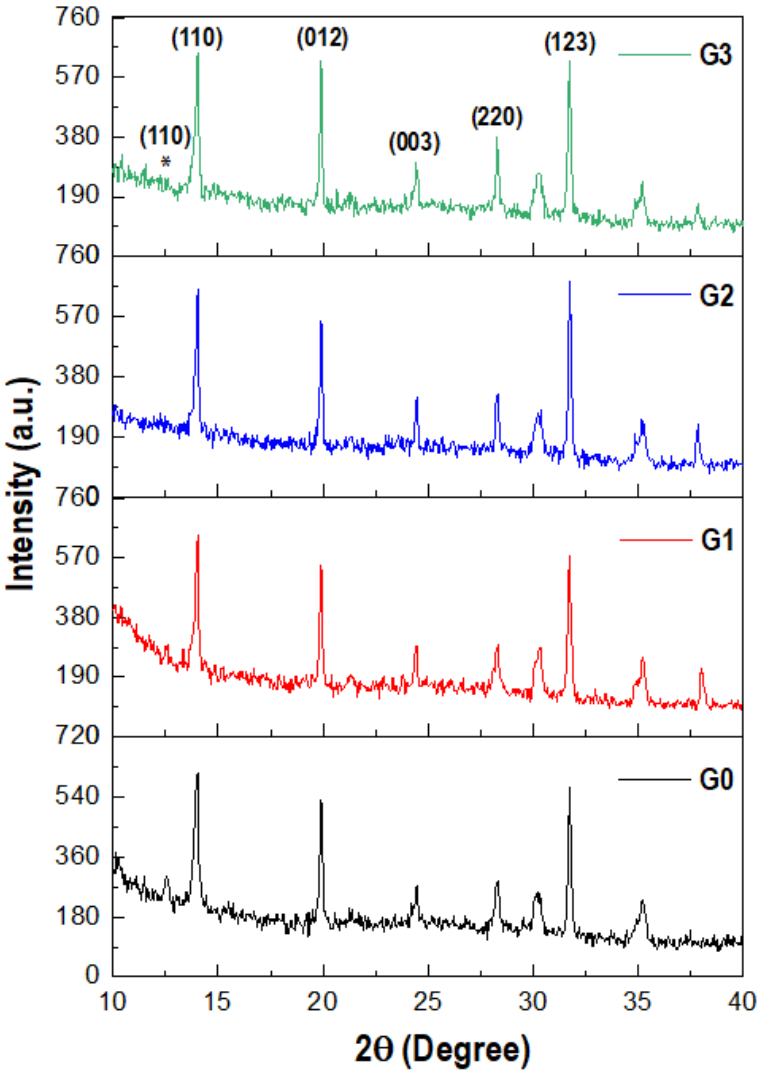

Fig. C1 XRD spectra of perovskite with different GUAI loading conditions prepared on ITO/glass (* represents PbI_2)

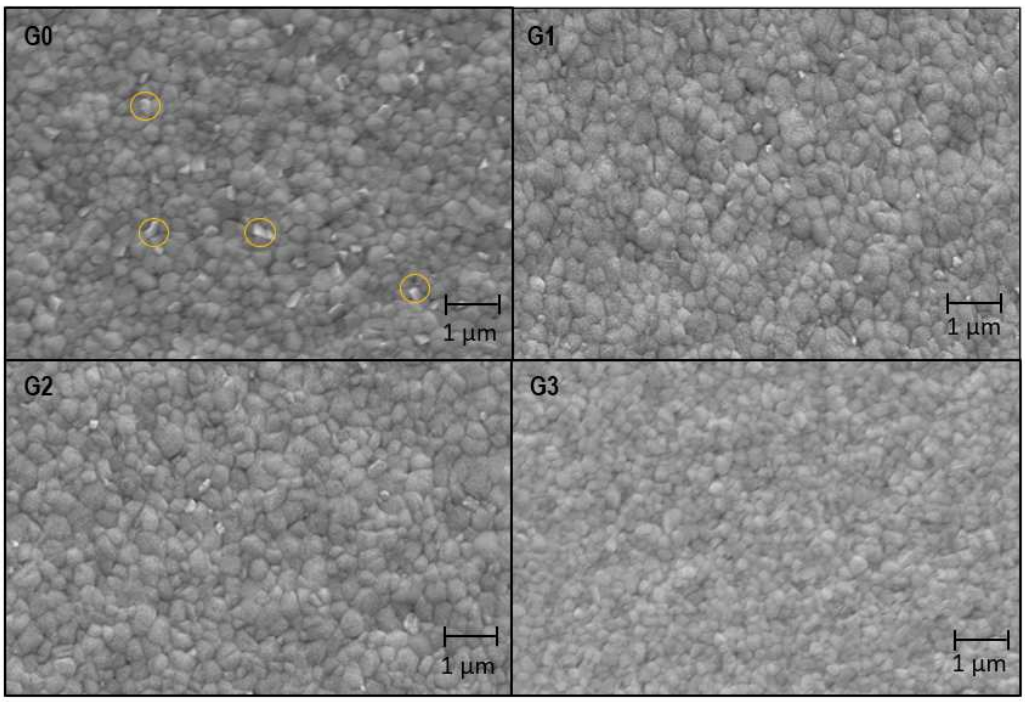

Fig. C2 SEM images of perovskite with different GUAI loading conditions prepared on an ITO/glass substrate

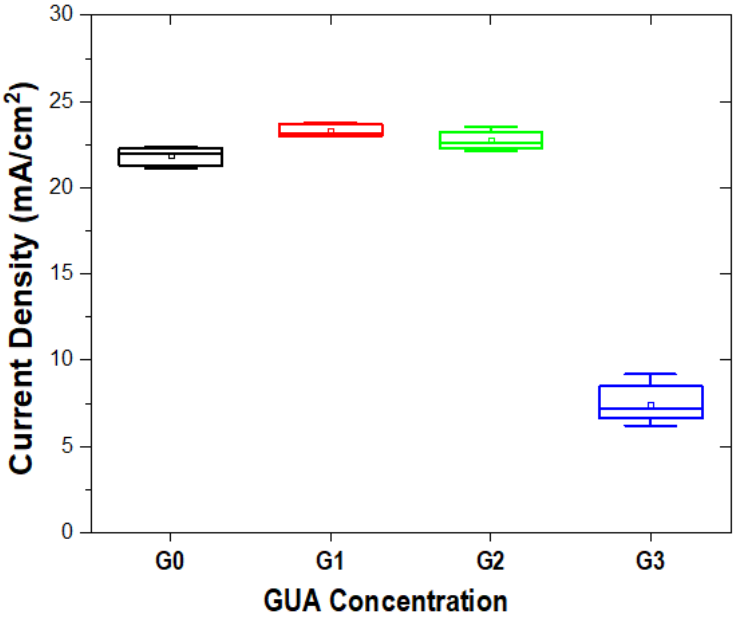

Fig. C3 Box plot of J_{SC} of perovskite devices with different GUAI loading conditions

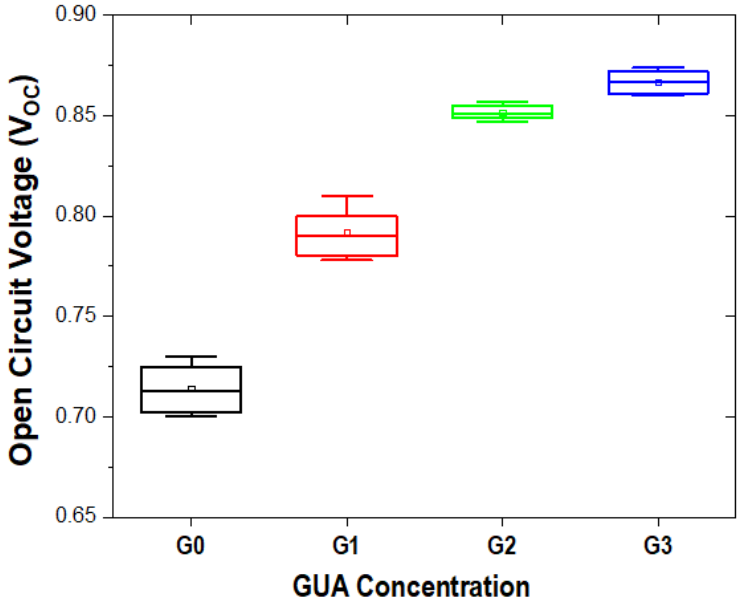

Fig. C4 Box plot of V_{OC} of perovskite devices with different GUAI loading conditions

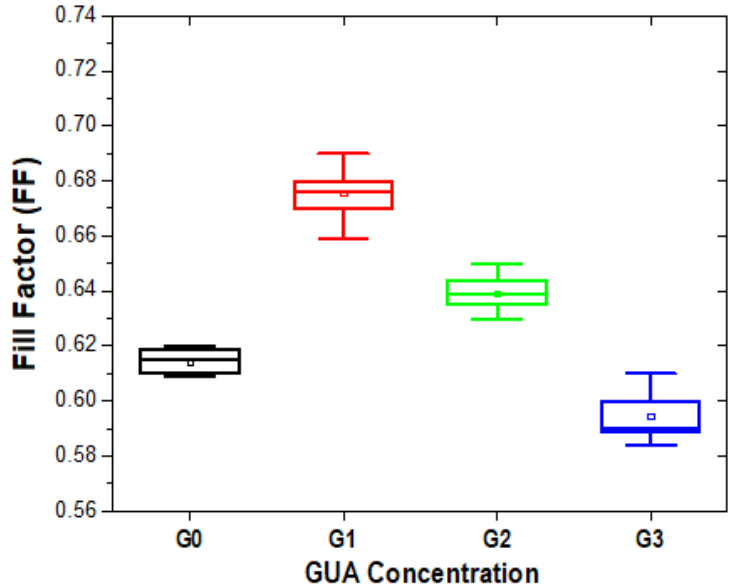

Fig. C5 Box plot of FF of perovskite devices with different GUAI loading conditions

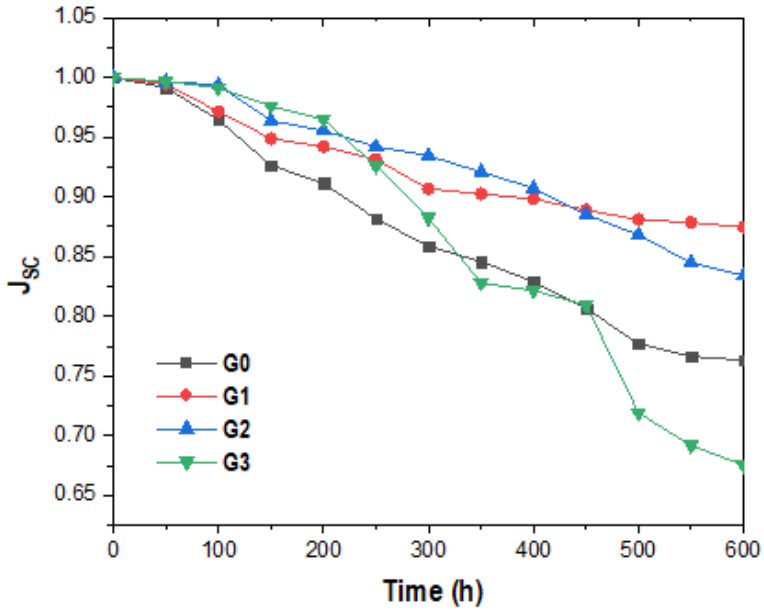

Fig. C6 J_{SC} decay of perovskite devices with different GUAI loading conditions

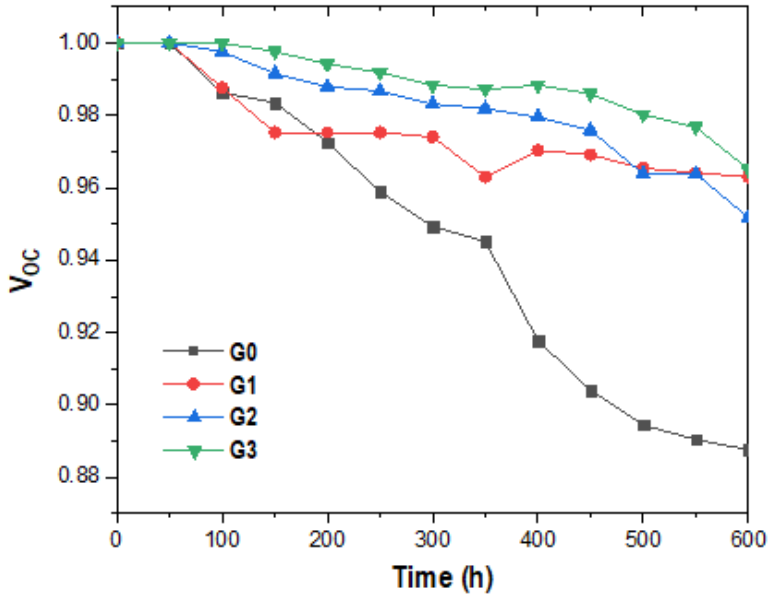

Fig. C7 V_{OC} decay of perovskite devices with different GUAI loading conditions

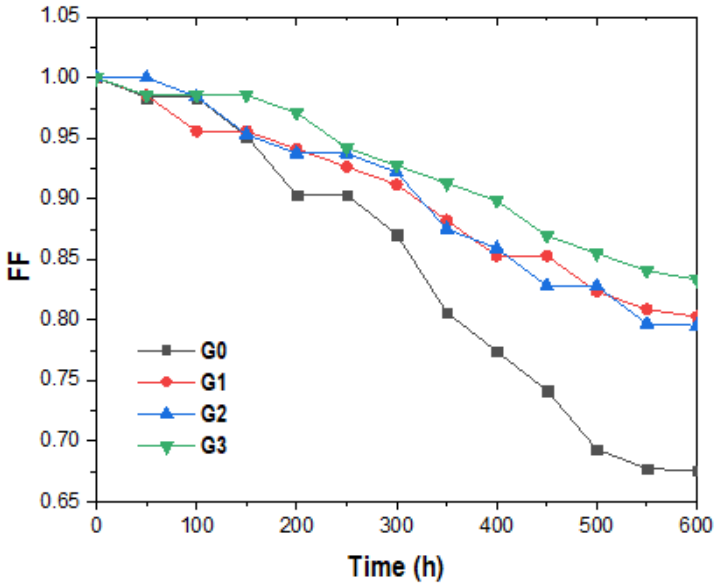

Fig. C8 FF decay of perovskite devices with different GUAI loading conditions